ABSTRACT

Title of dissertation: SELF-CONSISTENT SIMULATION OF RADIATION AND SPACE-CHARGE IN HIGH-BRIGHTNESS RELATIVISTIC ELECTRON BEAMS

David R. Gillingham
Doctor of Philosophy, 2007

Dissertation directed by: Professors Thomas M. Antonsen, Jr. and Patrick G. O'Shea
Department of Physics

The ability to preserve the quality of relativistic electron beams through transport bend elements such as a bunch compressor chicane is increasingly difficult as the current increases because of effects such as coherent synchrotron radiation (CSR) and space-charge. Theoretical CSR models and simulations, in their current state, often make unrealistic assumptions about the beam dynamics and/or structures. Therefore, we have developed a model and simulation that contains as many of these elements as possible for the purpose of making high-fidelity end-to-end simulations. Specifically, we are able to model, in a completely self-consistent, three-dimensional manner, the sustained interaction of radiation and space-charge from a relativistic electron beam in a toroidal waveguide with rectangular cross-section. We have accomplished this by combining a time-domain field solver that integrates a paraxial wave equation valid in a waveguide when the dimensions are small compared to the bending radius with a particle-in-cell dynamics code. The result is shown to agree

with theory under a set of constraints, namely thin rigid beams, showing the stimulation resonant modes and including comparisons for waveguides approximating vacuum, and parallel plate shielding. Using a rigid beam, we also develop a scaling for the effect of beam width, comparing both our simulation and numerical integration of the retarded potentials. We further demonstrate the simulation calculates the correct longitudinal space-charge forces to produce the appropriate potential depression for a converging beam in a straight waveguide with constant dimensions. We then run fully three-dimensional, self-consistent end-to-end simulations of two types of bunch compressor designs, illustrating some of the basic scaling properties and perform a detailed analysis of the output phase-space distribution. Lastly, we show the unique ability of our simulation to model the evolution of charge/energy perturbations on a relativistic bunch in a toroidal waveguide.

SELF-CONSISTENT SIMULATION OF RADIATION AND SPACE-CHARGE IN HIGH-BRIGHTNESS RELATIVISTIC ELECTRON BEAMS

by

David R. Gillingham

Dissertation submitted to the Faculty of the Graduate School of the
University of Maryland, College Park in partial fulfillment
of the requirements for the degree of
Doctor of Philosophy
2007

Advisory Committee:
Professor Patrick O'Shea, Chair/Advisor
Professor Thomas Antonsen, Co-Advisor
Professor Victor Granantstein
Senior Resarch Scientist Gregory Nusinovich
Professor Adil Hassam

Acknowledgments

This work was made possible by support from the Office of Naval Research and Joint Techology Office. I of course would like to thanks my advisors for their support and advice. As well I would also like to thank the Institute for Research Electronics and Applied Physics (IREAP) for the use of their facilities, and the generous support of the staff, especially Dottie Brosius for her help with LaTeX. Lastly, I would like to acknowledge the support of my family and especially my wife Beth for allowing this to be possible, providing invaluable emotional support and allowing me to pursue a career in science.

D.R. Gillingham

Table of Contents

List of Tables v

List of Figures v

List of Abbreviations xii

1 Introduction 1
1.1 Outline of Thesis 5

2 Synchrotron Radiation 6
2.1 History and Description of the Problem 6
2.2 Theory of Synchrotron Radiation 7
2.3 Self-Interaction 10
2.3.1 Angular Dependence 12
2.4 One-Dimensional Theory of the Longitudinal CSR Force 16
2.5 Effect of Perfectly Conducting Boundaries 18

3 Simulation Model and Methodology 25
3.1 Introduction 25
3.2 Simulation Model and Method 28
3.2.1 Theoretical Model 28
3.2.2 Comparison with Previous Work 35
3.2.3 Simulation Method 39
3.3 Symmetry and the Paraxial Wave Equation 42
3.4 Description of Symmetry using Basis Functions 43
3.5 Results 51

4 Particle Dynamics 67
4.1 Equations of Motion in Magnetic Dipole Field 68
4.2 Reference Trajectory 68
4.3 Deviations from Reference Trajectory 69
4.4 Numerical Integration the Equations of Motion 70
4.5 Linear Approximation and Matrix Methods 72
4.6 Edge Effects 73
4.7 Particle-in-Cell Method 75
4.8 Space Charge in Converging/Diverging Beams 78
4.9 Derviation of the Space-Charge Forces 79
4.10 The Talman Force and Cancellation Effect 83

5 Self-Consistent Simulations 85
5.1 Drift Space 85
5.2 Converging Beam in Straight Waveguide 91
5.3 Bunch Compressor Chicanes 93

5.3.1 Estimation of Emittance Dilution 96
5.3.2 CSR Workshop Benchmark Chicane 97
5.3.3 SDL-type Bunch Compressor Chicane 102
5.4 Microbunching 117

6 Summary and Outlook 125

List of Tables

2.1 Synchronous Modes of Square Toroidal Waveguide 24

5.1 Drift Space Test Case Parameters. 86

5.2 CSR Workshop Chicane Bunch Compressor Parameters. 98

5.3 CSR Workshop beam parameters. 100

5.4 CSR Workshop Summary. 101

5.5 CSR Workshop Summary at 500MeV. 103

5.6 SDL-type Chicane Bunch Compressor Parameters. 104

5.7 SDL BCC beam parameters. 106

List of Figures

2.1 Geometry for synchrotron radiation calculations. The source is at the retarded position A1 at time t1, and the observer is at B2 at time t2 10

2.2 Spectrum of synchrotron radiation showing coherent and incoherent contributions. For the coherent spectrum, the distribution is Gaussian with N=10, and $\sigma\omega_c/c = 0.01$. 15

2.3 Wave propagation between infinite perfectly conducting parallel plates, above and below the plane of curvature. 19

2.4 Toroidal waveguide with rectangular cross section. The bend radius is R, the width is a, and the height is b. Also shown is the cylindrical coordinate system. 21

3.1 Accelerator coordinate system. At any given distance s along the reference trajectory, we can assume a local radius of curvature $R(s)$. Deviations in the transverse directions are given by x (in the bending plane) and y (perpendicular to the bending plane). 30

3.2 Implicit integration scheme showing which points in space and time are used to solve for the point to be updated. Here the iteration runs from forward to back and requires initializing the furthest upstream point in order to solve for all others (set to zero if sufficiently upstream). 46

3.3 Comparison of time-domain (left) and frequency-domain (right) methods. The colors represent that strength of the longitudinal electric field taken at the midplane ($y = 0$). The horizontal axis is x, with the inside of the bend to the left and the vertical axis z with the head of the bunch towards the bottom. The top images are after 1 cm and the bottom after 5 cm. In the frequency-domain method, energy falling behind the computational window has reappeared ahead of the bunch, violating causality. 52

3.4 Space charge force x-component as a function of x in a straight 30 x 30 cm waveguide, taken at center point of a three-dimensional Gaussian bunch with rms length $\sigma_z = 0.23$ cm, and rms width $\sigma_\perp = 0.2$ cm. Simulation results are circles, and theory is represented by a solid line. The force is normalized to $F_0 = Ne^2/\sqrt{2\pi}\sigma_z\gamma^2$. 54

3.5 . Steady-state longitudinal force from rigid charge distribution of varying widths in x-direction. The beam is a three-dimensional Gaussian with the z and y rms beam widths held constant. The symbols are the result of simulation and the lines are the result of numberical integration of Eqs (3.24,3.25). The longitudinal coordinate z is scaled to the rms bunch length σ_z, which is 60 μm, and the force is scaled to $W_0 = \sqrt{2/\pi}Ne^2(3R^2\sigma_z^4)^{-1/3}$. The rms beam widths are scaled to the formation length $s_f = 2(3\sigma_z R^2)^{1/3}$. As discussed in the text, a more appropriate scaling is x/x_0 where $x_0 = (3\sigma_z^4 R^2)^{1/6}$ which for these three cases have values 0.5, 1.5 and 3.0. 56

3.6 Longitudinal force as a function of z (taken at $x, y = 0$) from CSR in transient states (measured in distance traveled past entrance) from simulation (symbols) compared to vacuum theory (lines) for three-dimensional Gaussian bunch in a 30 x 30 cm rectangular waveguide with uniform bending radius of 120 cm. The longitudinal coordinate z is scaled to the rms bunch length σ_z, which is 0.23 cm, and the force is scaled to $W_0 = \sqrt{2/\pi}Ne^2(3R^2\sigma_z^4)^{-1/3}$ 57

3.7 Longitudinal force as a function of z (taken at $x, y = 0$) from CSR in steady state with shielding from infinite parallel plates for three different gap sizes. The simulation (symbols) is compared to infinite parallel plate theory (lines) for Gaussian line charge. The bending radius is 120 cm, and the horizontal gap in the simulation is fixed at 50 cm to approximate infinite parallel plates. The longitudinal coordinate z is scaled to the rms bunch length σ_z, which is 0.23 cm, and the force is scaled to $W_0 = \sqrt{2/\pi}Ne^2(3R^2\sigma_z^4)^{-1/3}$ 59

3.8 Longitudinal force as a function of z (taken at $x, y = 0$) from CSR in steady state in a square toroidal waveguide. The sinusoidal wake behind the bunch is the lowest order synchronous mode TE(1,0), and has wavenumber $k = 13.2$ cm. The bending radius is 120 cm, and the width and height are 2.5 cm. The longitudinal coordinate z is scaled to the rms bunch length σ_z, which is 0.115 cm, and the force is scaled to $W_0 = \sqrt{2/\pi}Ne^2(3R^2\sigma_z^4)^{-1/3}$. 60

3.9 Average power loss from the TE(1,0) synchronous mode in a square toroidal waveguide as a function of distance s along the bend. The bending radius is 120 cm, and the width and height are 2.5 cm. The bunch length $\sigma_z = 0.115$ cm, and the rms beam width is $\sigma_\perp = 0.07$ cm. The symbols are the average beam energy deviation (from 100 MeV initial energy) expressed in keV, and the line is theoretical prediction of 67 eV/cm. The simulation results reaches a steady-state loss rate of 66 eV/cm, which differs from the theoretical prediction by 1.5 % . 62

3.10 Power spectrum of E_z (taken at $x, y = 0$) from CSR in steady state in a square toroidal waveguide, showing the three lowest frequency synchronous modes. The bending radius is 120 cm, and the width and height are 2.5 cm. The three modes have predicted wavenumbers of 13.2, 24.3 and 35.5 cm^{-1} respectively. The beam is a fixed three-dimensional Gaussian with $\sigma_z = 0.028$ cm, and $\sigma_\perp = 0.07$ cm. 64

3.11 Transverse coherent synchrotron radiation force in steady state as a function of z, taken along the center $x, y = 0$ of a three-dimensional Gaussian bunch given by simulation (shown in circles). The theoretical value (line) was calculated by numerical integration of Eqs.(3.24) and (3.25). The longitudinal coordinate z is scaled to the rms bunch length σ_z and the force is scaled by $F_{x0} = 2Ne^2/R$. 65

4.1 Geometry for fringe field calculation. The beam trajectory in the s-direction, exits at an angle η with respect to perpendular to the horizontal pole face, the h-direction. 74

4.2 Cloud-in-cell charge assignment function for the one-dimensional case. If the charge is located directly on a grid point then all of the charge is assigned there. Otherwise there will always be two grid points receiving charge assignment. The cloud size may be made larger than $2\Delta x$. 76

5.1 Beam envelope simulation compared to theory. The simulation was modified to use the steady-state space-charge forces at all times, and a very long beam approximation so that there are no longitudinal effects. 89

5.2 Geometry for converging beam test case. An axisymmetric laminar beam with initial rms radius σ_{in} is first focused by a thin lens with focal length f_0. The second lens is defocusing with focal length = $f_0/2$, resulting in a laminar beam with rms radius $\sigma_{out} = \sigma_{in}/2$. . . . 92

5.3 Comparison of the initial and final potential depression as measured both by the field and particle solvers of the simulation. The beam starts in laminar flow and is focused axisymmetrically to half its original beam width. The simulation used two thin lenses, separated by 50 cm, acting as a telescope. 92

5.4 Bunch compressor chicane consisting of four dipole magnets. The first and last magnets have the same polarity which is opposite of the middle two. All magnets have identical field strengths. The distance between the second and third magnet does not affect the compression strength. The bending angle is θ_D, the projected length of the magnet is L_M and the separation between magnets is L_D. The path through the chicane corresponds the reference energy. Particles with higher energy will take shorter path and particles with lower energy will take a longer path, therefore a bunch with a linear energy chirp will either compress or expand accordingly. 94

5.5 Emittance growth (red, solid) and energy loss (blue, dashed) as a function of distance in CSR workshop bunch compressor chicane. The beam is at 5 GeV, 1 nC. The emittance growth is computed as the absolute value of the difference between the 1 nC and the 0 nC simulations. Energy loss is the difference of the average particle energy from 5 GeV. 99

5.6 Emittance growth (red, solid) and energy loss (blue, dashed) as a function of distance in CSR workshop bunch compressor chicane. The beam is at 0.5 GeV, 1 nC. The emittance growth is computed as the absolute value of the difference between the 1 nC and the 0 nC simulations. Energy loss is the difference of the average particle energy from 0.5 GeV. 102

5.7 Bunch length (rms) as a function of path length in the SDL bunch compressor. The total charge is 0.3 nC. The red lines (solid) corresponds to a linear chirp of 0.105 cm^{-}1 which results in a final rms pulse length of 0.6 ps , and the blue line (dashed) corresponds to a linear chirp of 0.125 cm^{1} and corresponds to a final rms pulse length of 0.2 ps. 105

5.8 Horizontal beam width (rms) as a function of path length in the SDL bunch compressor. The total charge is 0.3 nC. The red lines (solid) corresponds to an intial betatron function of 5 m^{-}1, and the blue line (dashed) corresponds to an intial betatron function of 20 $^{-}$1. The chirp in both cases in 0.105 cm^{-}1. 107

5.9 Dispersion functions for the SDL bunch compressor parameters. . . . 109

5.10 Dispersion-corrected transverse emittance as a function of path traveled in the SDL bunch compressor. The bunch charge is 0.3nC. The three differenent case show the effect of varying basic beam parameters on the emittance growth. The largest effect is pulse length which scale roughly as $\sigma_z^{-4/3}$. The effect of beamwidth is approximately $\tilde{x}^{1/2}$. 110

5.11 Emittance (x, rms, normalized) taken in 0.02 ps slices at exit of compressor for 0.2 ps rms final pulse length(red, solid) and 0.6 ps (blue, dashed). Each slice is corrected for the centroid of x and x' independently. For the 0.2 ps case, the projected emittance was 18.5 μm, and for the 0.6 ps case, the projected emittance was 5.5 μm. In both cases, there is not a significant difference between the peak slice emittance and the projected emittance, indicating that the emittance growth is random, not systematic. 112

5.12 Transverse (x) phase-space at exit of SDL bunch compressor. The bunch charge is 0.3 nC, and the final rms pulse length is 0.2 ps. The offset in both coordinates is due to the net energy loss of the beam. The normalized rms emittance, which is corrected for the offsets in centroids, is 18.5 mm-mrad (initial was 2 mm-mrad). 113

5.13 Longitudinal phase-space at exit of SDL bunch compressor. The bunch charge is 0.3 nC, and the final rms pulse length is 0.2 ps. The general curved shape reflects the non-linear dependence of path length on energy. The wavy deflection in the center is from CSR. . . 114

5.14 Transverse emittance growth for three different values of bunch charge. Also plotted is a perfect quadratic dependence for reference. 115

5.15 Transverse emittance growth for three different values of bunch charge. Also plotted is a perfect quadratic dependence for reference. 116

5.16 Longitudinal force after 375 cm (one-half revolution) at midplane ($y = 0$) as a function x, positive towards the outside wall and z, negative towards the bunch head. The bunch is surrounded by a square waveguide with dimension 2.5 cm. The other parameters are $R =$ 120 cm, $E = 100$ MeV, Gaussian bunch $\sigma_z = 5.75$ mm with 20% modulation at wavelength 4.0 mm, initial $\sigma_x = 1.0$ mm.The color indicates the magnitude of the longitudinal force, in units of F_z/e^2 (cm^{-2}). There is no force forward of the bunch because the group velocity for this (and all) resonant mode is less than than the bunch velocity. At this bunch length, the beam would otherwise be completely shielded from CSR self-interaction, however the modulation has stimulated the lowest order synchronous mode. 118

5.17 Longitudinal phase space density after 375 cm (one-half revolution). The bunch is surrounded by a square waveguide with dimension 2.5 cm. The other parameters are $R = 120$ cm, $E = 100$ MeV, Gaussian bunch $\sigma_z = 5.75$ mm with 20% modulation at wavelength 4.0 mm, initial $\sigma_x = 1.0$ mm. Although the bunch clearly shows modulation a the wavelength of the lowest synchronous mode, there is a substantial incoherent energy spread resulting from the beam width. 119

5.18 Charge density as a function of x (horizontal, outer wall to right) and z (vertical, head is towards bottom) comparing input (on left) and output after 180^o bend. The intial modulation was 20% with a 4.0 mm wavelength on a Gaussian bunch with $\sigma_z = 0.575$ mm, which would otherwise be completely shielded from CSR interaction. The waveguide is square with transverse dimension 2.5 cm and bending radius R= 120 cm. Although the amount of bunching is small, there is a noticeable effect particularly towards the tail of the bunch. Microbunching is also limited somewhat by the finite beamwidth which in this case is 1 mm, approximately 25% of the resonant wavelength. 121

5.19 Current comparing input (blue, dahsed) and output (red, solid) after one complete revolution in bend. The intial modulation was 20% with a 4.0 mm wavelength on a Gaussian bunch with $\sigma_z = 0.575$ mm, which would otherwise be completely shielded from CSR interaction. The waveguide is square with transverse dimension 2.5 cm and bending radius R= 120 cm. 123

List of Abbreviations

BCC	Bunch Compressor Chicane
BNL	Brookhaven National Laboratory
CIC	Cloud-in-Cell
CSR	Coherent Syncrotron Radiation
FEL	Free Electron Laser
FODO	Focusing-Defocusing
IREAP	Institute for Research in Electronics and Applied Physics
LCLS	Linac Coherent Light Source
NGP	Nearest Grid Point
SCARS	Space-charge and Radiation Simulation
SDL	Source Development Laboratory
TSC	Triangularly-shaped-Cloud

Chapter 1

Introduction

As accelerators are now capable of producing ultra-high brightness electron beams, characterized by both high peak current and low transverse emittance, the difficulty in preserving the quality throughout transport systems has increased. When used to drive a light source, such as a Free Electron Laser (FEL), the optical quality of the light source depends critically on the quality of the electron beam [1, 2]. One where the beam quality may be degraded of particular concern is in bends. Examples are 180^o bends for energy recovery linacs [3–6], or magnetic dipole bunch compressor chicanes. In FEL's bunch compression is used to increase the peak current which in turn increases the small-signal gain. In each of these bending systems, the potential exists for the coherent self-interaction of the beam with it's own synchrotron radiation, or *coherent synchrotron radiation* (CSR) to diminish the beam quality. CSR also limits the maximum energy of charged particles in accelerators because the radiated power scales as the fourth power of energy. Additionally the CSR will induce a spread of energies within the bunch that, through the dispersive action of bending systems, will translate into a spread of horizontal velocites. More recently, there is concern whether a CSR wakefield could cause a single bunch instability [7]. Yet, there is still much about the CSR interaction that is not well understood. The difficulty in calculating CSR comes from it's relativistic nature.

The (relatively) long time it takes for radiation to overtake an electron which is moving away from the source at nearly the speed of light (as observed from the laboratory frame) complicates the calculation immensely.

One finds that the theory of CSR has developed primarily along lines where some simplifications can be made. For example, it is usually assumed that the source and observer particles move uniformly along the arc of a circle. This particular problem was first solved by Schott [8] in 1912 in the context of explaining atomic spectra. While the calculation did not succeed in it's original purpose, it was however the correct theory for CSR. After synchrotron radiation was observed by Blewett in 1946 [9], concern grew that high charge bunched beams could not bent successfully because of the coherent enhancement of the radiation for wavelengths longer the bunch lengths [10]. However, the bunch lengths of interest were relatively long compared to the characteristic wavelength for synchrotron radiation, and the effects of shielding from the beam pipe turned out to mitigate CSR at long wavelengths [11, 12]. After this burst of activity, slow but important progress was made [13–17] until the evolution of very short high brightness electron beams brought the problem again into the forefront of scientific interest [18–20]. We now are considering designs that produce very high charges, exceeding 1 nC, at bunch lengths less than 1 ps.

Since the time when the theory of CSR first came to the forefront of scientific concern, we have also seen significant effort put into simulation of the effects of CSR [21]. Along these lines, we have two major methods. The first method is to solve the problem by direct computation in terms of retarded potentials. Parallel plate shielding can be included using the method of image charges, but the inclusion of full

waveguide boundaries are not possible using retarded potentials. This prohibits the study of interaction with what are now known as resonant modes of the waveguide. [16, 17]. The second method is to solve a partial differential equation, the paraxial CSR wave equation, which approximates the full wave equation in the toroidal waveguide [22]. This has been our approach. This technique was sucessfully used to replicate the results of theory from a line charge and extended the ability to include transient waveguide solutions [23]. This is the starting point for the research described in this dissertation. We had hoped to apply this technique to elements such as magnetic bunch chicanes used to longitudinally compress the bunch. Unfortunately, this technique did not prove suitable, primarily as a consequence of working in the frequency domain and in three-dimensions.

Therefore we developed our own method for integrating the CSR paraxial wave equation in the time-domain. As we shall see, this method is able to replicate the results of theory. We will show comparisons of the longitudinal electric field under transient conditions, as well as the steady-state field with parallel plate shielding. We also derive a method for computing the transverse forces and compare the results with numerical integration of the retarded potentials in the limiting case as large waveguide dimensions approximating the vacuum case. For both longitudinal and transverse directions, we show that our method also calculates the correct space charge forces. Finally, we show the stimulation of the resonant modes for the toroidal waveguide.

It should be noted, however, that these comparisons with theory are all based on an assumption of a fixed, or a slowly evolving source, where slowly is defined

relative to the time it takes radiation to overtake the bunch. However, in a bunch compressor or bend, there are two important departures from the ideal conditions of the theory. First, bunch compression depends on *dispersion*, the perturbation of the horizontal trajectories with energy. Therefore, our simulation must be at least two-dimensional. Secondly, the evolution of the beam is generally not slow. In fact, in a dispersive element, the beam quickly diverges/conveges in the horizontal plane which introduces relatively rapid changes to the energy distribution. In a waveguide, the beam will stimulate modes which, because of their propagation characteristics, may quickly fall behind the beam. In the frequency-domain method described above, this radiation would reappear in the computational domain, but ahead of the bunch. Unless we intended to simulate an infinite train of closely space bunches (we do not), this violates casuality, where signals cannot travel faster than the speed of light. The time-domain technique that we have developed can explicitly prevent this through the choice of boundary conditions which we also demonstrate using a side-by-side comparison of simulations using the two domains.

Having solved this difficulty as well as developing methods for calculating the transverse forces and incorporating space-charge, we have integrated the field calculation with a particle-in-cell code in a self-consistent manner. As a result, we can simulate the full bunch dynamics in a bunch compressor, and any combination of straight or uniformly curved sections, including the reaction of the beam to it's self-generated fields. We show results for the beam envelope evolution under tranverse space charge fields, and the effect of longitudinal space charge in converging/diverging beams. Lastly we perform several end-to-end simulations of bunch

compressor chicanes, comparing the results to a benchmark case as well as demonstrating the basic scaling of emittance dilution. Finally we apply the self-consistent simulation method to the coherent microwave or microbunching instability [24, 25].

1.1 Outline of Thesis

This thesis is primarily divided into two sections. After some discussion of general theory of CSR, we describe in detail our method for solving the partial differential equation for the fields. We will also derive a method for calculating the complete set of Lorentz forces using just two electric fields under a consistent set of assumptions. The results of this section are then compared to the bulk of CSR theory, where we show, under the same set of assumptions, that the forces calculated by our simulation match those of the theory to a high degree of accuracy. In the second major section, we now describe how the bunch dynamics can be included in a self-consistent manner. We then proceed to show the application of the whole integrated simulation to some test cases, representative of the current state-of-the-art accelerator designs.

Chapter 2

Synchrotron Radiation

2.1 History and Description of the Problem

The first observation of visible radiation from circulating electrons occured in 1947 at the 70 MeV synchrotron build at General Electric [26], but the effect described in terms of energy loss was predicted as early as 1898 by Liénard [27] and again in 1912 by Schott [8]. The sucessful verification by experiment in 1946 was completed by Blewett [9] . Since then, we now use the term *synchrotron radiation* to describe any radiation from relativistic charged particles that are moving instantaneously along the arc of circle.

There has been tremendous development in the theory and technology of synchrotrons and the production of high-intensity radiation from them since that time. However, this is not the exact effect we are interested in. Synchrotron radiation is normally observed from a fixed position in the laboratory frame as a periodic burst of broad spectrum radiation as the electron bunch sweeps by the point where a line from the observer tangentially intersects the circular trajectory of the electrons. In the beam frame, the same radiation appears as a form of space-charge, meaning it reaches a steady-state condition. It also has a very different character. As we will see later, the angular distribution over all frequencies of synchrotron radiation is quite narrow, with angular width γ^{-1} centered about the tangent. Since the tan-

gent never intersects the arc of motion, one could argue that synchrotron radiation can never be felt by an observation point along the arc. If we change our view to measure the angular distribution as a function of frequency (as seen by a lab frame observer) we will see that at lower frequencies the distribution is quite wide.

2.2 Theory of Synchrotron Radiation

For a single electron *in vacuo*, we begin with Lienard-Wiechert Potentials [27, 28]

$$\phi(t) = \frac{e}{(1 - \boldsymbol{n} \cdot \boldsymbol{\beta})D}, \tag{2.1}$$

$$\boldsymbol{A}(t) = \frac{e\boldsymbol{\beta}}{(1 - \boldsymbol{n} \cdot \boldsymbol{\beta})D}, \tag{2.2}$$

from source particle at a point $(\boldsymbol{r}', t')$ as observed by a particle at $(\boldsymbol{r}, t)$ provided that the distance between the source and observation point was less than the distance $D = |\boldsymbol{r}(t) - \boldsymbol{r}'(t')| < c|t - t'|$. This condition is called *causality*. Otherwise, the radiation could not have traveled far enough to be felt, limited by the speed of light. $\boldsymbol{\beta}$ is the velocity of the source at the retarded time divided by the speed of light c, and the unit vector $\boldsymbol{n}$ points from the source at B1 to the observation point at A2 as illustrated in Fig. 2.1.

We calculate the fields $\boldsymbol{E} = -\nabla\phi - \partial\boldsymbol{A}/c\partial t$, and $\boldsymbol{B} = \nabla \times \boldsymbol{A}$. The fields are

$$\boldsymbol{E} = e\left[\frac{(\boldsymbol{n} - \boldsymbol{\beta}')}{\gamma^2(1 - \boldsymbol{n} \cdot \boldsymbol{\beta}')^3 D^2}\right]_{ret} + \frac{e}{c}\left[\frac{\boldsymbol{n} \times (\boldsymbol{n} - \boldsymbol{\beta}') \times \dot{\boldsymbol{\beta}}'}{(1 - \boldsymbol{n} \cdot \boldsymbol{\beta}')^3 D}\right]_{ret} \tag{2.3}$$

$$\boldsymbol{B} = \boldsymbol{n} \times \boldsymbol{E}, \tag{2.4}$$

where $\dot{\boldsymbol{\beta}}'$ is the source acceleration vector, which points inward for the instantaneous

circular motion associated with synchrotron radiation.

For motion that is instantaneously circular with radius R, the acceleration has value $\dot{\beta} = v^2/cR$ and is perpendicular to the velocity. If the electron is non-relativistic, $\beta = 0$, the first term will not contribute to power loss because $\boldsymbol{B} \to 0$. The expression for second (acceleration) term becomes

$$\boldsymbol{E}_a = \frac{e}{c}\left[\frac{\boldsymbol{n}\times(\boldsymbol{n}\times\dot{\boldsymbol{\beta}})}{D}\right]_{ret}, \tag{2.5}$$

$$\boldsymbol{B}_a = \boldsymbol{n}\times\boldsymbol{E}_a. \tag{2.6}$$

The intantaneous energy flux is computed from the Poynting vector

$$\boldsymbol{S} = \frac{c}{4\pi}\boldsymbol{E}\times\boldsymbol{B} = \frac{c}{4\pi}|\boldsymbol{E}_a|^2\boldsymbol{n}. \tag{2.7}$$

Integrating the Poynting vector over all a spherical surface with radius D_{ret} yields the Larmor result for the total power emitted

$$P = \frac{2}{3}\frac{e^2}{c^3}\frac{v^4}{R^2}. \tag{2.8}$$

The relativistic generalization is

$$P = \frac{2}{3}\frac{e^2c}{R^2}(\beta\gamma)^4. \tag{2.9}$$

For incoherent synchrotron radiation, we simply add the contributions to the radiated power from individual electrons to obtain the total radiated power which scales linearly with the number of electrons in the bunch N. As an example, a 1 A electron beam at 100 MeV with $R = 1$ m would lose power only at 8.85 watts.

Coherent synchrotron radiation occurs for portions of the spectrum where the wavelengths are larger than the bunch length. A proper summation for the total

radiation is computed by summing the fields, not the power, from the individual electrons. This could change the total power by up to an additional factor of N. To see how this occurs, consider a single frequency component of the radiated field from an individual electron

$$E_k \sim e^{i(\omega t+\phi_k)}. \tag{2.10}$$

Summing the square of the electric fields will lead to $P = F(\omega)P_1$ where P_1 is the power from a single electron at frequency ω, and

$$F(\omega) = \sum_{j,k} E_j E_k^* = \sum_{j,k} e^{i(\phi_j-\phi_k)}. \tag{2.11}$$

This sum can be also be written as a sum

$$F(\omega) \sim N + \sum_{j\neq k} e^{i(\phi_j-\phi_k)}, \tag{2.12}$$

where the terms represent the contribution from incoherent and coherent radiation respectively. The coherent term will be zero if the phases are uncorrelated and distributed uniformly over all phases. However, if all the phases are identical, this term will sum to $N(N-1) \approx N^2$. For a large number of electrons, we can convert the summation into integration

$$F(\omega) = \sum_{j,k} e^{i(\phi_j-\phi_k)} \rightarrow \int_{-\infty}^{\infty}\int_{-\infty}^{\infty} \rho(x)\rho(y)e^{i(x-y)\omega/c}dxdy. \tag{2.13}$$

If the distribution is Gaussian,

$$\rho(z) = \frac{N}{\sqrt{2\pi}\sigma} e^{-z^2/2\sigma^2}, \tag{2.14}$$

then

$$F(\omega) = N^2 e^{-(\omega\sigma/c)^2}. \tag{2.15}$$

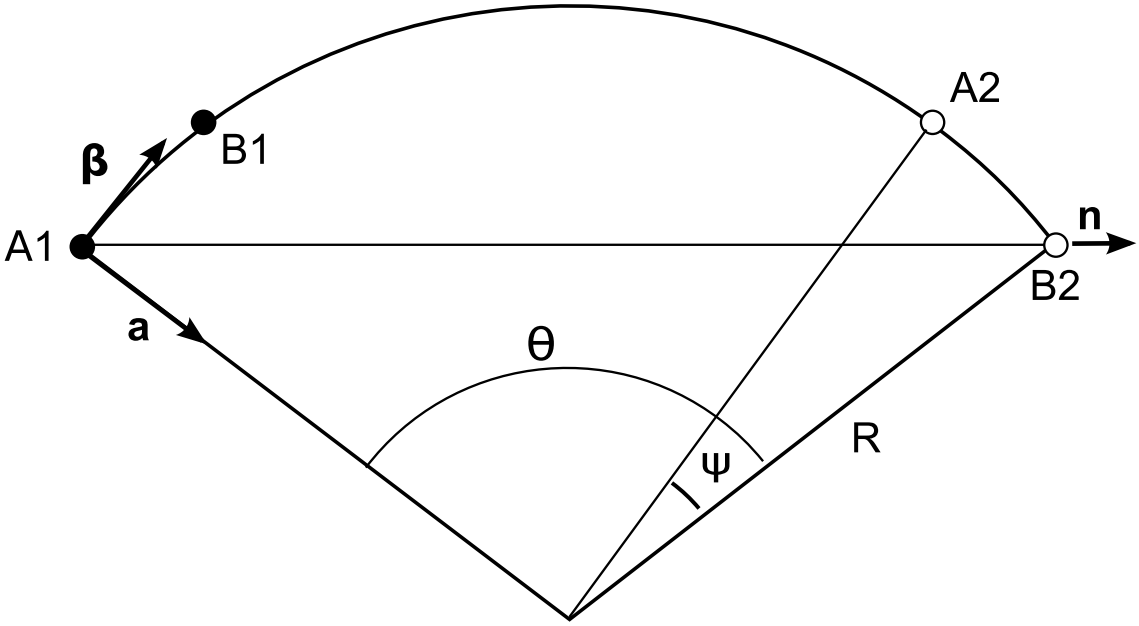

Figure 2.1: Geometry for synchrotron radiation calculations. The source is at the retarded position A1 at time t1, and the observer is at B2 at time t2

So now we see that if the wavelength of interest is very long compared to the bunch length then $\omega\sigma/c \ll 1$ such that $F(\omega) \to N^2$. Thusly, the radiation will be temporally coherent and the power will scale with the square of the beam current.

2.3 Self-Interaction

We now consider the possibility of synchrotron radiation acting on an electron bunch traveling along an arc of a circle. The energy change of a test electron traveling along the same trajectory at a fixed separation in time will be caused by only the longitudinal electric field. We separate the components of the force into transverse and longitudinal parts by defining a vector $\boldsymbol{e} = (e_x, e_y, e_z)$ where e_x points outward

from the center of the arc, e_y is perpendicular to the plane of motion, and e_z in in the same direction as β. The various vectors can be written

$$\boldsymbol{n} = (\sin[\theta/2], 0, \cos[\theta/2]), \tag{2.16}$$

$$\boldsymbol{\beta}' = \beta'(\sin[\theta], 0, \cos[\theta]), \tag{2.17}$$

$$\dot{\boldsymbol{\beta}}' = \frac{c\beta'^2}{R}(-\cos[\theta], 0, \sin[\theta]). \tag{2.18}$$

The distance between source and observer

$$D = 2R\sin(\theta/2). \tag{2.19}$$

The rate of energy change is

$$\frac{d\gamma}{dt} = \frac{e^2}{mc^2}\left[\frac{\boldsymbol{\beta}\cdot\boldsymbol{n} - \boldsymbol{\beta}\cdot\boldsymbol{\beta}'}{\gamma^2 D^2(1-\boldsymbol{n}\cdot\boldsymbol{\beta}')^3} + \frac{\boldsymbol{\beta}\cdot(\boldsymbol{n}-\boldsymbol{\beta}')\boldsymbol{n}\cdot\dot{\boldsymbol{\beta}}' - \boldsymbol{\beta}\cdot\dot{\boldsymbol{\beta}}'(1-\boldsymbol{n}\cdot\boldsymbol{\beta}')}{D(1-\boldsymbol{n}\cdot\boldsymbol{\beta}')^3}\right]_{ret} \tag{2.20}$$

We now compute the various quantities

$$\boldsymbol{n}\cdot\boldsymbol{\beta} = \beta\cos\theta/2 \tag{2.21}$$

$$\boldsymbol{n}\cdot\dot{\boldsymbol{\beta}}' = \frac{c\beta^2}{R}\sin\theta/2 \tag{2.22}$$

$$\boldsymbol{\beta}\cdot\dot{\boldsymbol{\beta}}' = \frac{c\beta^3}{R}\sin\theta \tag{2.23}$$

$$\boldsymbol{n}\cdot\boldsymbol{\beta}' = \beta\cos\theta/2 \tag{2.24}$$

$$\boldsymbol{\beta}\cdot\boldsymbol{\beta}' = \beta^2\cos\theta \tag{2.25}$$

After substitution and applying some trigonometric identities

$$\frac{d\gamma}{dt} = \frac{e^2}{mc^2}\frac{c\beta}{2R^2}\frac{1}{(1-\beta\cos\theta/2)^3}\left[\frac{\beta - (1-\beta\cos\theta/2)\cos\theta/2}{2\sin^2\theta/2} + \beta^2(\beta - \cos\theta/2)\right], \tag{2.26}$$

where we see that the singularity coming from D has been cancelled in the second term inside of the brackets.

2.3.1 Angular Dependence

We now estimate the angular dependence of the radiation. One must be careful, however in applying the same methods used for the non-relativistic case. The Poynting vector is not an invariant, so if we wish to calculate the radiated power in laboratory frame, we must take into account proper time.

$$\frac{dP}{d\Omega} = \frac{e}{4\pi} D_{ret}^2 |\boldsymbol{E}_a|^2 (1 - \boldsymbol{n} \cdot \boldsymbol{\beta}'). \tag{2.27}$$

Using our previous work, we find the angular dependence

$$\frac{dP}{d\Omega} \sim \frac{(\beta - \cos\theta/2)^2}{(1 - \beta\cos\theta/2)^5}. \tag{2.28}$$

If the electrons are ultra-relativistic such $\beta \approx 1 - 1/2\gamma^2$ and the angles are small so that $\cos\theta/2 \approx 1 - \theta^2/8$ we can rewrite the dependence

$$\frac{dP}{d\Omega} \sim \frac{(\hat{\theta}^2 - 1)^2}{(\hat{\theta}^2 + 1)^5}, \tag{2.29}$$

where $\hat{\theta} \equiv \gamma\theta/2$. It is clear from this form that it is peaked at $\hat{\theta} = 0$ and falls off rapidly for $\hat{\theta} \gtrsim 1$ meaning the main body of the radiation is concentrated within $\theta < \gamma^{-1}$ the usual characteristic angle associated with relativistic radiation. For $\hat{\theta} \gg 1$ the dependence falls off $\sim \hat{\theta}^{-6}$. From this, as mentioned before, one could deduce that synchrotron radiation self-effects on bunches are insignificant because the radiation is primarily tangential. However, when we allow a large portion of the radiation to be enhanced by coherency, we may find that the combination $N\hat{\theta}^{-6}$ is still not small. For example, suppose $\theta = 10^o$, $\gamma = 200$, and $N = 10^{10}$, the combination $N\hat{\theta}^{-6} = 5.6$ which despite the reduction due to the angular dependence is still larger than the incoherent radiation.

In order to fully reconcile our description of coherence, however, we need to examine the angular-spectral distribution. To be specific, we need $d^2I/d\Omega d\omega$. From [29]

$$\frac{d^2I}{d\omega d\Omega} = \frac{e^2}{3\pi^2 c}\left(\frac{\omega R}{c}\right)^2\left(\frac{1}{\gamma^2}+\theta^2\right)^2\left[K_{2/3}^2(\xi)+\frac{\theta^2}{(1/\gamma^2)+\theta^2}K_{1/3}^2(\xi)\right], \tag{2.30}$$

where

$$\xi = \frac{\omega R}{3c}\left(\frac{1}{\gamma^2}+\theta^2\right)^{3/2}, \tag{2.31}$$

and $K_\mu(z)$ is the modified Bessel function. There is negligible radiation for $\xi \gg 1$. Furthermore, this defines a critical frequency above which there is negligable radiation at all angles

$$\omega_c = 3\gamma^3 c/R. \tag{2.32}$$

For very low frequencies $\omega \ll \omega_c$, the range of angle with appreciable radiation is

$$\theta_c \approx \left(\frac{3c}{\omega R}\right)^{1/3}. \tag{2.33}$$

So, we are now in a position to understand coherence of the synchrotron radiation. First we demand that at a given frequency the radiation must have a large enough angular range to interact with the bunch in it's advanced position. This defines the angle $\psi = \sigma/R$ in Fig. 2.1. For a self-interaction, the angles ψ and θ must be related by the characteristic equation

$$\psi = \theta - 2\beta\sin(\theta/2). \tag{2.34}$$

If the angle $\theta \ll 1$, we can use the small angle expansion of the sine function

$$\sin(\theta/2) \approx \theta/2 - \theta^3/48 \tag{2.35}$$

to write an approximate version of the characteristic equation

$$\psi \approx \theta^3/24. \tag{2.36}$$

We can then rearrange this to find the formation angle

$$\theta_f \approx 2\left(\frac{3\sigma}{R}\right)^{1/3} \tag{2.37}$$

Let us estimate the maximum frequency of any radiation that can self-interact with the bunch generating it. This requires that the critical angle be at least as great as the angle encompassing the advanced beam, $\theta_c \geq \theta_f$. Upon substitution, and reaarranging, we then require

$$\frac{\omega\sigma}{c} \leq \frac{1}{8} \tag{2.38}$$

which is clearly less than the requirement for coherence. We conclude that all radiation capable of interacting with the majority of the same bunch from which it was emitted must by definition be coheherent, and now use the term coherent synchrotron radiation to describe the self-interaction of synchrotron radiation. This does not mean, however, that there is no incoherent portion, only that it will play a small factor an appear as a small energy loss term. In general, however, we will neglect that calculation of incoherent synchrotron radiation, specifically because it would require calculations at frequencies much greater than the resolution of our system.

If we integrate the radiated intensity over all angles we can also obtain the spectrum of synchrotron radiation. From [29] the integration yields

$$\frac{dI}{d\omega} = 2\sqrt{3}\frac{\gamma e^2}{c}\frac{\omega}{\omega_c}\int_{2\omega/\omega_c}^{\infty} K_{5/3}(x)dx. \tag{2.39}$$

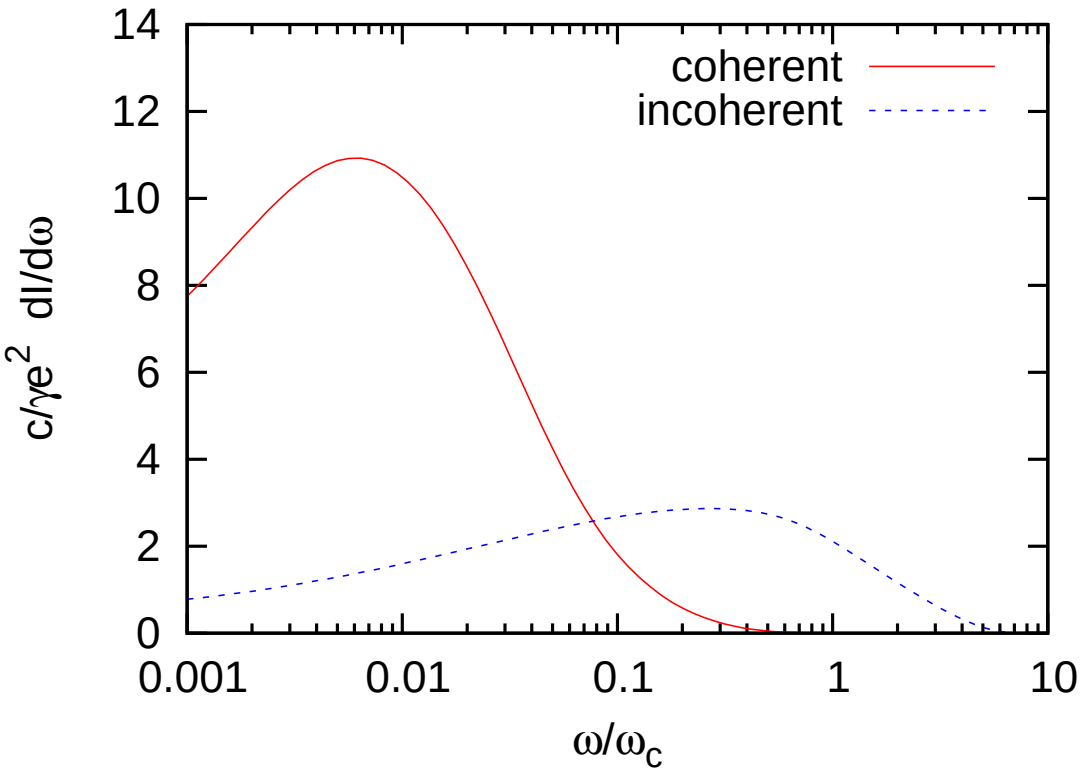

Figure 2.2: Spectrum of synchrotron radiation showing coherent and incoherent contributions. For the coherent spectrum, the distribution is Gaussian with N=10, and $\sigma\omega_c/c = 0.01$.

The spectrum as a function of ω/ω_c is shown in Fig. 2.2. On the same plot, we have shown the effect of coherence using the form factor for a Gaussian line-charge. We have arbitrarily chosen $\omega_c\sigma/c = 0.01$ and $N = 10$ for the purposes of illustration. Below frequencies where the wavelength is smaller than the bunch we clearly see the coherent spectrum. In real bunches N is more like 10^9 electrons, however.

2.4 One-Dimensional Theory of the Longitudinal CSR Force

The most significant interaction between a charged bunch and its synchrotron radiation will be in the form of energy modulation. We will not be able to fully support this claim until we discuss the full beam dynamics in a later chapter. But for now, let us assume this is true and proceed to review the historical work along these lines. By one-dimensional, we do not necessarily mean that we are only considering line-charges, but that the effects of the finite beam extent in the transverse directions does not alter the result signficantly.

The first theory published by Schott in 1912 [8] calculated the longitudinal component of the electric field on a test charge from a point charge where both charges are moving uniformly along the same circular path, separated by angle ψ. The result is

$$\begin{aligned} E_\theta(\psi) &= -\frac{e(1-\beta^2)cos\psi}{4R^2 sin^2\psi} - \frac{e}{R^2}\sum_{m=1}^{\infty}(-1)^m cosm\psi \\ &\times \left[m\beta^2 J'_m(m\beta) - \frac{1}{2}(1-\beta^2)m^2\int_0^\beta J_m(mx)dx\right]. \end{aligned} \tag{2.40}$$

Note that Schott has separated out the singular (Coulomb) term.

We can use this model to express the result in a more general form in terms of impedance. Suppose we have a line-charge bunch which can be described by a current density in cylindrical coordinates $J_\theta(\boldsymbol{r},t) = e\beta c\lambda(\theta-\omega_0 t)\delta(r,z)$ where $\omega_0 = \beta c/R$ is the natural frequency of rotation. Then, one could define the current, $I = \int J da$, as a sum of Fourier transforms

$$I(\theta,t) = -e\beta c\sum_n \int_{-\infty}^{+\infty}\lambda_n(\omega)e^{i(n\theta-\omega t)}d\omega \tag{2.41}$$

The coefficients $\lambda_n(\omega)$ are found from

$$\lambda_n(\omega) = \frac{\delta(\omega - n\omega_0)}{2\pi} \int_0^{2\pi} \lambda(\theta') e^{-in\theta'} d\theta' \tag{2.42}$$

where $\theta' = \theta - \omega_0 t$. The longitudinal coupling impedance is defined by

$$-2\pi R E_{\theta,n}(\omega) = Z_n(\omega) I_n(\omega). \tag{2.43}$$

Using Schott's result, one can derive the impedance [30]

$$\begin{aligned} Z_n(n\omega_0) = \quad & \pi n \quad \beta Z_0 \left[J'_{2n}(2n\beta) - i E'_{2n}(2n\beta) \right] \\ & - \quad \pi n^2 \left(\frac{1-\beta^2}{\beta} \right) \int_0^{\beta} \left[J_{2n}(2nx) - i E_{2n}(2nx) \right] dx \\ & - \quad i2n \left(\frac{1-\beta^2}{\beta} \right) \left(-\frac{1}{4} \right) \ln(1-\beta^2), \end{aligned} \tag{2.44}$$

where $E_n(z)$ is the Weber function, defined by

$$J_n(z) + i E_n(z) = \frac{1}{\pi} \int_0^{\pi} d\theta e^{i(n\theta - z\sin\theta)}. \tag{2.45}$$

One can find the power loss from the real part of the impedance. The power loss is

$$\frac{dP}{dt} = -e\beta c \int E_\theta(\theta t) \lambda(\theta - \omega_0 t) d\theta. \tag{2.46}$$

We now substitute the Fourier trasformed harmonic summations

$$\frac{dP}{dt} = -e\beta c \int d\theta \int d\omega e^{-i\omega t} \sum_n E_{\theta,n}(\omega) e^{in\theta} \int d\omega' e^{-i\omega' t} \sum_{n'} \lambda_{n'}(\omega') e^{in'\theta}. \tag{2.47}$$

For the fixed bunch, we can write

$$\lambda_n(\omega) = \frac{\delta(\omega - n\omega_0)}{2\pi} \lambda_n, \tag{2.48}$$

where

$$\lambda_n = \int_0^{2\pi} \lambda(\theta') e^{-in\theta'} d\theta'. \tag{2.49}$$

Substituting,

$$\frac{dP}{dt} = -\frac{(e\beta c)^2}{2\pi R}\int d\theta \int d\omega e^{-i\omega t}\sum_n Z_n(\omega)\lambda_n(\omega)e^{in\theta}\sum_{n'}\lambda_{n'}e^{in'(\theta-\omega_0 t)}. \tag{2.50}$$

Carrying out the integrations

$$\frac{dP}{dt} = -\frac{(e\beta c)^2}{R}\sum_{n=-\infty}^{\infty} Z_n(n\omega_0)\lambda_n\lambda_{-n}. \tag{2.51}$$

Lastly we note that $\lambda_{-n} = \lambda_n^*$ and $Z_{-n}(-n\omega_0) = Z_n(n\omega_0)^*$ to write

$$\frac{dP}{dt} = -\frac{2(e\beta c)^2}{R}\sum_{n=0}^{\infty} |\lambda_n|^2 \mathrm{Re}Z_n(n\omega_0). \tag{2.52}$$

This expression is difficult to evaluate numerically, however we can approximate it within certain regimes using asymptotic expressions. When the bunch length is much larger than the critical wavelength, in which case $1 \ll n \ll n_c$ where $n_c = 3\gamma^3/2$, and the energy is high so that $\beta \approx 1$, then

$$\mathrm{Re}Z_n(n\omega_0) \approx \tfrac{1}{2}Z_0 3^{1/6}\Gamma(\tfrac{2}{3})n^{1/3}, \tag{2.53}$$

where Z_0 This scaling was first noted by Schwinger [10]. The complete asymptotic form is given is [30]

$$Z_n \sim \frac{Z_0\Gamma(\frac{2}{3})}{3^{1/3}}\left(\frac{\sqrt{3}}{2} + \frac{i}{2}\right)n^{1/3}, \tag{2.54}$$

where $Z_0 = 120\pi\ \Omega$ is the free space impedance.

2.5 Effect of Perfectly Conducting Boundaries

The presence of conducting walls will alter the propagation characteristics of the radiation. We begin by considering two infinite perfectly conducting plates

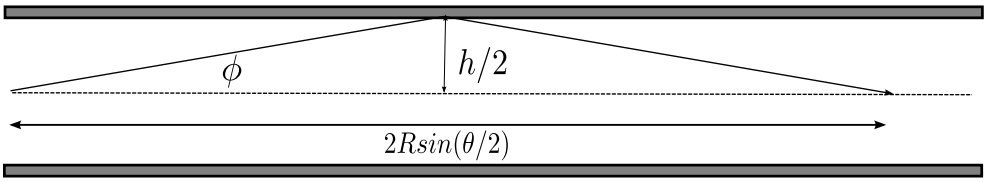

Figure 2.3: Wave propagation between infinite perfectly conducting parallel plates, above and below the plane of curvature.

located symmetrically above and below the horizontal plane, separated by distance h. In order to meet the boundary conditions, the radiation must propagate at an angle ϕ with respect to the horizontal plane which is determined by the wavelength. In order to meet the boundary conditions for two perfectly conducting plates, they are related by [31]

$$\lambda = \frac{2h\sin\phi}{m}, \quad m = 1, 2, 3... \tag{2.55}$$

Because the radiation must bounce between the plates, the group velocity in a straight line will always be less than the speed of light by the factor $\cos\phi$. The extra distance traveled by the radiation bouncing between the plates as the beam travels along the arc $R\theta$ is

$$\Delta z_{pp} = 2Rsin(\theta/2) - 2\left(R^2 sin^2(\theta/2) + h^2/4\right)^{1/2}. \tag{2.56}$$

Assuming that all angles are small,

$$\Delta z_{pp} \approx -\frac{h^2}{2R\theta}. \tag{2.57}$$

Shielding of the self-interaction from infinite parallel plates occurs when the change in propagation caused by the boundary conditions alters the self-interaction in such a manner as to negate the catch-up effect. The catch-up effect is the distance

ahead of a source that the radiation can propagate because of the shorter path taken by it. As the bunch travels along the arc, the radiation takes a path along the cord. The catch-up distance is related to the distance traveled along the arc by the characteristic equation

$$\Delta z_{cu} \approx \theta^3 R/24, \tag{2.58}$$

where R is the radius of curvature.

Equating the gain from the catch-up effect and the loss from reflection determines a critical angle

$$\theta_{crit} \approx 3^{-1/4}\sqrt{\frac{h}{2R}}. \tag{2.59}$$

This also means that

$$\phi_{crit} \approx 3^{1/4}\sqrt{\frac{h}{2R}}. \tag{2.60}$$

Finally, then we can relate this to a critical wavelength

$$\lambda_{crit} \approx \frac{3^{1/4}h^{3/2}}{(2R)^{1/2}}, \tag{2.61}$$

or in terms of wavenumber

$$k_{crit} \approx \frac{2^{3/2}\pi}{3^{1/4}}R^{1/2}h^{-3/2} \tag{2.62}$$

For wavenumbers less than k_{crit} the angle ϕ increases, θ decreases and the extra distance from reflection exceeds the gain from the catch-up effect, and the radiation can no longer interact with itself. Therefore this establishes a minimum on the wavenumber below which the radiation is effectively shielded from the self-interaction.

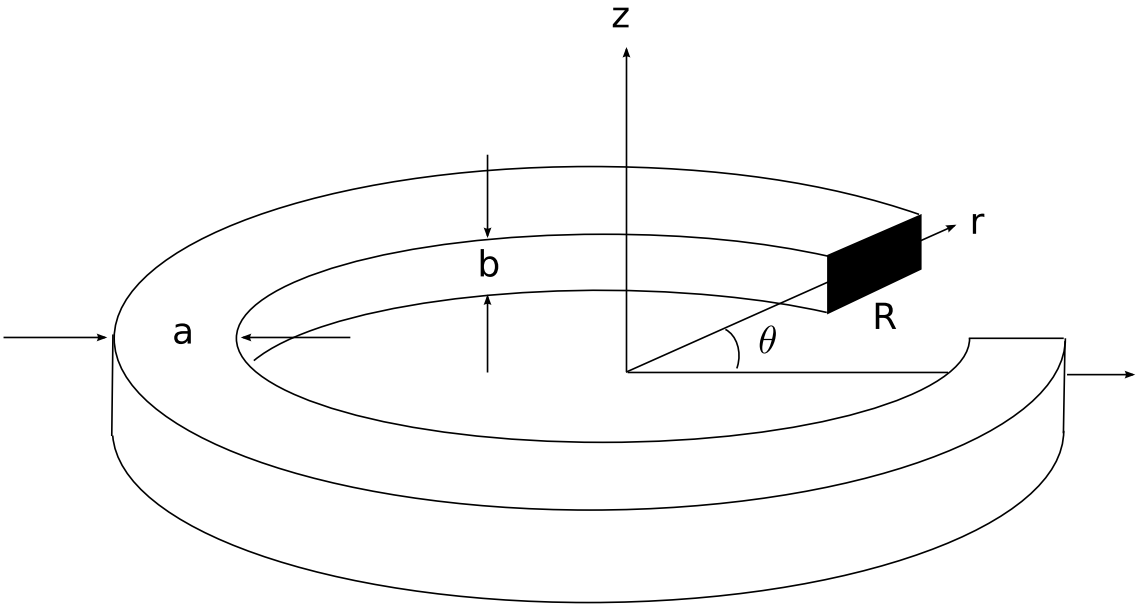

Figure 2.4: Toroidal waveguide with rectangular cross section. The bend radius is R, the width is a, and the height is b. Also shown is the cylindrical coordinate system.

The longitudinal coupling impedance for infinite parallel plates is [32]

$$\begin{aligned} Z_n(n\omega_0) &= \frac{2\pi^2 n Z_0}{\beta}\frac{R}{h}\sum_{p(odd)\geq 1}\Lambda_p\{\beta^2 J_n'(\gamma_p R)\left([J_n'(\gamma_p R)+iY_n'(\gamma_p R)\right] \\ &+ (\alpha_p/\gamma_p)^2 J_n(\gamma_p R)\left[J_n(\gamma_p R)+iY_n(\gamma_p R)\right]\}, \end{aligned} \tag{2.63}$$

where

$$\gamma_p^2 = \frac{n^2\beta^2}{R^2} - \alpha_p^2, \quad \alpha_p = \frac{p\pi}{2h}, \quad \Lambda_p = \frac{\sin(\delta h\alpha_p)}{(\delta h\alpha_p)}, \tag{2.64}$$

and the vertical size of the beam is δh.

Of course, there must also be walls in the other transverse direction in order to maintain the vacuum environment. We now consider a toroidal vacuum chamber with rectangular cross-section as shown in Fig. 2.4. The wave equation for either

E_z or B_z is

$$\left(\nabla^2 - \frac{1}{c^2}\frac{\partial^2}{\partial t^2}\right)\left\{\begin{array}{c} E_z \\ \\ B_z \end{array}\right\} = 0. \tag{2.65}$$

The solutions, assuming $\sim \mathrm{e}^{i(kR\theta-\omega t)}$ are

$$E_z(r,\theta) = \{C_1 J_{kR}(\gamma_p r) + C_2 Y_{kR}(\gamma_p r)\}\cos\left[\frac{p\pi}{b}(z+b/2)\right]\mathrm{e}^{i(kR\theta-\omega t)}, \tag{2.66}$$

$$B_z(r,\theta) = \{C_3 J'_{kR}(\gamma_p r) + C_4 Y'_{kR}(\gamma_p r)\}\sin\left[\frac{p\pi}{b}(z+b/2)\right]\mathrm{e}^{i(kR\theta-\omega t)}, \tag{2.67}$$

where

$$\gamma_p = \sqrt{\frac{\omega^2}{c^2} - \frac{p^2\pi^2}{b^2}}, \quad p = 0, 1, 2, ... \tag{2.68}$$

is the radial wavenumber.

The are two types of modes, a "TE" mode where $E_z = 0$, and a "TM" mode where $B_z = 0$ with the following dispersion relations

$$\text{TM:} \qquad J_{kR}(\gamma_p R_2)Y_{kR}(\gamma_p R_1) - J_{kR}[\gamma_p R_1]Y_{kR}(\gamma_p R_1) = 0, \tag{2.69}$$

$$\text{TE:} \qquad J'_{kR}(\gamma_p R_2)Y'_{kR}(\gamma_p R_1) - J'_{kR}(\gamma_p R_1)Y'_{kR}(\gamma_p R_2) = 0, \tag{2.70}$$

where $R_1 = R - a/2$ and $R_2 = R + a/2$. Again, for the vertical ribbon charge, the impedance in a rectangular toroidal waveguide is [32]

$$\begin{aligned} Z_n(n\omega_0) &= \frac{2i\pi^2 Z_0}{\beta}\frac{nR}{b}\sum_{p(odd)\geq 1}\Lambda_p\Big[\frac{\beta\omega_0 R}{c}\frac{s_n(\gamma_p R_2, \gamma_p R)s_n(\gamma_p R, \gamma_p R_1)}{s_n(\gamma R_2, \gamma_p R_1)} \\ &+ \left(\frac{\alpha_p}{\gamma_p}\right)^2\frac{p_n(\gamma_p R_2, \gamma_p R)p_n(\gamma_p R, \gamma_p R_1)}{p_n(\gamma R_2, \gamma_p R_1)}\Big], \end{aligned} \tag{2.71}$$

where

$$\begin{aligned} p_n(x,y) &= J_n(x)Y_n(y) - Y_n(x)J_n(y), \\ s_n(x,y) &= J'_n(x)Y'_n(y) - Y'_n(x)J'_n(y). \end{aligned} \tag{2.72}$$

Unfortunately, this form is difficult to use numerically. The bunch lengths that we will consider are such that $kR \gg 1$. Furthermore, we will want to soley focus on resonant modes that have phase velocities that are nearly the speed of light. In this case, we can define a parameter

$$\Lambda(\omega, k) = \frac{1}{2}\left(\frac{\omega^2}{k^2c^2} - 1\right) \tag{2.73}$$

that measures the difference. For very high frequencies, the perturbation caused by the curvature of the waveguide lowers the phase velocity for all modes so that resonance can occur for finite k as compared to the straight waveguide where $\Lambda \to 0$ as $k \to \infty$. In cases of interest where $\Lambda \approx 0$, the argument of the Bessel function will be $kR \gg 1$ too. Therefore, we need large argument, large order Bessel function expansions, which turn out to be the Airy functions, Ai and Bi. We can rewrite the dispersion relations

$$\text{TM:} \qquad Ai(\xi_0 - \xi_{a/2})Bi(\xi_0 + \xi_{a/2}) - Ai(\xi_0 + \xi_{a/2})Bi(\xi_0 - \xi_{a/2}) = 0, \tag{2.74}$$

$$\text{TE:} \qquad Ai'(\xi_0 - \xi_{a/2})Bi'(\xi_0 + \xi_{a/2}) - Ai'(\xi_0 + \xi_{a/2})Bi'(\xi_0 - \xi_{a/2}) = 0, \tag{2.75}$$

where

$$\xi_0 = \frac{\pi^2 p^2 R^{2/3}}{(2k^2)^{2/3}b^2} - (2k^2R)^{1/3}\Lambda, \tag{2.76}$$

$$\xi_{a/2} = \left(\frac{2k^2}{R}\right)^{1/3}\frac{a}{2} \tag{2.77}$$

The solutions of the dispersion relations will determine the wavenumbers of the resonant modes. Since we will need the synchronous mode frequencies for a square waveguide later, so we have solved for some of them numerically. For each

value of p there will be multiple solutions corresponding to $m = 0, 1, 2...$. The TM modes begin at $m = 1$ because the $m = 0$ mode does not satisfy the boundary conditions. In Table 2.1, the frequencies have been arranged in order from lowest to highest indicating the mode for each.

Table 2.1: Synchronous Modes of Square Toroidal Waveguide

$ka^{3/2}R^{-1/2}$	Mode	p	m
4.78	TE	1	0
8.78	TM	1	1
11.4	TE	3	0
12.8	TE	1	1
15.1	TM	3	1
17.4	TM	1	2
18.5	TE	3	1
21.8	TE	1	2

Chapter 3

Simulation Model and Methodology

3.1 Introduction

New designs for charged particle accelerators, particularly as drivers for free electron lasers are now in regimes of very short bunch length (picosecond or less) and very high charge per bunch (up to and exceeding 1 nanoCoulomb) [33–35]. These systems typically use bending sections either for energy recovery and/or bunch compression. In the bends the bunch will emit synchrotron radiation, characterized by a critical wavelength $\lambda_c = 3\pi R/\gamma^3$, where R is the bending radius and γ is the Lorentz factor [29]. At wavelengths smaller than the critical wavelength, the radiated power decreases rapidly. For the accelerator designs that we will consider, the critical wavelength will always be much smaller than the bunch length. However, the portion the synchrotron radiation spectrum with wavelengths greater than the bunch length will be temporally coherent. In this case, the radiated coherent synchrotron radiation (CSR) power may be larger than the equivalent incoherent synchrotron radiation by up to a factor of N, the number of electrons per bunch [10]. For a Gaussian line-charge distribution, where the electrons are distributed with rms bunch length σ_z according to

$$\rho(z) = \frac{N}{\sqrt{2\pi}\sigma_z} e^{-z^2/2\sigma_z^2}, \tag{3.1}$$

we can easily compute the coherent enhancement for a particular wavenumber k as $\approx Ne^{-(k\sigma_z)^2}$ which is obviously large whenever $k\sigma_z \ll 1$. In this case, the coherent portion of radiation from a bunched charge transiting a bend, which is greatly enhanced over the usual incoherent synchrotron radiation, may interact with itself in a way that will increase the transverse emittance. Simple estimates of the growth of transverse emittance from longitudinal CSR indicate that this may be a serious problem for high brightness electron beams [18].

There are other factors that may enhance or mitigate the effect of CSR in bending systems. The presence of perfectly conducting walls as infinite parallel plates above and below the plane of motion restricts the CSR fields which can interact with the radiating bunch to wavelengths $\lambda \ll h^{3/2}R^{-1/2}$, where h is the gap size [11, 12]. In the presence of conducting walls in the form of a waveguide, the modes must have phase velocity close to the speed of the bunch and therefore have a maximum wavelength which scales similarly as in the case of infinite parallel plates with gap size h, but where h is replaced by the characteristic dimension of the waveguide a, the smaller of either the height or width [16, 17]. This restricts the range of CSR wavelengths to a band, limited below by the synchronous phase velocity requirement, and above by coherence, such that $\sigma_z \ll \lambda \ll a^{3/2}R^{-1/2}$.

Additionally, the effects from transverse fields can be significant and of comparable magnitude as the longitudinal forces [36, 37]. However the calculation of these transverse effects depend critically on the shape of the transverse charge distribution. Lastly we can postulate that in the presence of the actual beam dynamics including dispersion, energy spread, betatron motion, energy chirp and the resulting

compression/decompression the actual situation may drastically vary from the ideal conditions assumed in the theoretical predictions. For these reasons, in order to obtain an accurate estimate of the potential effect of CSR and space-charge under dynamical conditions, we must develop simulation methods that include as much as possible. However, before the complications of beam dynamics are introduced, it is important to establish the capability of a such a simulation to accurately calculate the CSR fields to the extent that there is theory to compare with. So as a starting point, we remove the complexity of the beam dynamics and establish as a minimum goal to model the CSR and space-charge forces from a three-dimensional charge distribution traveling on a curved path inside a rectangular waveguide

The simulation of the CSR force in a rectangular waveguide was first accomplished by numerical integration of a wave equation, originally derived in [22], in the *frequency domain* (i.e. Fourier transform in the longitudinal coordinate), using a three-dimensional grid [23]. Later, modifications of the basic equations were made to include space-charge [21] and the effect of resistive walls [38, 39]. Starting with the same wave equation, we have developed an unconditionally stable, unitary integration method in the *time domain*, using a different set of boundary conditions in the longitudinal coordinate. As a result, we can simulate a single bunch in curved and straight sections in a manner that strictly enforces causality, and is free from any restriction of the simulation length. Additionally, we have extended and fully developed this method for an arbitrary, dynamic three-dimensional charge distribution including the effects of space-charge. In the following sections, we review the theoretical development, describe our method in detail and compare results to

theory where possible.

3.2 Simulation Model and Method

3.2.1 Theoretical Model

To model the effects of CSR on an electron beam, we must be able to calculate the electromagnetic fields $\boldsymbol{E}$ and $\boldsymbol{B}$ as driven by charge density ρ and current density $\boldsymbol{J}$. The evolution of these fields is described by Maxwell equations in vacuum. By simple manipulation, we can form wave equations (using Gaussian units)

$$\nabla^2 \boldsymbol{E} - \frac{1}{c^2}\frac{\partial^2}{\partial t^2}\boldsymbol{E} = \frac{4\pi}{c^2}\frac{\partial}{\partial t}\boldsymbol{J} + 4\pi\nabla\rho, \tag{3.2}$$

$$\nabla^2 \boldsymbol{B} - \frac{1}{c^2}\frac{\partial^2}{\partial t^2}\boldsymbol{B} = -\frac{4\pi}{c}\nabla \times \boldsymbol{J}, \tag{3.3}$$

where $c = 2.998 \times 10^{10}$ cm/s is the speed of light in vacuum. We now define the usual accelerator coordinate system which follows a reference particle a total distance s from an arbitrary origin along the design trajectory as shown in Fig. 3.1. For our purposes, the reference trajectory with Lorentz factor γ_0 will only be either straight, corresponding to drift sections or uniformly bending with constant radius R, so we use a cylindrical coordinate system and set $R \to \infty$ for drift sections. We can then specify coordinates as deviations from the reference trajectory. In the longitudinal coordinate, we define $z = s - \beta_0 \tau$ where $\beta_0 = (1 - \gamma_0^{-2})^{1/2}$ and $\tau = ct$. In the transverse directions we define $x = r - R$ as the transverse coordinate in the bending plane, and y as the vertical displacement from the bending plane. Next we write the wave equations for the transverse electric fields, denoted by the subscript

$\perp$. Assuming the that the transverse current density $\boldsymbol{J}_\perp$ is negligible,

$$\left(\nabla^2 - \frac{\partial^2}{\partial\tau^2} + 2\beta_0\frac{\partial^2}{\partial z\partial\tau} - \beta_0^2\frac{\partial^2}{\partial z^2}\right)\boldsymbol{E}_\perp = 4\pi\nabla_\perp\rho. \tag{3.4}$$

Next, we make the assumption that the deviation from the reference trajectory in the bending plane is small compared to the bending radius. If the width of our vacuum waveguide is a, then we state this more precisely as the restriction that $x/R < a/R \equiv \delta^2 \ll 1$, where δ is a small parameter representing the effect of curvature. Additionally we assume the reference trajectory is such that $\gamma_0^2 >> 1$, where $\gamma_0 = (1-\beta_0^2)^{-1/2}$ so that we may make the expansion $\beta_0 \approx 1 - 1/2\gamma_0^2$. Lastly, we neglect solutions to Eq. (3.4) that are not *paraxial*, propagating at a small angle to the beam axis. More specifically, we ignore the second derivative $\partial^2/\partial\tau^2$ relative to other terms. We restrict ourselves to the consideration of waves with wavenumbers far from the waveguide cutoff, $k \gg a^{-1}$, that propagate very nearly along the longitudinal axis. For a sustained interaction, the modes must also propagate at a similar speed (phase velocity) as the beam. As discussed in the introduction, this restricts our description to forward wave solutions $\sim e^{i(kz-\omega t)}$ with wavenumbers $ka \gg \delta^{-1}$. This leads us to a parabolic wave equation [40] for the transverse electric fields, where we only keep terms to $\sim O(\delta, \gamma^{-2})$, now given by

$$\frac{\partial^2\boldsymbol{E}_\perp}{\partial z\partial\tau} = -\frac{1}{2}\left[\nabla_\perp^2 + \left(\frac{1}{\gamma^2} - \frac{2x}{R}\right)\frac{\partial^2}{\partial z^2}\right]\mathbf{E}_\perp + 2\pi\nabla_\perp\rho, \tag{3.5}$$

where the function $O()$ denotes order-of-magnitude.

The boundary conditions for $\boldsymbol{E}$ in a waveguide with perfectly conducting walls

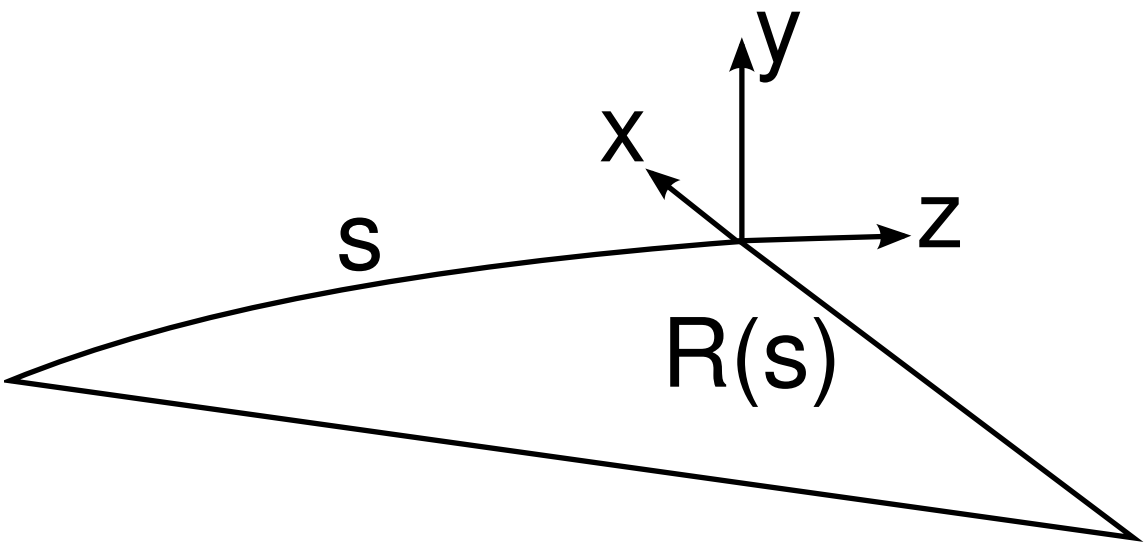

Figure 3.1: Accelerator coordinate system. At any given distance s along the reference trajectory, we can assume a local radius of curvature $R(s)$. Deviations in the transverse directions are given by x (in the bending plane) and y (perpendicular to the bending plane).

are

$$\hat{\boldsymbol{n}} \times \boldsymbol{E}\Big|_S = 0 \tag{3.6}$$

where $\hat{\boldsymbol{n}}$ is the unit vector normal to the surface. Clearly $E_z|_S = 0$. Additionally, we require that there are no charges in contact with the walls, so that $\rho|_S = 0$, also implying $\nabla \cdot \boldsymbol{E}|_S = 0$. Therefore we can derive the boundary condition for the normal component of the electric field at the rectangular waveguide walls

$$\frac{\partial}{\partial n}\hat{\boldsymbol{n}} \cdot \boldsymbol{E}\Big|_S = 0, \tag{3.7}$$

keeping in mind that this too will only need be evaluated to the same order of approximation with respect to δ.

To $O(\delta, \gamma^{-2})$, we can calculate all other field quantities as functions of only the transverse electric fields and the charge density. This will be particularly important

when applied to a simulation method, because it reduces the storage requirements from six fields to just two. We now describe how this can be accomplished.

To calculate the longitudinal electric force $F_z = eE_z$ we use Gauss' law $\nabla \cdot \mathbf{E} = 4\pi\rho$, where we can neglect the x-dependence, $(1+x/R)^{-1}\partial F_z/\partial z \approx \partial F_z/\partial z$, because F_z is already $O(\delta)$, yielding

$$F_z(z) = e\int_z^\infty (\nabla_\perp \cdot \boldsymbol{E}_\perp - 4\pi\rho)\, dz', \tag{3.8}$$

where we have exploited the fact that $F_z(\infty) = 0$. To calculate the transverse Lorentz force $\boldsymbol{F}_\perp = e\,[\boldsymbol{E}_\perp + (\boldsymbol{\beta} \times \boldsymbol{B})_\perp]$, we first transform Faraday's law into the co-moving reference frame,

$$\nabla \times \boldsymbol{E} = \beta_0 \frac{\partial \boldsymbol{B}}{\partial z} - \frac{\partial \boldsymbol{B}}{\partial \tau}. \tag{3.9}$$

Here we will assume that the energy spread is small so that $\beta \approx \beta_0$. If the energy deviation is $\Delta\gamma \equiv \gamma - \gamma_0$ then $\beta - \beta_0 \approx \Delta\gamma/\gamma_0^3$ which will always be met for $\gamma_0^2 \gg 1$. Next we note that to the same order of approximation, $B_y = \beta E_x$. Therefore Eq. (3.9) can be rearranged, again neglecting all terms involving x because $F_\perp \sim O(\delta^2)$ already, and integrated to yield the following equations for the transverse Lorentz forces,

$$\boldsymbol{F}_\perp(z) = -\int_z^\infty \left(\nabla_\perp F_z - e\beta \frac{\partial}{\partial \tau}\boldsymbol{E}_\perp\right) dz'. \tag{3.10}$$

Neglecting the time derivative, Eq. (3.10) is exactly what one would have obtained using the Panofsky-Wentzel theorem [41]. We expect that the time derivative term should be small, but unfortunately cannot be neglected for an accurate calculation, because it of the same order as $\nabla_\perp F_z$ (best seen by comparing terms in Eq. (3.5)).

In steady-state it will be identically zero, in which case we could have derived the fields in terms of retarded potentials Φ and $\boldsymbol{A}$.

We start by expressing the electric and magnetic fields in terms of potentials ϕ and $\boldsymbol{A}$,

$$\boldsymbol{E} = -\nabla\phi - \frac{1}{c}\frac{\partial}{\partial t}\boldsymbol{A} \tag{3.11}$$

$$\boldsymbol{B} = \nabla \times \boldsymbol{A}. \tag{3.12}$$

The force felt by a test particle moving at speed βc along an arc of a circle with radius r is given by the Lorentz force law

$$\boldsymbol{F} = e\left[\boldsymbol{E} + \boldsymbol{\beta} \times \boldsymbol{B}\right]. \tag{3.13}$$

In a cylindrical coordinate system $\{r, \theta, z\}$ if we take the particle's motion to be in the θ-direction, we have the two following components:

$$F_r = e\left(-\frac{\partial\phi}{\partial r} - \frac{1}{c}\frac{dA_r}{dt} + \frac{\beta}{r}\frac{\partial}{\partial r}rA_\theta\right), \tag{3.14}$$

$$F_\theta = e\left(-\frac{1}{r}\frac{\partial\phi}{\partial\theta} + \frac{\beta}{r}\frac{\partial A_\theta}{\partial\theta} - \frac{1}{c}\frac{dA_\theta}{dt}\right), \tag{3.15}$$

where we have substituted the total time derivative defined by

$$\frac{d}{dt} = \frac{\partial}{\partial t} + \frac{\beta c}{r}\frac{\partial}{\partial\theta}. \tag{3.16}$$

Subsequently, we neglect the total time derivative, consistent with our approach of using the paraxial wave equation where the fields evolve slowly in the co-moving reference frame.

Lastly, we compute the difference in the derivatives as follows:

$$\frac{1}{r}\frac{\partial F_r}{\partial\theta} - \frac{\partial F_\theta}{\partial r} = \frac{e}{r}\left(-\frac{1}{r}\frac{\partial\phi}{\partial\theta} + \frac{\beta}{r}\frac{\partial A_\theta}{\partial\theta}\right), \tag{3.17}$$

noting that the right hand side is F_θ/r if we neglect the total derivative. Rearranging terms, we have

$$\frac{1}{r}\frac{\partial F_r}{\partial \theta} = \frac{\partial F_\theta}{\partial r} + \frac{F_\theta}{r}. \tag{3.18}$$

This is essentially Eq.(3.10) if we change variables to $x = r - R$ and $z = R\theta$ and neglect small terms in $x/R \ll 1$. Keeping terms to the same order, we obtain the steady-state Lorentz forces

$$F_x = -e\frac{\partial V_0}{\partial x} + \frac{eA_z}{R} \tag{3.19}$$

$$F_y = -e\frac{\partial V_0}{\partial y} \tag{3.20}$$

$$F_z = -e\frac{\partial V_0}{\partial z}. \tag{3.21}$$

where $V_0 = (\Phi - \boldsymbol{\beta} \cdot \boldsymbol{A})$.

In steady-state Eq. (3.10) is identical with the results from this approach. The second term in the equation for F_x is the Talman force [15] which causes some difficulty for line charge models since it is logarithmically divergent as we take the limit of small transverse dimensions. It is shown here because we will need it to correctly derive the theoretical model for the transverse forces. The effect on the transverse dynamics is thought to be largely canceled by the change in energy from space-charge forces (also logarithmically divergent) and so can be removed for linear models [42, 43]. The extent to which these effects cancel is a subject of debate [37, 44] and something our model may prove useful in resolving once we add the bunch dynamics. The problem of divergence, however, does not exist for three-dimensional models.

In free-space, we can solve for the retarded potentials [45]

$$\Phi(\boldsymbol{r},t) = \int \frac{d^3 r_1 \rho(\boldsymbol{r}_1, t-\tau)}{D_{ret}}, \tag{3.22}$$

$$\boldsymbol{A}(\boldsymbol{r},t) = \int \frac{d^3 r_1 \boldsymbol{\beta}_1 \rho(\boldsymbol{r}_1, t-\tau)}{D_{ret}}, \tag{3.23}$$

where $D_{ret} = |\boldsymbol{r} - \boldsymbol{r}_1|$, and $\tau = D_{ret}/c$. With a constant curvature radius of R, and in the case where we can write the charge distribution as the product of transverse and longitudinal distributions, $\rho(\boldsymbol{r}') = \Phi(\boldsymbol{x}'_\perp)\lambda(z')$ we can cast Eqs. (3.22, 3.23) into a form suitable for numerical integration

$$\begin{aligned} V_0(\boldsymbol{r}) &= \int \Phi(\boldsymbol{x}'_\perp)\left[1-\beta(x')\beta_0\cos(\xi/R)\right] \\ &\times \frac{\lambda[z+\xi+\beta(x')D_{ret}(\boldsymbol{x}'_\perp,\xi)]}{D_{ret}(\boldsymbol{x}'_\perp,\xi)} d\boldsymbol{x}'_\perp d\xi, \end{aligned} \tag{3.24}$$

$$\begin{aligned} A_z(\boldsymbol{r}) &= \int \Phi(\boldsymbol{x}'_\perp)\beta(x')\cos(\xi/R) \\ &\times \frac{\lambda[z+\xi+\beta(x')D_{ret}(\boldsymbol{x}'_\perp,\xi)]}{D_{ret}(\boldsymbol{x}'_\perp,\xi)} d\boldsymbol{x}'_\perp d\xi, \end{aligned} \tag{3.25}$$

$$\begin{aligned} D_{ret} &= [(R+x)^2 + (R+x')^2 - \\ &\times 2(R+x)(R+x')\cos\left(\frac{z'-z}{R}\right) + (y-y')^2]^{1/2}, \end{aligned} \tag{3.26}$$

where $\xi = z' - z$. We have allowed for a variation in β with distance x from the reference trajectory, contrary to our previous assumption where $\beta \approx \beta_0$. This will not alter our results later in this paper, because we will always calculate the forces along the reference trajectory where $\beta = \beta_0$ identically. The variation in β for the source, however will be necessary for an accurate comparison with theoretical calculations of the transverse force where a rigid bunch has been assumed. To keep the bunched charge distribution fixed despite moving through a dispersive bending section, we need a linear velocity shear such that $\beta(x') = \beta_0(1 + x'/R)$.

The integrations in Eqs.(3.24,3.25) are over two distinct regions. When $\xi < 0$, the tail-to-head interaction regime, the radiation slowly overtakes the bunch from behind. This is the usual effect associated with CSR. The fields from the tail-to-head interaction build up slowly and only reach steady-state when the overtaking length is longer than the bunch length. We also integrate over $\xi > 0$, head-to-tail interaction regime, the effect is felt almost instantaneously as the radiation and charge run towards each other. For the longitudinal force, only the tail-head interaction is significant, but for the transverse force, the head-to-tail component coming from the A_z/R is dominant.

3.2.2 Comparison with Previous Work

In [23] the authors claim to have developed a method for the calculation of the transverse force using only the integrated values of $\boldsymbol{E}_\perp$. They claim

$$F_x = \frac{i}{2k}\left(\frac{\partial B_s}{\partial y} - \frac{\partial E_s}{\partial x}\right), \tag{3.27}$$

where the quantities are Fourier transforms defined by

$$f(t,s) = \frac{1}{2\pi}\int_{-\infty}^{\infty} f(k,s)e^{ik(s-t)}dk \tag{3.28}$$

so that spatial derivatives are replaced by the Fourier equivalents using

$$\frac{\partial f(t,s)}{\partial s} \leftrightarrow ikf(k,s) + \frac{\partial f(k,s)}{\partial s}. \tag{3.29}$$

Note that the distance s along the reference trajectory has been retained as the independent variable.

In our work, we do not use the Fourier domain, and the transverse force is calculated by Eq. (3.10). Neglecting the time derivative, and taking the longitudinal derivative of the x-component, we have

$$\frac{\partial F_x}{\partial z} = -\frac{\partial E_z}{\partial x}. \tag{3.30}$$

Now, taking the Fourier transform in the z-direction and noting the equivalence of the z and s directions, and the sign difference between the t and z variables, we obtain our version in the same notation as Ref [23]

$$F_x(s,k) = -\frac{i}{k}\frac{\partial E_s}{\partial x}. \tag{3.31}$$

The obvious difference is the omission of the term involving B_s and the factor of 2. We demonstrate in our paper that our equation matches theory in two steady-state cases in vacuum:

1. The limit of $R \to \infty$, and

2. For a rigid source moving along the arc of a circle.

In [23], $\gamma = \infty$, therefore case (1) should be identically zero. Unfortunately, the derivation did not include finite γ and therefore is not helpful. Even assuming $\gamma \to \infty$, the solution for free-space potentials is given in Eq. (3.23).

Clearly, if $\boldsymbol{\beta}_y = 0$, then $A_y = 0$, and therefore $B_s = -\partial A_x/\partial y$. If we calculate the value of B_s along the s-axis, we now can show it will be identically zero if the source distribution is even in y_1. Suppose that the source is even composed of the product of transverse and longitudinal distributions such that $\rho(\boldsymbol{r}_1) = \phi(x_1, y_1)\lambda(z-$

βct), where the transverse distribution is least even in y_1. Then using Eqn. (3.23) we can write an expression for the magnetic field

$$B_s(x,y,z,t) = \int d^3r_1 \beta_x \phi(x1,y1) \frac{\partial}{\partial y}\left(\frac{\lambda[z-\beta ct-\beta D_{ret}]}{D_{ret}}\right). \tag{3.32}$$

Evaluating the derivative

$$\begin{aligned} &\frac{\partial}{\partial y}\left(\frac{\lambda[z-\beta ct-\beta D_{ret}]}{D_{ret}}\right) = \\ &(y-y1)\left(\frac{\lambda'[z-\beta ct-\beta D_{ret}]}{D_{ret}^2} - \frac{\lambda[z-\beta ct-\beta D_{ret}]}{D_{ret}^3}\right). \end{aligned} \tag{3.33}$$

When evaluated at $y = 0$, this makes the integrand an odd function of y_1 and therefore $B_s = 0$.

Thus, the second term in Eqn. (3.27) does not contribute to this case, meaning our equations differ exactly by a factor of two (in steady-state). Since we have sucessfully compared our method to theory both in the case of $R \to \infty$ and for steady-state circular motion, we claim that the Eqn. (3.27) was incorrectly derived. No details of the derivation are provided in [23], therefore it is impossible to find the error. However, details are given in [39] which might allow us to identify the problem. The author attempts to remove the s-dependent terms by adding the Faraday and Ampere Maxwell equations. The error surely must occur in the Fourier transform of Ampere's law,

$$\frac{1}{c}\frac{\partial E_x}{\partial t} = (\nabla \times \boldsymbol{B})_x - \frac{4\pi}{c} J_x. \tag{3.34}$$

Taking the Fourier transform we have

$$-ik\tilde{E}_x = \frac{1}{(1+x/R)}\left(\frac{\partial(1+x/R)\tilde{B}_s}{\partial y} - \frac{\partial \tilde{B}_y}{\partial s} - ik\tilde{B}_y\right). \tag{3.35}$$

Solving for $\tilde{B}_y$,

$$\tilde{B}_y = (1 + x/R)\tilde{E}_x + \frac{i}{k}\frac{\partial \tilde{B}_y}{\partial s} - \frac{i}{k}\frac{\partial (1 + x/R)\tilde{B}_s}{\partial y} \tag{3.36}$$

In [23], however, quoting Eqn. (2.39), the author concludes that

$$B_y = + \left(1 + \frac{x}{\rho}\right) E_x - \frac{i}{k}\frac{\partial E_x}{\partial s} - \frac{i}{k}\frac{\partial B_s}{\partial y} \tag{3.37}$$

is the correct expansion to $O(x/\rho)$, where the author has used ρ for the radius of curvature which is R in our notation. Perhaps the author wanted to exchange $B_y \sim E_x$, but the sign appears incorrect. Or perhaps the author indavertently exhanged the independent variables. Regardless, the cancelation of the s-dependent terms does not seem to work. Furthermore it does not lead to the same answer as we have obtained even in steady-state. By contrast, in our paper we have provided a detailed derivation and sucessfully compared the results with established theory for a rigid three-dimensional charge distribution with finite γ in free space.

We conclude that the method to calculate the transverse force in [23] is incorrect. Specifically that the second term involving B_s is identically zero on the $s-$axis for a symmetric charge distribution, and therefore even in the steady-state case, would predict a value exactly one-half of our expression. Additionally, the modification for finite γ in the integration equations would also require modifiying the method for calculating the transverse force since it appears it will not work as is, again disagreeing by a factor of two from our method. Furthermore the expression is missing terms involving time derivatives which probably come from an erroneous derivation. Our conclusions are based on a detailed derivation and comparision

with theory for the limiting cases of a rigid source in free space for our method, two counter-examples and a review of [23, 39].

3.2.3 Simulation Method

We now describe the method we use to integrate Eq. (3.5). This has previously been accomplished for a rigid line charge using a Fourier transform in z, where the transverse fields can be written [23]

$$\boldsymbol{E}_\perp(x,y,z,\tau) = \int_{-\infty}^{\infty} \tilde{\boldsymbol{E}}_\perp(x,y,k,\tau)e^{ikz}dk. \tag{3.38}$$

This form is quite useful for analysis or for simulation of a line charge, however it presents some difficulty for numerical simulation of a three-dimensional and possibly dynamic source. Firstly, note that we will be approximating the fields on a three-dimensional grid. For a sampling window size from $-c/2$ to $+c/2$ with N grid points, the sampling locations are $z_l = -c/2 + lc/N$ with $l = 0, 1, 2....$ Since the fields will be sampled on discrete intervals, we need to use a Discrete Fourier Transform [46]

$$\boldsymbol{E}_\perp(z_l,\tau) = \sum_{q=0}^{N} \boldsymbol{E}_q e^{ik_q z_l} \tag{3.39}$$

where $k_q = 2\pi q/c$ for $q = 0, 1, 2...N$ are the discrete wavenumbers. This form makes the fields periodic in z with interval c. In a waveguide section such as we are simulating, there are some frequency components which will propagate with group velocity much slower than the bunch speed. A derivation of the group and phase velocities is given later in this section. If the beam stimulates these modes as it converges/diverges, they will quickly fall behind and if care is not taken, could reappear ahead of the bunch because of the periodic boundary conditions implicit in the

Discrete Fourier Transform. If the computational domain is not actually periodic, this *wrap-around* effect could contaminate the fields and furthermore violate the causality condition where signals cannot propagate faster than the speed of light.

Our goal is to efficiently simulate the CSR and space-charge fields from a three dimensional single bunch, or as an approximation, a train of bunches that are separated by distances much greater than the bunch length while adequately resolving the forces within the bunch. This may be in individual sections or combinations of sections that are either straight and uniformly curved. Because of the difficulty associated with the wrap-around effect, we have developed a method that does not use periodic boundary conditions. Instead, we use a *time domain* method in the spatial variable z to integrate the paraxial wave equations, instead of a *frequency domain* method in the frequency variable k. We can choose the behavior at the boundaries (in z) as desired. To simulate a single bunch, at the boundary ahead of the bunch, at $z = +c/2$, we choose to set the fields to zero because it may be easily chosen to be sufficiently far enough ahead of the bunch that no radiation could ever reach it. On the other hand, for the same situation, we let any radiation passing the boundary behind the bunch, at $z = -c/2$, simply pass through as if the boundary were transparent. As long as the rear boundary is far enough away that radiation propagating to the rear boundary cannot reverse itself and come forward again then the situation should be adequately representative of our model. We can therefore still use a relatively small (in z) window about the center of the bunch with a reasonable size, on the order of 10-20 σ_z, which both models the physical situation and is computationally efficient. The transition between sections is accomplished

by simply changing the value of R and continuing to advance the fields. For straight sections, $\kappa = 1/R = 0$, and for curved sections, R is set to bending radius of the reference trajectory. The bending radius could change within a bending section but for our purposes does not.

To devise a stable integration scheme in the time domain, we found it necessary to use spectral methods in the transverse directions, where the transverse dependence is written as a series of eigenfunctions. We use either sine or cosine expansions that meet the boundary conditions in Eqs. (3.6, 3.7) for perfectly conducting walls in a waveguide channel width a and height b. The transverse fields are written as

$$E_x = \sum_{m,n=0}^{\infty} \tilde{E}_x e_x^{m,n}, \tag{3.40}$$

$$E_y = \sum_{m,n=0}^{\infty} \tilde{E}_y e_y^{m,n}, \tag{3.41}$$

where

$$\left\{ \begin{array}{c} e_x^{m,n} \\ e_y^{m,n} \end{array} \right\} = \left\{ \begin{array}{c} \cos[k_n(x-a/2)]\sin[k_m(y-b/2)] \\ \sin[k_n(x-a/2)]\cos[k_m(y-b/2)] \end{array} \right\}, \tag{3.42}$$

and $k_n = n\pi/2a$, $k_m = m\pi/2b$. The exact boundary conditions at $y = \pm b/2$ are $E_x = 0$ and $\partial E_y/\partial y = 0$. At $x = \pm a/2$, $E_y = 0$, but the exact form of Eq. (3.7) is

$$\frac{\partial E_x}{\partial x} + \frac{E_x}{R+x}\Big|_{x=\pm a/2} = 0. \tag{3.43}$$

Since we have only retained terms to $O(\delta)$, we can also replace the boundary condition by its approximation to the same order,

$$\frac{\partial E_x}{\partial x}\Big|_{x=\pm a/2} \approx 0. \tag{3.44}$$

Therefore our eigenfunctions meet the boundary conditions individually, which in turn allows us to use an implicit method for advancing the fields because we are guaranteed to satisfy the boundary conditions area each step. By implicit method, we mean that we can algebraically solve for the updated value at a particular time using both the previous value and current value to approximate the derivative.

3.3 Symmetry and the Paraxial Wave Equation

Returning to the basic paraxial wave equation that is the basis of our model, Eq. (3.4), if we initially construct the charge distribution with symmetry in the y-direction, such that $\rho(x, y, z, 0) = \rho(x, -y, z, 0)$, then we may suspect that the symmetry of the solution will depend only on the symmetry of the right hand side. This occurs because the operator on the left hand side is completely symmetric in y. However, we should also take care to examine the boundary conditions. Therefore let us examine E_x and E_y separately.

We make the substitution $y \to -y$ in each component of Eq. (3.4)

$$\left(\nabla^2 - \frac{\partial^2}{\partial\tau^2} + 2\beta_0\frac{\partial^2}{\partial z\partial\tau} - \beta_0^2\frac{\partial^2}{\partial z^2}\right)E_x(y) = 4\pi\frac{\partial\rho(y)}{\partial x} \tag{3.45}$$

$$\left(\nabla^2 - \frac{\partial^2}{\partial\tau^2} + 2\beta_0\frac{\partial^2}{\partial z\partial\tau} - \beta_0^2\frac{\partial^2}{\partial z^2}\right)E_x(-y) = 4\pi\frac{\partial\rho(y)}{\partial x} \tag{3.46}$$

$$\left(\nabla^2 - \frac{\partial^2}{\partial\tau^2} + 2\beta_0\frac{\partial^2}{\partial z\partial\tau} - \beta_0^2\frac{\partial^2}{\partial z^2}\right)E_y(y) = 4\pi\frac{\partial\rho(y)}{\partial y} \tag{3.47}$$

$$\left(\nabla^2 - \frac{\partial^2}{\partial\tau^2} + 2\beta_0\frac{\partial^2}{\partial z\partial\tau} - \beta_0^2\frac{\partial^2}{\partial z^2}\right)E_y(-y) = -4\pi\frac{\partial\rho(y)}{\partial y} \tag{3.48}$$

Now, we examine the boundary conditions at $y = \pm b/2$.

$$E_x(y = \pm b/2) = 0 \tag{3.49}$$

$$\left.\frac{\partial E_y}{\partial y}\right|_{y=\pm b/2} = 0. \tag{3.50}$$

At $y = 0$ we also require

$$E_{x,y}(0^-) = E_{x,y}(0^+) \tag{3.51}$$

$$\left.\frac{\partial E_{x,y}}{\partial y}\right|_{0^-} = \left.\frac{\partial E_{x,y}}{\partial y}\right|_{0^+} \tag{3.52}$$

by simply stating that the charge distribution must be continuous there.

We now see that if we divide the region into two sub-regions, one from $y = 0$ to $y = b/2$ and one from $y = 0$ to $y = -b/2$, that the paraxial wave equations satisfied by E_x are exactly the same and have the same boundary conditions, and therefore must have identical solutions. Thus E_x must be symmetric with respect to y. Similarly E_y satisfies the same equation and boundary conditions with the exception that the source is negative, therefore E_y must be odd with respect to y.

3.4 Description of Symmetry using Basis Functions

Since E_x is even with respect to y and E_y is odd with respect to y we find that we can eliminate half of the basis eigenfuctions in the description of each. Specfically, the y-dependence of E_x is expressed using eigenfunctions of the form

$$E_x \sim \sin[k_m(y - b/2)]. \tag{3.53}$$

These functions are either even or odd with respect to y. In fact

$$\sin[k_m(y-b/2)] = -\sin[k_m(-y-b/2)], m=2,4,... \tag{3.54}$$

$$\sin[k_m(y-b/2)] = \sin[k_m(-y-b/2)], m=1,3,... \tag{3.55}$$

Therefore, E_x can be described using only the odd-numbered basis fuctions (with respect to y) in the case where the source is always symmetric with respect to y. Similarly,

$$\cos[k_m(y-b/2)] = \cos[k_m(-y-b/2)], m=0,2,4,... \tag{3.56}$$

$$\cos[k_m(y-b/2)] = -\cos[k_m(-y-b/2)], m=1,3,... \tag{3.57}$$

so we see that E_y can also be described using only the odd-numbered basis functions in the same situation.

As an immediate test of validity, consider the steady-state case in which there is no curvature of the waveguide. We aready know how to solve for the fields

$$\hat{\boldsymbol{E}}_{\perp}^{ss}(\boldsymbol{k}) = \frac{4\pi \boldsymbol{k}_{\perp}\hat{\rho}(\boldsymbol{k})}{k_{\perp}^2 + k_z^2/\gamma^2}. \tag{3.58}$$

It is clear that if $\hat{\rho}$ is zero for all even wavenumbers by symmetry, then the steady state fields also are zero for all even wavenumbers. The paraxial wave equation for a curved waveguide does not introduce any terms with a y-dependence, therefore we may safely assume nothing is changed.

The use of these eigenfunctions also allow us to easily compute the transverse spatial derivatives (from the $\nabla_{\perp}^2$ operator) with spectral accuracy. However this is inconsistent with terms involving x, so we need to split the transverse operator into

two parts and integrate them separately and sequentially. This technique is know as *the method of fractional steps* [47]. Eq. (3.5) then becomes two equations

$$\frac{\partial^2 \tilde{\boldsymbol{E}}_\perp}{\partial z \partial \tau} = \frac{1}{2} k_\perp^2 \tilde{\mathbf{E}}_\perp + 2\pi \boldsymbol{k}_\perp \tilde{\rho}, \tag{3.59}$$

$$\frac{\partial \boldsymbol{E}_\perp}{\partial \tau} = \left(\frac{x}{R} - \frac{1}{2\gamma^2} \right) \frac{\partial}{\partial z} \mathbf{E}_\perp, \tag{3.60}$$

where $\tilde{E}_\perp$ are the expansion coefficients. Eqs. (3.59) and (3.60) are integrated sequentially for each time step, using a Fast Fourier Transform method to change in and out of transverse eigenfunction space each step.

We now discretize the fields on a uniform mesh $x_i = a(i/N_x - 1/2)$ where $i = 0, 1, 2...N_x$ and similarly for y_j and z_l, as well as for time $\tau_n = n\Delta\tau$. For Eq. (3.59) we use an implicit finite difference method using only the points as illustrated in Fig. 3.2. Because we are only using points that are at or ahead (in z) of the point we are currently solving for, there is no mechanism for information to travel forward. As we will demonstrate later, the group velocity for all frequencies that are solutions to Eq. (3.59) are negative and therefore cannot propagate forward. Therefore, by using on the points as shown in Fig. 3.2 we are enforcing causality for this step. The discrete form of Eq. (3.59) is

$$\tilde{\boldsymbol{E}}_{\perp,l}^{n+1} = \frac{1-q}{1+q} \left(\tilde{\boldsymbol{E}}_{\perp,l+1}^{n+1} + \tilde{\boldsymbol{E}}_{\perp,l}^{n} \right) - \tilde{\boldsymbol{E}}_{\perp,l+1}^{n} + \pi \boldsymbol{k}_\perp \Delta\tau \Delta z (\tilde{\rho}_{l+1} + \tilde{\rho}_l), \tag{3.61}$$

where $q = k_\perp^2 \Delta\tau \Delta z/8$. Because the scheme needs to be initialized, we begin at the forward boundary and integrate from front to back, again consistent with causality. Note that the source term is fixed in this scheme, but could easily be advanced self-consistently under the influence of the electromagnetic fields.

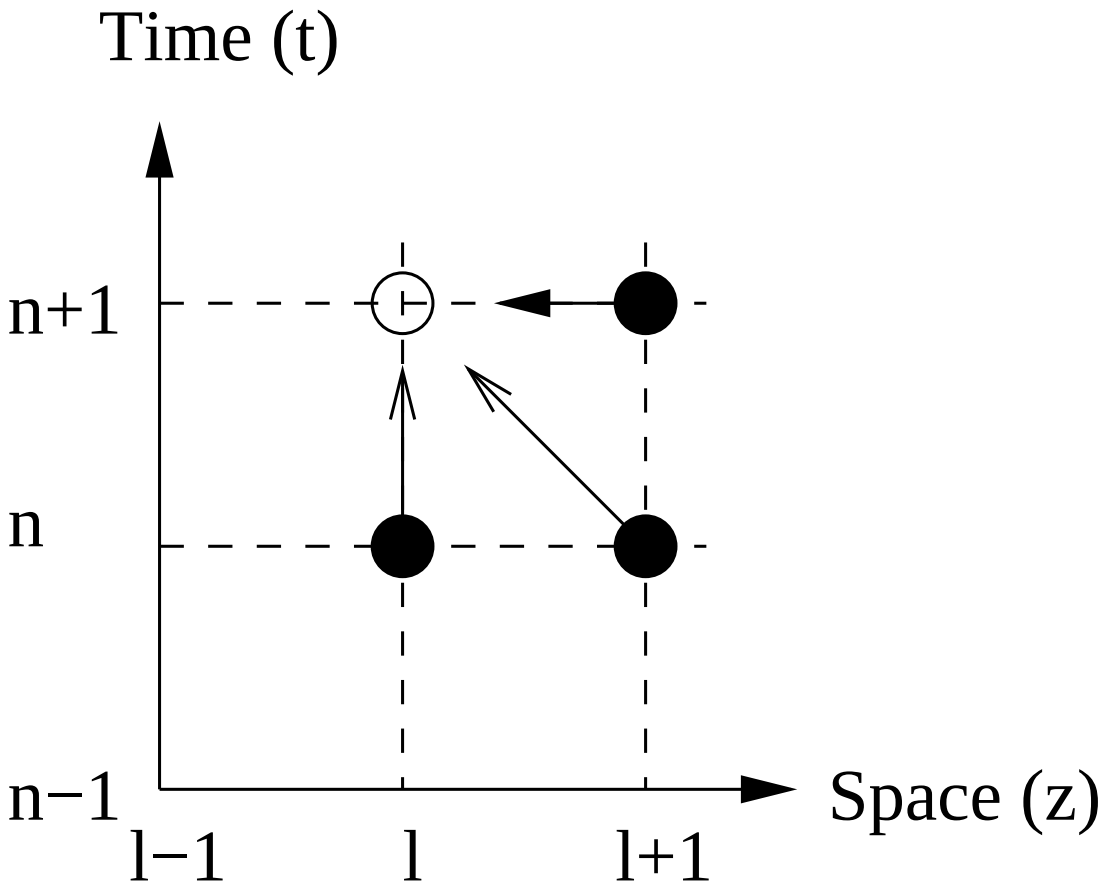

Figure 3.2: Implicit integration scheme showing which points in space and time are used to solve for the point to be updated. Here the iteration runs from forward to back and requires initializing the furthest upstream point in order to solve for all others (set to zero if sufficiently upstream).

Eq. (3.60) can be integrated by a similar method, this time depending on the sign of the term $(1/\gamma^2 - 2x/R)$. If it is positive, radiation can indeed propagate ahead of the beam and vice versa if it is negative, so we use two methods:

$$\boldsymbol{E}^{n+1}_{\perp,l+1} = \frac{1-p}{1+p}\left(\boldsymbol{E}^{n}_{\perp,l+1} - \boldsymbol{E}^{n+1}_{\perp,l}\right) + \boldsymbol{E}^{n}_{\perp,l} \ (p > 0), \tag{3.62a}$$

$$\boldsymbol{E}^{n+1}_{\perp,l-1} = \frac{1+p}{1-p}\left(\boldsymbol{E}^{n}_{\perp,l-1} - \boldsymbol{E}^{n+1}_{\perp,l}\right) + \boldsymbol{E}^{n}_{\perp,l} \ (p < 0), \tag{3.62b}$$

where $p = (1/2\gamma^2 - x/R)\Delta\tau/\Delta z$.

We can estimate the error in either step by Fourier analysis (neglecting the source term), assuming $\tilde{\boldsymbol{E}}_\perp \sim e^{ik_z z}$. Eqs. (3.59) and (3.60) separately can be integrated analytically, namely

$$\tilde{\boldsymbol{E}}_\perp(\boldsymbol{k}_\perp, k_z, t) = \tilde{\boldsymbol{E}}_\perp(\boldsymbol{k}_\perp, k_z, 0)\exp\left[-i\frac{k_\perp^2}{2k_z}\tau\right], \tag{3.63}$$

$$\boldsymbol{E}_\perp(\boldsymbol{x}_\perp, k_z, t) = \boldsymbol{E}_\perp(\boldsymbol{x}_\perp, k_z, 0)\exp\left[-ik_z\left(\frac{1}{2\gamma^2} - \frac{x}{R}\right)\tau\right]. \tag{3.64}$$

If we write the time stepping discrete forms as $\tilde{\boldsymbol{E}}^n_{\perp,l} = \lambda^n e^{il(k_z\Delta z)}$, $\boldsymbol{E}^n_{\perp,l} = \mu^n e^{il(k_z\Delta z)}$, and substitute them into Eqs.(3.61) and(3.62), we obtain

$$\lambda = \frac{1 - iq\cot(k_z\Delta z/2)}{1 + iq\cot(k_z\Delta z/2)}, \tag{3.65}$$

$$\mu = \frac{1 - ip\tan(k_z\Delta z/2)}{1 + ip\tan(k_z\Delta z/2)}. \tag{3.66}$$

It is obvious that $|\lambda|, |\mu| = 1$ for all wavelengths and step sizes and therefore both steps are individually unconditionally stable.

In order evaluate the combination of steps, we use Parseval's theorem

$$\int |\tilde{E}^n_{\perp,l}|^2 d\boldsymbol{k}_\perp = \int |E^n_{\perp,l}|^2 d\boldsymbol{x}_\perp \tag{3.67}$$

to write the overall scheme in terms of the square-integral of fields as a product. In our notation, the difference between n and $n+2$ will equal one complete step as $\tilde{\boldsymbol{E}}_{\perp,l}^{n+1} = \lambda \tilde{\boldsymbol{E}}_{\perp,l}^{n}$, and $\boldsymbol{E}_{\perp,l}^{n+2} = \mu \boldsymbol{E}_{\perp,l}^{n+1}$, therefore

$$\int |\tilde{E}_{\perp,l}^{n+2}|^2 d\boldsymbol{k}_\perp = |\lambda|^2 |\mu|^2 \int |\tilde{E}_{\perp,l}^{n}|^2 d\boldsymbol{k}_\perp, \tag{3.68}$$

$$\int |E_{\perp,l}^{n+2}|^2 d\boldsymbol{x}_\perp = |\lambda|^2 |\mu|^2 \int |E_{\perp,l}^{n}|^2 d\boldsymbol{x}_\perp. \tag{3.69}$$

Again, $|\lambda|^2|\mu|^2 = 1$ for all longitudinal modes, regardless of step size. Since each step conserves the square integral of the fields, it is clear that it remains bounded for all time. By definition, any unstable discrete mode would grow without bound and thereby cause the square integral to grow without bound which cannot happen, therefore we conclude that all modes are stable unconditionally. The preservation of the field energy is of course consistent with our model of perfectly conducting walls which have lossless reflection. Phase accuracy, on the other hand, can only be achieved if both $4q/k_z\Delta z,\ pk_z\Delta z \ll 1$. The worst case scenario occurs for a maximum longitudinal wavelength of L and transverse charge distribution width of $\sigma_\perp$ ultimately limits that maximum time step to

$$\Delta\tau \ll \frac{\sigma_\perp^2}{L}. \tag{3.70}$$

If we look at solutions $\sim e^{i(k_z z - \omega\tau)}$ in Eqs. (3.59, 3.60) we can obtain a separate dispersion relation for each step

$$\omega^{(1)} = \frac{k_\perp^2}{2k_z}, \tag{3.71}$$

$$\omega^{(2)} = \left(\frac{1}{2\gamma^2} - \frac{x}{R}\right) k_z. \tag{3.72}$$

The phase and group velocities, $v_\phi \equiv \omega/k_z$, $v_g \equiv \partial\omega/\partial k_z$ are

$$v_\phi^{(1)} = \frac{k_\perp^2}{2k_z^2}, \tag{3.73}$$

$$v_\phi^{(2)} = \left(\frac{1}{2\gamma^2} - \frac{x}{R}\right), \tag{3.74}$$

$$v_g^{(1)} = -\frac{k_\perp^2}{2k_z^2}, \tag{3.75}$$

$$v_g^{(2)} = \left(\frac{1}{2\gamma^2} - \frac{x}{R}\right). \tag{3.76}$$

By considering the action the combination of steps we can understand the scaling $k_{min} \gtrsim R^{1/2}a^{-3/2}$ of the synchronous modes. The requirement is that the phase velocity is zero. We can approximate this by requiring that $v_\phi^{(1)} + v_\phi^{(2)} = 0$. Transverse modes will have $k_\perp \gtrsim a^{-1}$, and $x \lesssim a$, thus requiring $k_z \gtrsim R^{1/2}a^{-3/2}$, ignoring the small terms $O(\gamma^{-2})$.

We can also see that the group velocity in Eq. (3.59) is always negative, and the group velocity in Eq. (3.60) may be positive or negative depending on the sign of the term $(1/2\gamma^2 - x/R)$. Therefore our choice of finite differencing in Eqs. (3.61, 3.62) for Eqs. (3.59, 3.60) automatically enforces causality as appropriate. We can also see that modes with large transverse wave numbers and small longitudinal wave numbers will rapidly fall behind the bunch because they have the greatest negative group velocity. Because the system is lossless, these modes could contaminate the solution if we had used periodic boundary conditions to model a non-periodic system. The mode with the largest (negative) group velocity has $k_\perp \sim \sigma_\perp^{-1}$ and $L \sim c$, the length of the computational domain. We can estimate the maximum bend angle

that can be simulated $\Delta\tau/R$ before this mode reaches the boundary,

$$\Delta\tau/R = \frac{c}{v_g R} \sim \frac{2\sigma_\perp^2}{cR}. \tag{3.77}$$

If we had used periodic boundary conditions, this would have restricted the simulation to cases where $\Delta\tau/R \ll 1$ which would be unacceptable for the range of parameters we are interested in.

As an illustration of the wrap-around effect we will compare the results from the time-domain method with the frequency-domain method for a sample simulation. Our frequency-domain method also uses a split-step method, but in this case we can solve each step exactly. The two integrations are

$$\begin{aligned}
\tilde{\boldsymbol{E}}_\perp(k_z, \tau + \Delta\tau) &= \tilde{\boldsymbol{E}}_\perp(k_z, \tau) \mathrm{e}^{-ik_\perp^2 \Delta\tau/2k_z} \\
&- \frac{2\pi i \boldsymbol{k}_\perp}{k_z} \mathrm{e}^{-ik_\perp^2 \Delta\tau/2k_z} \int_{\tau'}^{\tau'+\Delta\tau} \tilde{\rho}(k_z, \tau') \mathrm{e}^{ik_\perp^2 \tau'/2k_z} d\tau', \qquad (3.78) \\
\boldsymbol{E}_\perp(k_z, \tau + \Delta\tau) &= \boldsymbol{E}_\perp(k_z, \tau) \mathrm{e}^{i(1/2\gamma^2 - x/R)k_z \Delta\tau}. \qquad (3.79)
\end{aligned}$$

On the right hand side of Eq. (3.78), we will use a constant value for the source term. The longitudinal electric field can be easily computed

$$\tilde{E}_z(k_z, \tau) = \frac{i}{2k_z} \left[k_x \tilde{E}_x(k_z, \tau) + k_y \tilde{E}_y(k_z, \tau) + 4\pi \tilde{\rho}(k_z, \tau) \right]. \tag{3.80}$$

We integrated both methods over a short distance in a bend, with the transverse fields intialized to their steady-state values for a straight section, with the results shown in Fig. 3.3. In this images we see the magnitude and sign of E_z/e^2 in units of cm^{-2}, denoted by colors, yellow for positive and blue for negative. The fields are taken at the midplane ($y = 0$), as a function of x (horizontal, outside wall to the right) and z (vertical, head of bunch to bottom of page). On the left side is the

time-domain method and on the right, the frequency-domain method. There are two time steps, one after $s = 1$cm (top row), and another after $s = 5$ cm (bottom row) along the reference trajectory. Here one can clearly see the radiation leaving behind the tail of the bunch reappear ahead in the frequency-domain method because of the periodic boundary conditions. This is what is meant by the wrap-around effect. In the time-domain method, because we are free to use any boundary conditions we like, we can make the rear edge of the computational domain perfectly absorbing, in which case, all radiation reaching the boudary is lost. For a single bunch, the wrap-around effect violates causality. For this reason, we did not use the frequency domain approach.

3.5 Results

We now test the simulation results to theory where possible. All examples in this section, unless specified otherwise, will use a 100 MeV, 1 nC bunch, with a three-dimensional Gaussian distribution, with longitudinal rms length, $\sigma_z = 0.23$ cm, and axisymmetric transverse rms width, $\sigma_\perp = 0.2$ cm.,

$$\rho(\boldsymbol{x}) = \frac{Ne}{(2\pi)^{3/2}\sigma_\perp^2\sigma_z} e^{-(x^2+y^2)/2\sigma_\perp^2} e^{-z^2/2\sigma_z^2}. \tag{3.81}$$

Note that this form remains fixed which is definitely not the correct dynamical description of the bunch dynamics in a dipole magnet. However, because the theoretical results we will use for comparison assume a rigid bunch, we must also do so here. The bending radius where applicable is constant at $R = 120$ cm. The waveguide dimensions will vary as necessary for comparison to theory. For vacuum

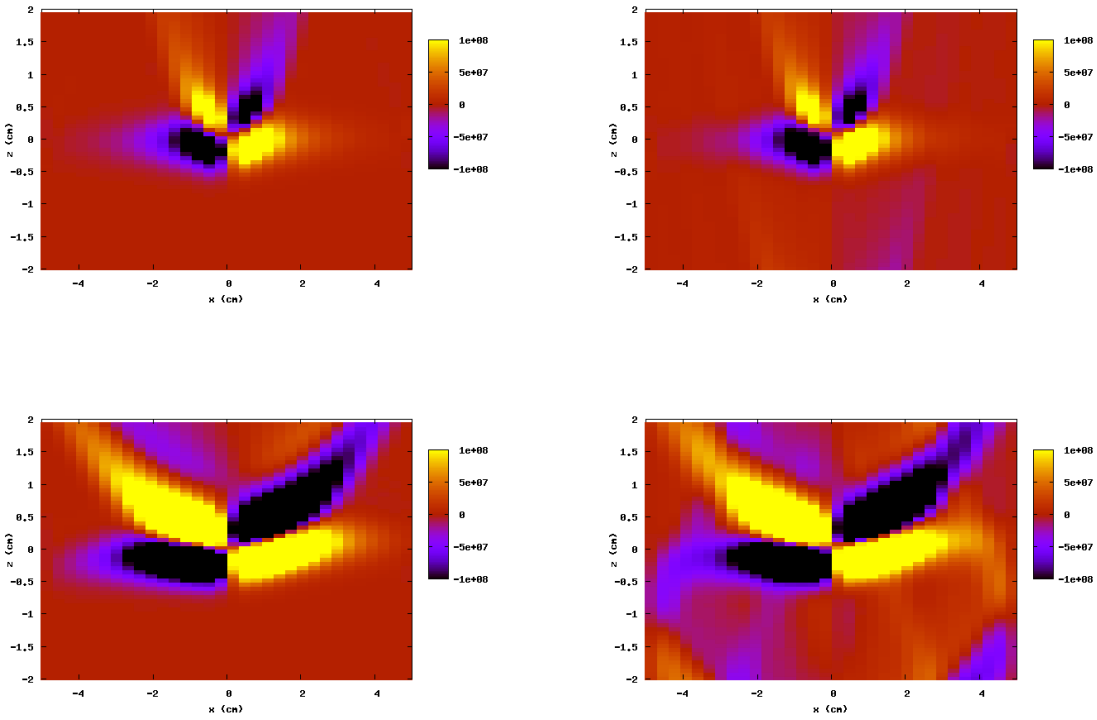

Figure 3.3: Comparison of time-domain (left) and frequency-domain (right) methods. The colors represent that strength of the longitudinal electric field taken at the midplane ($y = 0$). The horizontal axis is x, with the inside of the bend to the left and the vertical axis z with the head of the bunch towards the bottom. The top images are after 1 cm and the bottom after 5 cm. In the frequency-domain method, energy falling behind the computational window has reappeared ahead of the bunch, violating causality.

theory we will simply make them large enough that the results converge and shielding and reflection are negligible. For a fixed grid resolution, this means we need more grid points in the transverse directions to simulation vacuum. For the case of waveguide boundaries our method becomes more efficient because less grid points are required. On the other hand, theories which use image charges to account for shielding become less efficient as the waveguide dimensions shrink.

We begin with space-charge. Since we have retained terms to order γ^{-2}, we should be able to recover the space-charge fields for straight line motion. To see why this should work, examine Eq. (3.5) with $R \to \infty$. Because we no longer have the curvature term involving x, we may find the steady-state solution by setting the time derivative to zero and Fourier transforming all the space variables

$$\boldsymbol{E}(\boldsymbol{x}) = \int d^3x \hat{\boldsymbol{E}}(\boldsymbol{k}) e^{i\boldsymbol{k}\cdot\boldsymbol{x}} \tag{3.82}$$

Then we have the steady-state straight line solution

$$\hat{\boldsymbol{E}}_\perp^{ss}(\boldsymbol{k}) = \frac{4\pi \nabla \hat{\rho}(\boldsymbol{k})}{k_\perp^2 + k_z^2/\gamma^2}. \tag{3.83}$$

First, we compute the longitudinal force using the differential form of Eq.(3.8)

$$\hat{F}_z^{ss}(\boldsymbol{k}) = \frac{-i4\pi k_z \hat{\rho}}{\gamma^2(k_\perp^2 + k_z^2/\gamma^2)}. \tag{3.84}$$

Finally we substitute this into Eq.(3.10) to obtain

$$\hat{\boldsymbol{F}}_\perp^{ss}(\boldsymbol{k}) = \frac{4\pi \nabla \hat{\rho}(\boldsymbol{k})}{\gamma^2(k_\perp^2 + k_z^2/\gamma^2)}. \tag{3.85}$$

The inverse Fourier transform in independent of γ, so we can explicitly demonstrate the γ^{-2} scaling as expected. Thus, we can expect that if the simulation converges to a steady-state solution it should accurately calculate the space-charge forces.

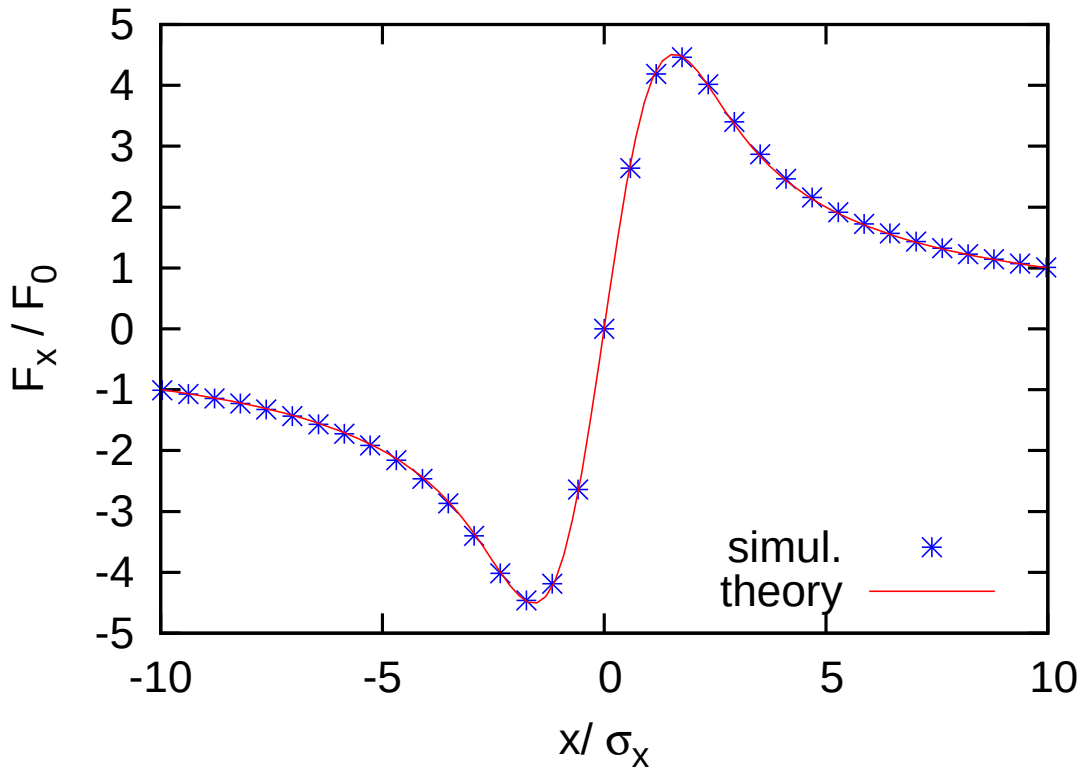

Figure 3.4: Space charge force x-component as a function of x in a straight 30 x 30 cm waveguide, taken at center point of a three-dimensional Gaussian bunch with rms length $\sigma_z = 0.23$ cm, and rms width $\sigma_\perp = 0.2$ cm. Simulation results are circles, and theory is represented by a solid line. The force is normalized to $F_0 = Ne^2/\sqrt{2\pi}\sigma_z\gamma^2$.

As a test, we numerically integrate Eqs. (3.59, 3.60) with $R \to \infty$ and compute the space-charge fields which are known from theory in vacuum. The theoretical space-charge force for a three-dimensional Gaussian in free-space is given by

$$F_x = \frac{2Ne^2}{\sqrt{2\pi}\sigma_z\gamma^2}\left(\frac{1-e^{-x^2/2\sigma_x^2}}{x}\right). \tag{3.86}$$

The results are shown in Fig. 3.4 showing excellent agreement.

We then calculate the coherent synchrotron radiation and space-charge longitudinal force in a curved waveguide at various times along the trajectory for a rigid

charge distribution. For comparison, we take the transient theory for a Gaussian line charge [48]

$$F_z = \sqrt{\frac{2}{\pi}} \frac{Ne^2}{(3R^2\sigma_z^4)^{1/3}} G(\zeta, \eta), \tag{3.87}$$

where $G(\zeta, \eta)$ is a function on the order of 1 given by

$$G(\zeta, \eta) = \eta^{-1/3} \left[e^{-(\zeta-\eta)^2/2} - e^{-(\zeta-4\eta)^2/2} \right] + \int_{\zeta-\eta}^{\zeta} \frac{d\zeta'}{(\zeta-\zeta')^{1/3}} \frac{d}{d\zeta'} e^{-(\zeta')^2/2}, \tag{3.88}$$

where $\zeta = z/\sigma_z$ is the distance traveled in the bend and $\eta = \xi^3/(24R^2\sigma_z)$. The results are shown in Fig. 3.6, which also show very good agreement.

Using the same methodology we may also investigate the effect of the two transverse beam widths on the longitudinal force. This is particularly applicable to a bunch compressor chicane in which the beam expands and contracts in the horizontal plane (the x-direction) because of dispersion. In a one-dimensional model, the transverse extent of the beam is ignored, so we may inquire as to what the effect of that assumption is on the accuracy. Looking at the form of Eq. (3.26), and assuming the angle $\xi/R \ll 1$ we can expand the cosine function so that

$$D_{ret} \approx \xi + \frac{(x-x')^2 + (y-y')^2}{2\xi} + \frac{(x+x')\xi}{2R} - \frac{\xi^3}{24R^2}. \tag{3.89}$$

Because of cancellation in the numerator of the lead term, the retarded charge density goes like $\rho(z' - \xi^3/24R^2)$ to leading order. So we again see the scaling in the formation length, that is the bulk of the interaction occurs over a range when $\xi^3/24R^2 \sim \sigma_z$ or $\xi \sim 2(3\sigma_z R^2)^{1/3}$. In the denominator, we should not see any difference unless $x' \sim s_f$ where $s_f = 2(3\sigma_z R^2)^{1/3}$ is the characteristic formation length. We show the steady-state longitudinal field for various values of x/s_f, comparing

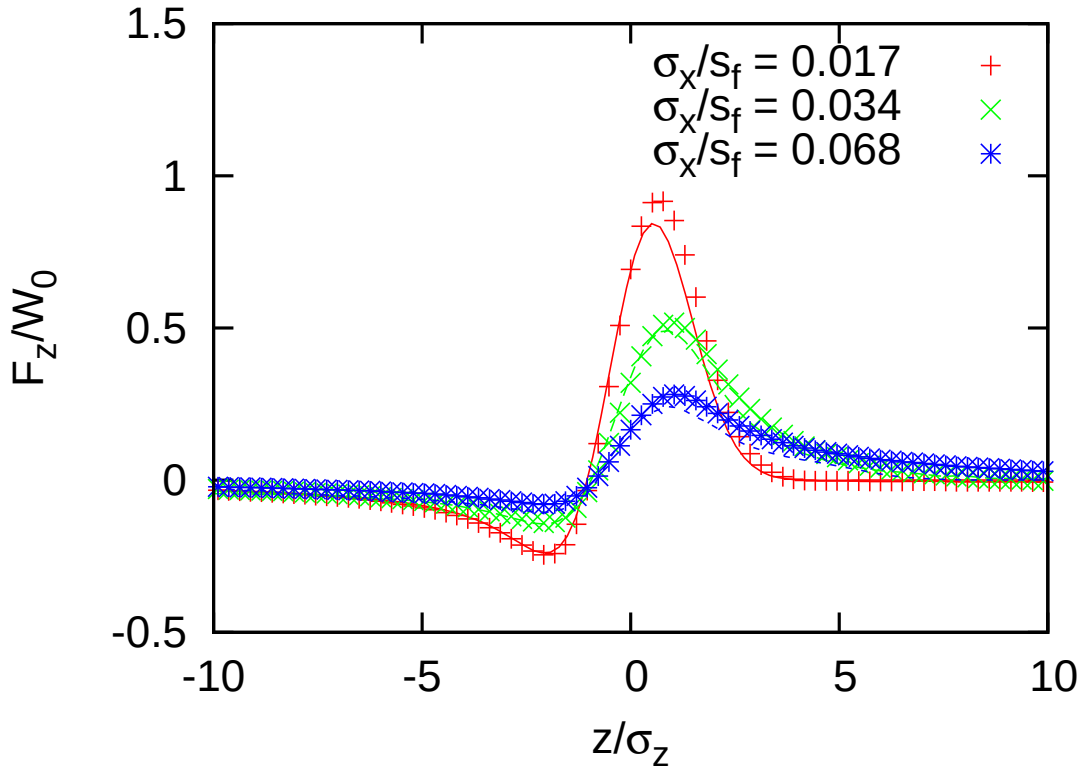

Figure 3.5: . Steady-state longitudinal force from rigid charge distribution of varying widths in x-direction. The beam is a three-dimensional Gaussian with the z and y rms beam widths held constant. The symbols are the result of simulation and the lines are the result of numberical integration of Eqs (3.24,3.25). The longitudinal coordinate z is scaled to the rms bunch length σ_z, which is 60 μm, and the force is scaled to $W_0 = \sqrt{2/\pi}Ne^2(3R^2\sigma_z^4)^{-1/3}$. The rms beam widths are scaled to the formation length $s_f = 2(3\sigma_z R^2)^{1/3}$. As discussed in the text, a more appropriate scaling is x/x_0 where $x_0 = (3\sigma_z^4 R^2)^{1/6}$ which for these three cases have values 0.5, 1.5 and 3.0.

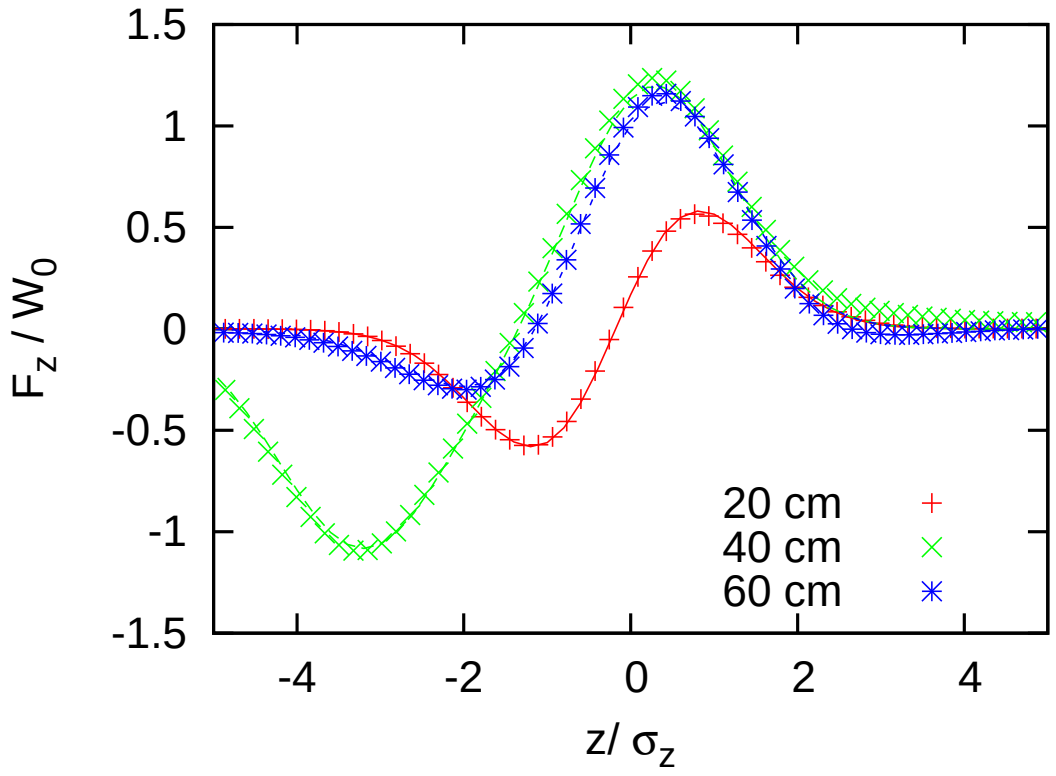

Figure 3.6: Longitudinal force as a function of z (taken at $x, y = 0$) from CSR in transient states (measured in distance traveled past entrance) from simulation (symbols) compared to vacuum theory (lines) for three-dimensional Gaussian bunch in a 30 x 30 cm rectangular waveguide with uniform bending radius of 120 cm. The longitudinal coordinate z is scaled to the rms bunch length σ_z, which is 0.23 cm, and the force is scaled to $W_0 = \sqrt{2/\pi} N e^2 (3R^2\sigma_z^4)^{-1/3}$

both the simulation and numerical integration methods in Fig. 3.5. Note that there is a significant change even for small values of x/s_f. In the numerator of the integrand in Eqs. (3.24,3.25), because of the cancellation of the leading term, we may see a significant difference in the argument whenever $x/x_0 \gtrsim 1$ where $x_0 = 3^{1/6}\sigma_z^{2/3}R^{1/3}$. In Fig. 3.5, x_0= 0.2 cm, and the three plots correspond to x/x_0= 0.5, 1.5 and 3.0 respectively, demonstrating that this is the appropriate scaling for beam width.

We now compare our simulation with the steady-state theoretical results for shielding. By reducing the vertical gap size, keeping the horizontal dimension large, we should approximate the case of infinite parallel plates. Although there are results for parallel plate shielding for a Gaussian line charge given directly in the time domain, it is somewhat easier to calculate the results using the longitudinal coupling impedance [16]. A line charge can be approximated in our simulation by reducing the transverse dimensions so that $\sigma_\perp \ll \sigma_z$. An actual line charge is impossible on this simulation because it would require an infinite number of terms in the eigenfunction expansion, also reducing the maximum time step given Eq. (3.70) to an infinitesimal distance. So we just fix the transverse dimension of the waveguide at a large width, here 50 cm, and reduce $\sigma_\perp$ until the results converge. The results are shown for three different values of gap size, each obtained after the fields have reached steady state, achieved after a distance in the bend that is much longer than the characteristic formation length $\tau \gg 2(3\sigma_z R^2)^{1/3}$, which in this case is about 42 cm. The results from the simulation were taken at $\tau = 300$ cm, and as shown in Fig. 3.7, once again demonstrate excellent agreement with the theory.

If we now reduce the width of the waveguide we may expect to see the effects of shielding in both transverse directions. For a sustained interaction with the radiation, it must propagate with a similar speed (i.e. phase velocity) as the bunch. The synchronous modes of a square toroidal waveguide must have wavenumbers above $k_{min} = 4.78R^{1/2}a^{-3/2}$ [16, 17, 22]. Furthermore, for these modes to be coherent with the bunch they must satisfy $k\sigma_z \lesssim 1$. In general, if $k_{min}\sigma_z \ll 1$, there will be many synchronous modes, approaching the limiting case where the synchronous modes

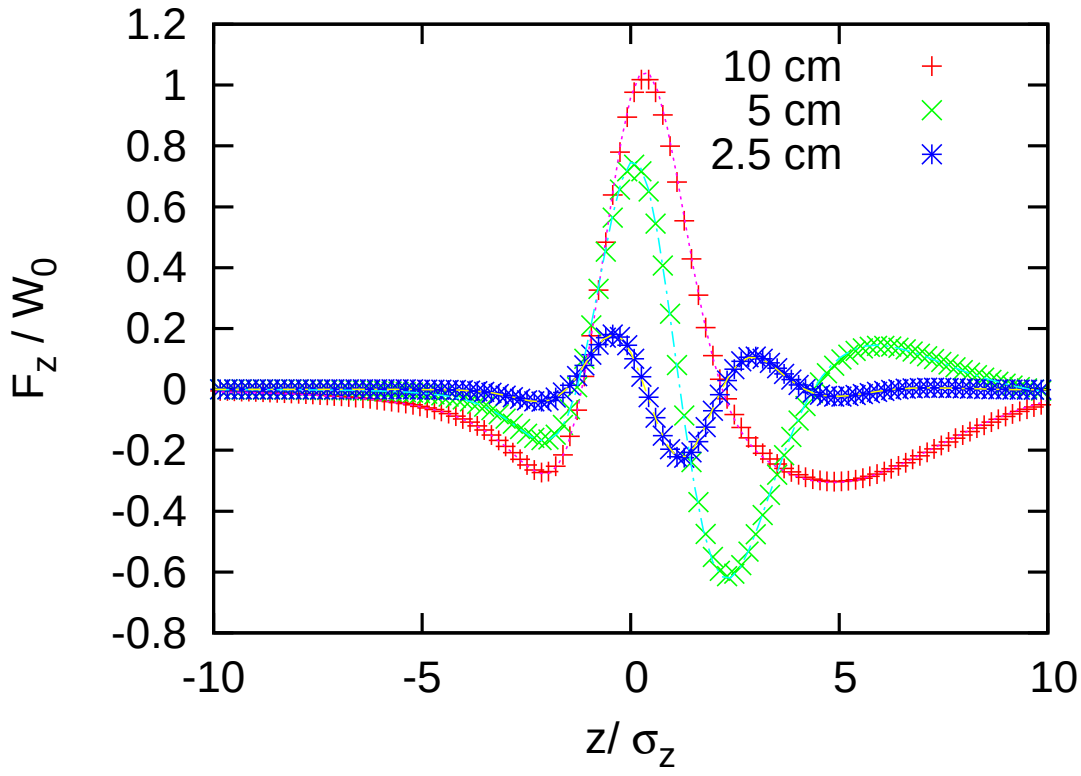

Figure 3.7: Longitudinal force as a function of z (taken at $x, y = 0$) from CSR in steady state with shielding from infinite parallel plates for three different gap sizes. The simulation (symbols) is compared to infinite parallel plate theory (lines) for Gaussian line charge. The bending radius is 120 cm, and the horizontal gap in the simulation is fixed at 50 cm to approximate infinite parallel plates. The longitudinal coordinate z is scaled to the rms bunch length σ_z, which is 0.23 cm, and the force is scaled to $W_0 = \sqrt{2/\pi} N e^2 (3R^2\sigma_z^4)^{-1/3}$

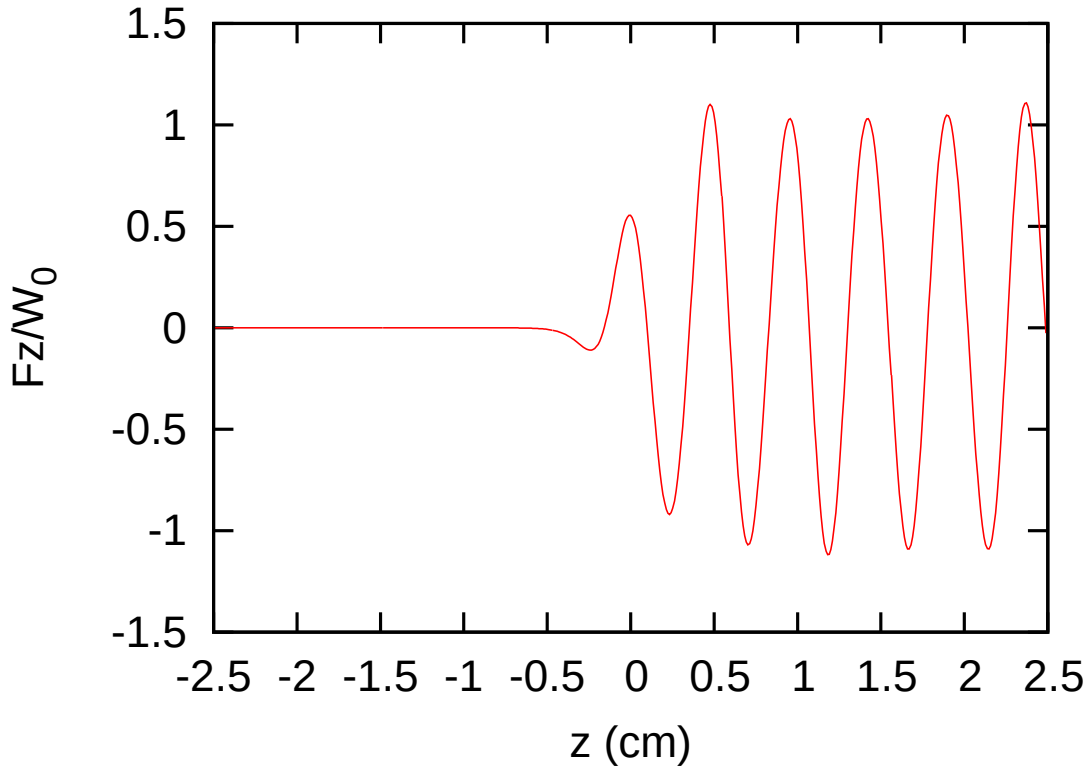

Figure 3.8: Longitudinal force as a function of z (taken at $x, y = 0$) from CSR in steady state in a square toroidal waveguide. The sinusoidal wake behind the bunch is the lowest order synchronous mode TE(1,0), and has wavenumber $k = 13.2$ cm. The bending radius is 120 cm, and the width and height are 2.5 cm. The longitudinal coordinate z is scaled to the rms bunch length σ_z, which is 0.115 cm, and the force is scaled to $W_0 = \sqrt{2/\pi} N e^2 (3R^2\sigma_z^4)^{-1/3}$.

appear as a continuum. As a becomes very large, we approximate the vacuum (unshielded case). On the other hand, as a is made smaller, causing k_{min} to be greater, we approach the case where fewer modes will be coherent. Therefore, by carefully choosing the bunch length and a, we may be able to isolate just a single mode which is both synchronous and coherent, thereby seeing it's effect clearly, appearing as a single sinusoidal signal behind the bunch. Recall that we are simulating a single bunch, and therefore no mode can be stimulated in front of it.

Using the nomenclature of [16], there are two types of modes, the "TE" mode with $E_y = 0$, and the "TM" mode with $E_x = 0$. For the square waveguide, the lowest frequency modes calculated by the method in Table 2.1 are: TE(1,0) at $k = 4.78R^{1/2}a^{-3/2}$, TM(1,0) at $k = 8.78R^{1/2}a^{-3/2}$, and TE(1,1) at $k = 12.8R^{1/2}a^{-3/2}$. For all cases using the simulation, we choose $a = b = 2.5$ cm. In order to only see the lowest mode, we pick $\sigma_z = 0.115$ cm. The resulting steady-state longitudinal force along the axis at $x = y = 0$ is shown in Fig. 3.8, which clearly illustrates the presence of a single sinusoidal synchronous mode stimulated behind the bunch. We can also compute the power loss of the bunch, using the results from [22], where the loss factor for a single electron with energy W is $\kappa \equiv e^{-2}dW/ds$. To calculate the average bunch power loss we must take into account the effects of coherence as discussed in the introduction. For the Gaussian bunch distribution, the average energy loss rate of the bunch for a single mode is

$$\frac{d\bar{W}}{ds} = \kappa r_e mc^2 N e^{-(k\sigma_z)^2}, \tag{3.90}$$

where $r_e = e^2/mc^2$ is the classical electron radius. Using the value from [22], with

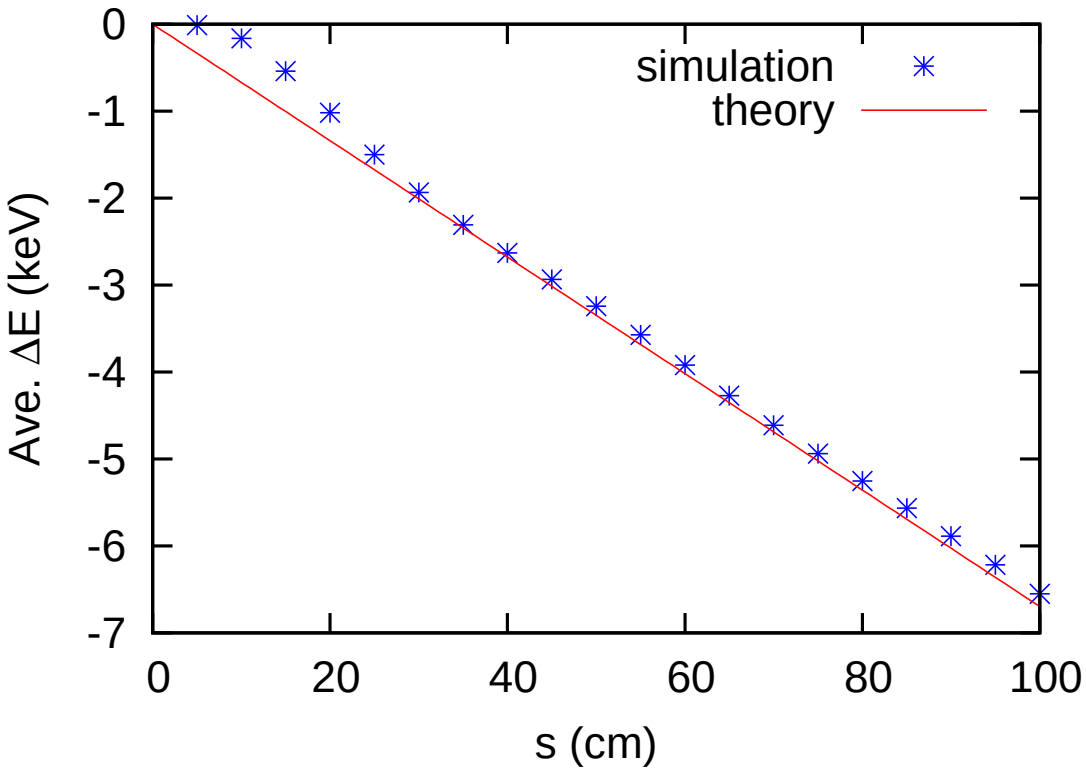

Figure 3.9: Average power loss from the TE(1,0) synchronous mode in a square toroidal waveguide as a function of distance s along the bend. The bending radius is 120 cm, and the width and height are 2.5 cm. The bunch length $\sigma_z = 0.115$ cm, and the rms beam width is $\sigma_\perp = 0.07$ cm. The symbols are the average beam energy deviation (from 100 MeV initial energy) expressed in keV, and the line is theoretical prediction of 67 eV/cm. The simulation results reaches a steady-state loss rate of 66 eV/cm, which differs from the theoretical prediction by 1.5 %

$\kappa a^2 = 4.94$ for the TE(1,0) mode, leads to a predicted average energy loss rate of 67 eV/cm when $\sigma_z = 0.115$ cm.

We can test this using the simulation with some test particles which do not move but keep track of the total energy change. Once again, the source remains fixed, as that is the assumption of the theory. After the initial transient phase in which the non-synchronous modes fall behind, we find a steady-state energy loss rate of 66 eV/cm, which differs from the theory by 1.5%. A plot of the energy deviation from the initial average beam energy of 100 MeV vs. distance s along the bend is shown in Fig. 3.9. The initial difference occurs while the radiation fields are forming up into a trailing wake. The small residual discrepancy is attributed to differences in the assumptions of the theory and the realities of the simulation. Noteably, we cannot use a line charge, but only approximate it by reducing the beam width. In the simulation the beam was a Gaussian axisymmetric distribution with $\sigma_\perp = 0.07$ cm. Additionally, the theory uses a periodic boundary at $2\pi R$, so in principle, there would be a sinusoidal wake in front of the bunch also. The simulation, however uses special boundary conditions where this wake will never appear in front of the bunch because all of the synchronous modes have negative group velocities. Regardless, we find a reasonable agreement between the theory and simulation in this case, as we expect the effects to be small.

We can uncover more modes by decreasing the bunch length. We now take $\sigma_z = 0.028$ cm and again run the simulation to a steady-state situation. In this case, we should see the three lowest frequency modes as described above. To confirm the presence of these modes, we can identify them more clearly in a spectral analysis

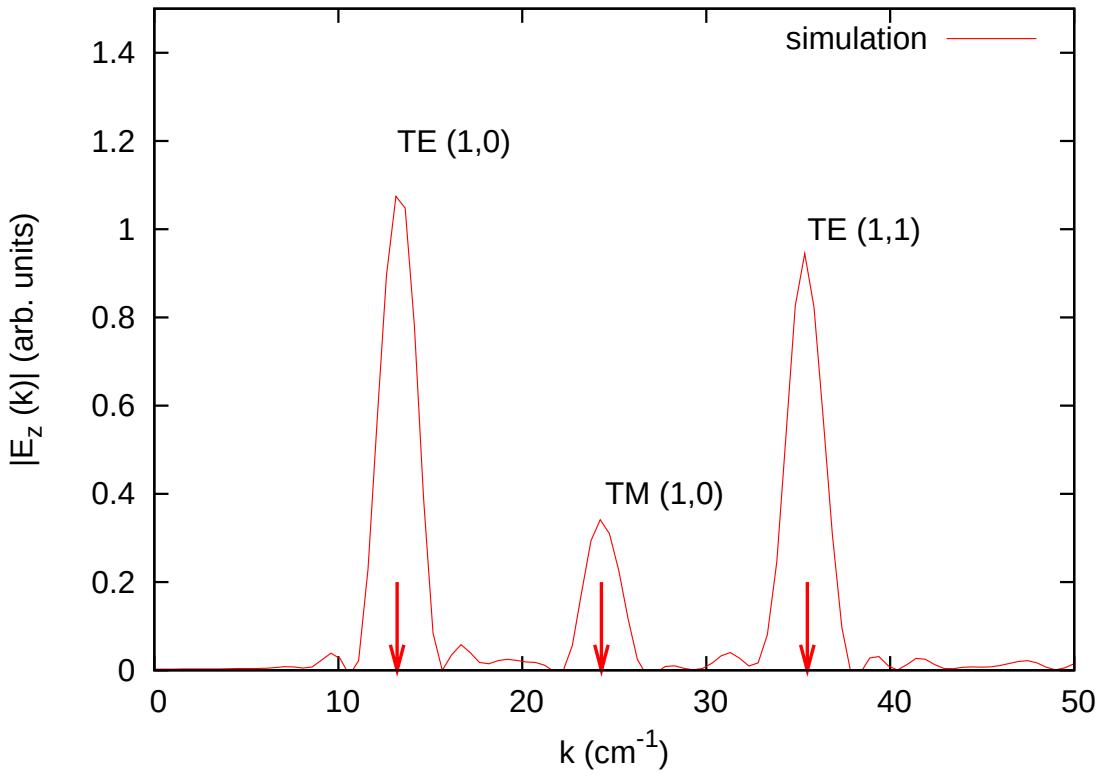

Figure 3.10: Power spectrum of E_z (taken at $x, y = 0$) from CSR in steady state in a square toroidal waveguide, showing the three lowest frequency synchronous modes. The bending radius is 120 cm, and the width and height are 2.5 cm. The three modes have predicted wavenumbers of 13.2, 24.3 and 35.5 cm^{-1} respectively. The beam is a fixed three-dimensional Gaussian with $\sigma_z = 0.028$ cm, and $\sigma_\perp = 0.07$ cm.

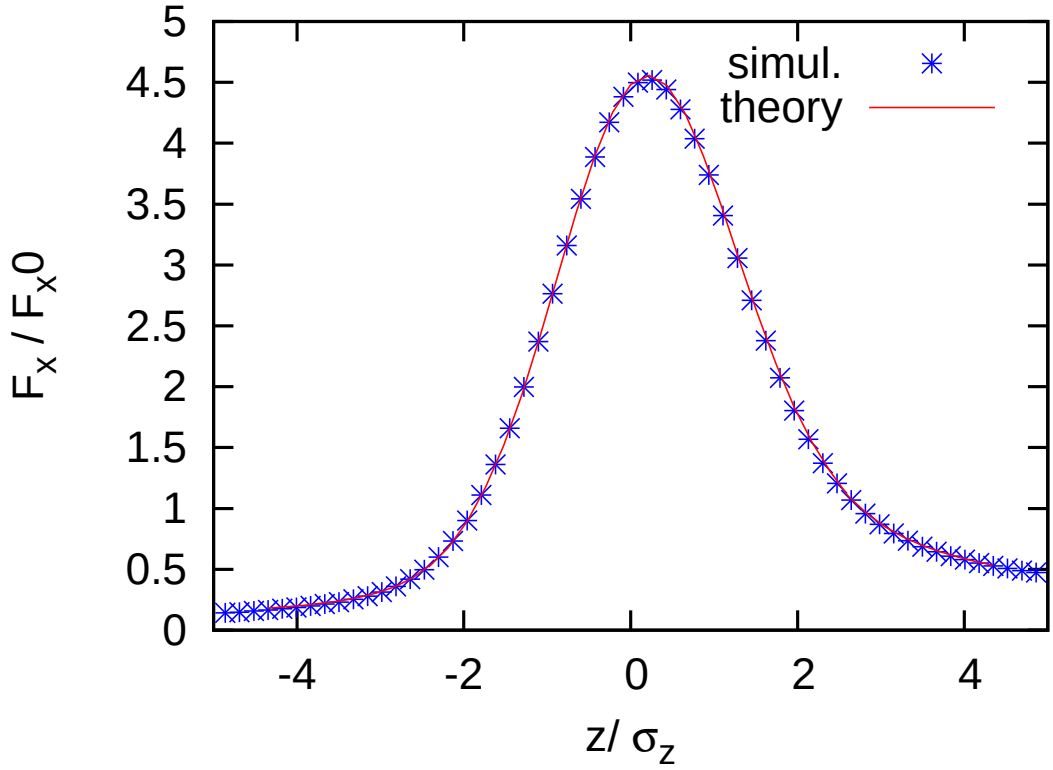

Figure 3.11: Transverse coherent synchrotron radiation force in steady state as a function of z, taken along the center $x, y = 0$ of a three-dimensional Gaussian bunch given by simulation (shown in circles). The theoretical value (line) was calculated by numerical integration of Eqs.(3.24) and (3.25). The longitudinal coordinate z is scaled to the rms bunch length σ_z and the force is scaled by $F_{x0} = 2Ne^2/R$.

which is shown in Fig. 3.10. Here, we now see the TE(1,0), TM(1,0) and TE(1,1) modes. The modes above these frequencies do not appear with any significant power because there are not coherent at this bunch length.

Lastly, we compute the steady-state transverse coherent synchrotron force (including the space-charge force) (in the plane of motion) as shown in Fig. 3.11. For comparison, we numerically integrated Eqs. (3.24) and (3.25). The non-symmetric shape is an effect of the finite transverse dimensions of the bunch. It should be noted

that the theoretical result can only be obtained under artificial constraints, specifically here we must assume a linear velocity shear in order to make a rigid charge distribution fixed in the local coordinate system. Of course, this is unphysical because if the reference trajectory is close to the speed of light, the outer particles will exceed it. As we will see in Chapter 4, in an actual uniform bending section, the bunch would be continuously deforming in a combination of betatron motion in the horizontal plane coupled with longitudinal bunching/debunching all with period $2\pi R$. In this case the forces would never reach a steady-state and we would be left without anything to compare to. Despite these violations of our assumptions it is interesting to note that simulation implicitly took care of this while the theory had to be modified.

Chapter 4

Particle Dynamics

Having established how the fields and resulting forces are to be calculated, we now turn to the dynamical description of the beam. We will only use two basic elements for external fields: a drift space (no external fields) and a uniform magnetic dipole field. Using these elements we can build up composite systems such as 180^0 bends, storage rings and chicanes. In reality, these systems also contain quadrupoles in various combinations such as focusing-defocusing lattices (FODO channel) for control of the beam size or in doublet or triplet combinations for beam matching between elements. Although, these elements could be incorporated into the simulation we are describing, they are not. The reason is simply that within the elements where CSR effects are the greatest, such as inside a chicane, the elements are not necessary, particularly at high energies. So we will leave them out, at least for now.

The dynamics of the beam will actually be the nearly same in either a drift or dipole, with the only difference being the parameter describing the bending radius of the reference trajectory. In fact, the dirft section can be simply interpreted as the limit of infinite bending radius, in which case we only really need one element. Transitions between elements could be accomplished by changing the bending radius parameter, however there is an additional effect when the bunch enters the dipole

field at an angle not perpendicular to the pole edge faces. The effect will be handled in a simple manner which we will detail a little later in this chapter.

4.1 Equations of Motion in Magnetic Dipole Field

In a constant dipole magnetic field, the fundamental equations of motion in cylindrical coordinates (r, θ, y), where y is perpendicular to the bending plane, are

$$\gamma\ddot{r} = \gamma r\dot{\theta}^2 - \dot{\gamma}\dot{r} - \frac{F_r}{m} - \frac{e\beta B_0}{m} \tag{4.1}$$

$$\gamma r\ddot{\theta} = -\gamma\dot{r}\dot{\theta} - \dot{\gamma}r\dot{\theta} - \frac{eE_\theta}{m} \tag{4.2}$$

$$\gamma\ddot{y} = -\dot{\gamma}\dot{y} + \frac{F_y}{m} \tag{4.3}$$

$$\dot{\gamma} = -\frac{e\beta E_\theta}{mc}, \tag{4.4}$$

where B_0 is a uniform magnetic dipole field, and $(F_r, -eE_\theta, F_y)$ are the forces from the self-fields.

4.2 Reference Trajectory

In the absence of any self-fields, clearly $\dot{\gamma} = 0$, so we can define the reference trajectory for a given constant energy γ_0 by the condition $\dot{r} = 0$, $r = R$. According to Eqn. (4.2), $R\dot{\theta} = \textit{constant} = \beta c$. We can use Eqn. (4.1) to solve for the equilibrium radius

$$R = \frac{\beta\gamma_0 mc^2}{eB_0}, \tag{4.5}$$

where $\beta = \sqrt{1 - \gamma_0^{-2}}$.

4.3 Deviations from Reference Trajectory

We assume that the particle's energies are large compared to the rest energy, $E/mc^2 \gg 1$ so that $\gamma \gg 1$ and that $v_\theta \approx c$, $v_\theta \gg v_r, v_y$, so that we can consider all of the particle's velocity to be the θ-direction, then

$$\frac{d}{dt}\left(r\dot{\theta}\right) = -\frac{eE_\theta}{\gamma^3 m}, \tag{4.6}$$

which we will consider to be negligible for $\gamma \gg 1$. For each particle, therefore, $r\dot{\theta} = \beta c$ is a constant of motion. Expanding in deviations in radius $r = R + x$, where the reference frame moves with $\dot{\theta}_0 = \beta c/R$ and a general particle at $\dot{\theta} = \beta c/(x+R)$. This presumes they both are moving along an arc. In the more general case, we can simply compare the differential path length between an aribtrary path and the reference trajectory. If is more useful now to use the distance along the reference trajectory $s = \beta ct$ as the independent variable. Denoting the derivative with respect to s by the notation $x' = dx/ds$ so that the differential path lengths can be written

$$dl^2 = x'^2 + y'^2 + (1 + x/R)^2 \tag{4.7}$$

$$dl_{ref}^2 = 1. \tag{4.8}$$

The difference in path length, $z = l - l_{ref}$, relative to the reference as measured along the reference arc with radius R therefore evolves according to

$$\dot{z} = \sqrt{x'^2 + y'^2 + (1 + x/R)^2} - 1. \tag{4.9}$$

For deviations in energy $\gamma = \gamma_0 + \Delta\gamma$ we can define $\delta = \Delta\gamma/\gamma_0$ which evolves according to

$$\delta' = -\frac{eE_\theta}{\beta\gamma_0 mc^2}. \tag{4.10}$$

In the transverse coordinate $r = R + x$ we can use the approximate constant of motion $r\dot{\theta} = \beta c$ and write

$$x'' = \frac{\delta - x/R}{R(1 + x/R)(1 + \delta)} + \frac{F_x}{\gamma mc^2} \tag{4.11}$$

where we have neglected the $\dot{\gamma}/\gamma$ term.

4.4 Numerical Integration the Equations of Motion

In order to minimize the potential for error, we would like to integrate the dynamic coordinates using at least second-order techniques. For x, y, and δ this can be accomplished using leapfrog integration. Consider the equation for advancing x by one timestep using the value of x' on the half-step,

$$x_{num}(s + \Delta s) = x(s) + x'(s + \Delta s/2)\Delta s. \tag{4.12}$$

The Taylor expansion of x about s is

$$x(s + \Delta s) = x(s) + x'(s)\Delta s + \tfrac{1}{2}x''(s)\Delta s^2 + \tfrac{1}{6}x'''(s)\Delta s^3 + ... \tag{4.13}$$

Using the Taylor series $x'(s + \Delta s/2) \approx x'(s) + x''(s)\Delta s^2/2 + x'''(s)\Delta s^3/24$, we see the error is proportional to the third power of the time step

$$x_{num}(s + \Delta s) - x(s + \Delta s) = \tfrac{3}{24}x'''(s) + ... \tag{4.14}$$

we can apply the same method for y and δ

$$y_{num}(s + \Delta s) = y(s) + y'(s + \Delta s/2)\Delta s, \tag{4.15}$$

$$\delta_{num}(s + \Delta s) = \delta(s) + \frac{e}{\gamma mc^2}E_z(s + \Delta s/2)\Delta s. \tag{4.16}$$

So it would seem convenient to just compute the values of x, y and δ at increments of $n\Delta s$, $n = 1$, 2,3... and the value of x', y' and E_z at half-steps $(n + 1/2)\Delta s$. However, this will not work, because the integration of x' depends on F_x (recall that F_x is computed from E_z), so we need its value on the whole step. We can still preserve second-order accuracy by integrating in two steps.

$$x'_{num}(s + \Delta s/2) = x'(s) + x''(s)\frac{\Delta s}{2}, \tag{4.17}$$

$$x'_{num}(s + \Delta s) = x'_{num}(s + \Delta s/2) + x''(s + \Delta s)\frac{\Delta s}{2}. \tag{4.18}$$

Using the same analysis the error is again third-order

$$x'(s + \Delta s) - x'_{num}(s + \Delta s) = \tfrac{1}{12}x''''(s)\Delta s^3 + ... \tag{4.19}$$

The technique will be required to advance x', y', z and the fields themselves $\boldsymbol{E}_\perp$. The complete sequence to advance one complete time step is

1. $x'(s)$, $y'(s) \rightarrow x'(s + \Delta s/2)$, $y'(s + \Delta s/2)$.

2. $\boldsymbol{E}_\perp(s) \rightarrow \boldsymbol{E}_\perp(s + \Delta s/2)$.

3. $z(s) \rightarrow z(s + \Delta s)$.

4. $x(s)$, $y(s)$, $\delta(s) \rightarrow x'(s + \Delta s/2)$, $y'(s + \Delta s/2)$, $\delta(s + \Delta s)$.

5. $z(s + \Delta s/2) \rightarrow z(s + \Delta s)$.

6. $\boldsymbol{E}_\perp(s + \Delta s/2) \rightarrow \boldsymbol{E}_\perp(s + \Delta s)$.

7. $x'(s + \Delta s/2)$, $y'(s + \Delta s/2) \rightarrow x'(s + \Delta s)$, $y'(s + \Delta s)$.

Although steps 1 and 7 could be combined, the break is there so all variables can be written to output on the whole increment in time.

4.5 Linear Approximation and Matrix Methods

Expanding in the small terms $x/R, \delta \ll 1$ to first order,

$$x'' \approx -\frac{x}{R^2} + \frac{\delta}{R} + \frac{F_x}{\gamma_0 mc^2}, \tag{4.20}$$

where we have neglected any energy deviation effect in the term involving the self-fields since these will already be treated as a first-order perturbative effect. The first term represents the natural betatron focusing for a dipole magnet, and the second term represents the first and second-order dispersion effects.

Without self-fields, we can solve Eq. (4.20) for any trajectory analytically within the linear approximation. We begin with the homogenous equation

$$x'' + \frac{1}{R^2}x = 0, \tag{4.21}$$

which is satisfied by either $\cos(s/R)$ or $\sin(s/R)$. From the initial conditions $x(0) = x_0$ and $x'(0) = x'_0$, we can write the homogenous solution describing the natural betratron motion without dispersion

$$x^H(s) = x_0 \cos\left(\frac{s}{R}\right) + x'_0 R \sin\left(\frac{s}{R}\right), \tag{4.22}$$

$$x'^H(s) = -\frac{x_0}{R}\sin\left(\frac{s}{R}\right) + x'_0 \cos\left(\frac{s}{R}\right). \tag{4.23}$$

Likewise we can write the equation including dispersion and look for a particular solution. Starting with

$$x'' + \frac{1}{R^2}x = \frac{\delta}{R}, \tag{4.24}$$

we can see that the addition of δR to either cos or sin solution will work, but to meet the boundary conditions we require the combination $\delta R(\cos(s/R) - 1)$ making

the complete solution

$$x(s) = x_0 \cos(\frac{s}{R}) + x_0' R \sin\left(\frac{s}{R}\right) + \delta R \left(\cos(\frac{s}{R}) - 1\right), \tag{4.25}$$

$$x'(s) = -\frac{x_0}{R} \sin\left(\frac{s}{R}\right) + x_0' \cos\left(\frac{s}{R}\right) - \delta \sin\left(\frac{s}{R}\right). \tag{4.26}$$

We can also write this in a matrix form

$$\begin{pmatrix} x \\ x' \\ y \\ y' \\ z \\ \delta \end{pmatrix} = \begin{pmatrix} \cos\phi & R\sin\phi & 0 & 0 & 0 & R(\cos\phi - 1) \\ -\frac{1}{R}\sin\phi & \cos\phi & 0 & 0 & 0 & \sin\phi \\ 0 & 0 & 1 & R\phi & 0 & 0 \\ 0 & 0 & 0 & 1 & 0 & 0 \\ -\sin\phi & R\cos\phi & 0 & 0 & 1 & R\phi \\ 0 & 0 & 0 & 0 & 0 & 1 \end{pmatrix} \begin{pmatrix} x_0 \\ x_0' \\ y \\ y' \\ z_0 \\ \delta_0 \end{pmatrix} \tag{4.27}$$

where $\phi = s/R$. Note that the normal motion is a counter-clockwise rotation in the $x - z$ plane. The matrix method for linear transport is unfortunately too inaccurate for what we need, and will only be used for some analysis functions.

4.6 Edge Effects

If the beam enters or exits the magnetic dipole not perpendicular to the face, electrons that are displaced to either side will enter/exit at different times than the reference trajectory. Let η be the angle of the face relative to perpendicular, where $\eta > 0$ means that electrons displaced by $x > 0$ enter first. For small $\eta \ll 1$, the extra distance traveled is approximately $\Delta s = x \tan(\eta)$, which we also assume is small causing a deflection of $\Delta x' = -(x/R)\tan(\eta)$, while x is unchanged. This is the equivalent of a thin lens with focal length $f = R/\tan\eta$. The transport matrix

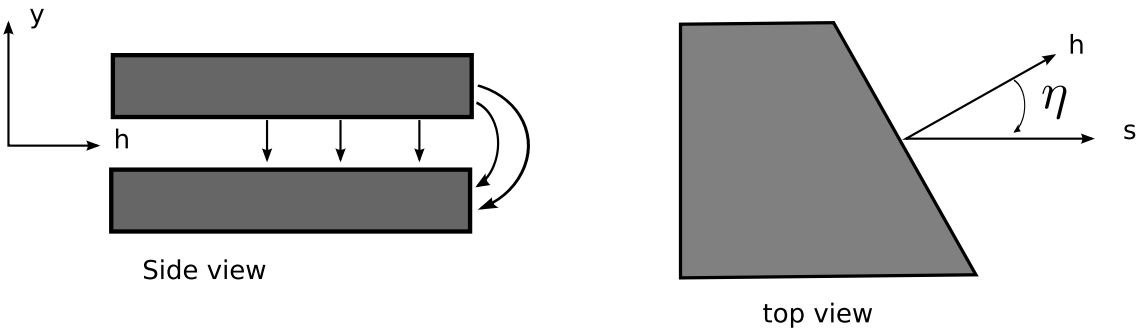

Figure 4.1: Geometry for fringe field calculation. The beam trajectory in the s-direction, exits at an angle η with respect to perpendular to the horizontal pole face, the h-direction.

is

$$\begin{pmatrix} x \\ x' \end{pmatrix} = \begin{pmatrix} 1 & 0 \\ -\frac{1}{R}\tan\eta & 1 \end{pmatrix} \begin{pmatrix} x_0 \\ x_0' \end{pmatrix}. \tag{4.28}$$

Again, note that $\eta > 0$ is focusing, while $\eta < 0$ is defocusing. In general, the best practice is usually to tilt both faces by half the bend angle which makes both faces defocusing in x. This allows the beam trajectory to stay closer to the center axis of the magnet which minimizes field errors.

The effect in the vertical direction is exactly opposite, in fact one could model the entrance as a single thin quadrupole lens. The reason is that there must be a vertical curvature to the fringe fields in order to satisfy the Maxwell equations at the edge. Consider the geometry in Fig. 4.1. The static magnetic field must satisfy $\nabla \times \boldsymbol{B} = 0$. This means that

$$\frac{\partial B_y}{\partial h} = \frac{\partial B_h}{\partial y}. \tag{4.29}$$

Expanding B_h about the mid-plane,

$$B_h(y) \approx y \frac{\partial B_h}{\partial y}\Big|_{y=0} + ..., \tag{4.30}$$

where we have used the fact that $B_h(0) = 0$. The component along the face, using Eq. (4.29) is

$$B_{face} = y \frac{\partial B_y}{\partial h} \sin\eta. \tag{4.31}$$

Integrating this along $ds = dh/\cos\eta$, we find the change in vertical velocity

$$\Delta y' = \frac{y}{R} \tan\eta, \tag{4.32}$$

where R is the design bending radius. So the fringe fields act again just like a thin lens, except with opposite sign from the edge focusing in the horizontal direction. The transfer matrix is

$$\begin{pmatrix} y \\ y' \end{pmatrix} = \begin{pmatrix} 1 & 0 \\ \frac{1}{R}\tan\eta & 1 \end{pmatrix} \begin{pmatrix} y_0 \\ y_0' \end{pmatrix}. \tag{4.33}$$

4.7 Particle-in-Cell Method

Given that we can calculate the response of a collection of discrete charges to fields, we still have two important tasks to accomplish. Since the fields are to be calculated at grid points, but the electrons have continuous spatial coordinates, we must interpolate the forces. Secondly, if the electrons are to act as the source for wave equations, the charges must be assigned to grid points. In the particle-in-cell method [49], the individual electrons of a bunch are represented by macroparticles. In a 1 nC bunch, there are roughly 6.25×10^9 electrons. It is generally impractical

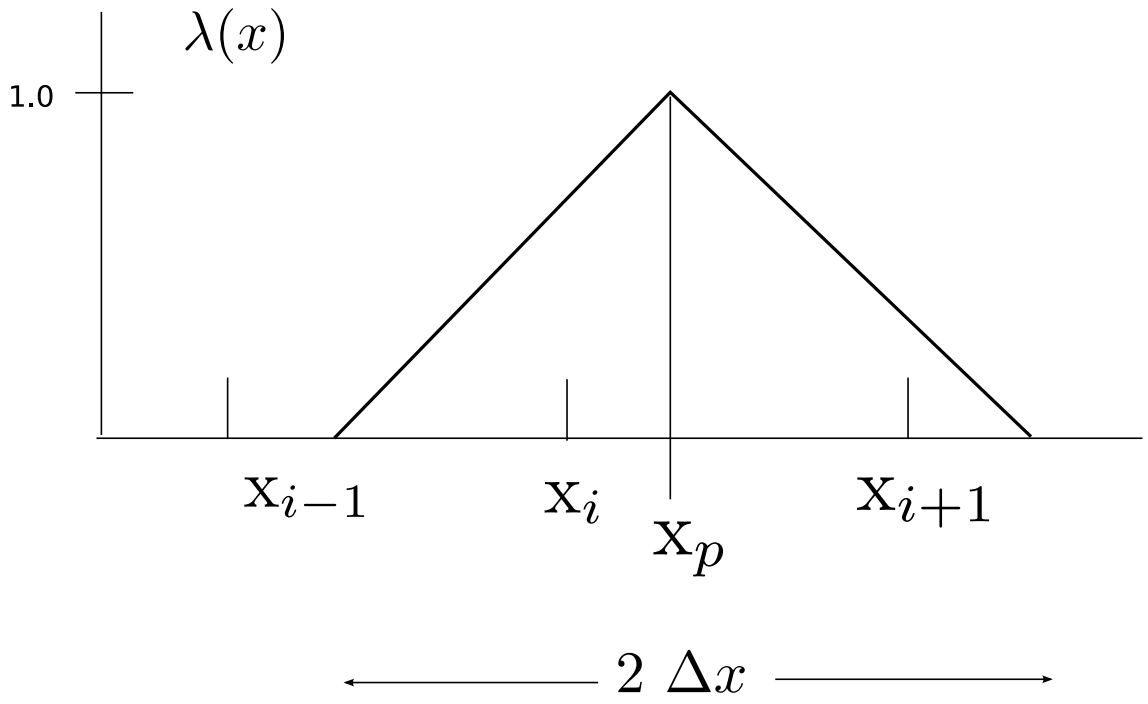

Figure 4.2: Cloud-in-cell charge assignment function for the one-dimensional case. If the charge is located directly on a grid point then all of the charge is assigned there. Otherwise there will always be two grid points receiving charge assignment. The cloud size may be made larger than $2\Delta x$.

to represent each charge. Each electron is described by six phase-space coordinates: x, y, z, v_x, v_y, and v_z. Assuming single precision, a computer takes four bytes to store a single precision floating point number. Therefore, it will take 24 bytes to store a single electron's phase-space coordinates. So, theoretically, one could store the entire bunch in something like 150 GB. However it is usually faster to store the particles in RAM, but it would take an extraordinary computer to do so using every electron. We can choose, on the other hand, to represent some number of electrons by a single macroparticle with the phase-space coordinates equal to the mean coordinates of the electrons comprising the macroparticle.

The simplest form for charge assigment is called nearest-grid-point (NGP). As the name implies, all of the charge from each macroparticle is assigned to the closest grid point. Regardless of the number of space dimensions, all of the charge is always assigned to a single grid location. An improvement is the technique called cloud-in-cell (CIC). In this case, the charge is generally assigned to 2^n grid points where n is the number of dimensions. Of course, we will be using three dimensions, so each cell is bordered by eight grid points. For illustrative purposes, it is easier to begin with a one-dimensional charge assignment, then generalize. The charge assignment function for one dimension is shown in Fig. 4.2. Every macroparticle lies between two grid points. The charge is assigned proportionally, depending on the distance from the grid point. For CIC, the proportionality is linear. One may extend the size of the cloud to include up to four points (in the one-dimensional case), but the proportionality remains linear. The next level of complexity is to use a quadratic charge assignment function, and this is called triangularly-shaped-cloud (TSC).

The differences between the methods are twofold. Simpler schemes, such as NGP tend to have more noise, while less noisy schemes like TSC tend to be more complex and therefore slower. Because of the discrete nature of electrons, there will always be some shot noise. If we use macroparticles, one may expect more noise. Consider, for example, a finite volume, within which we may want to know the total charge. If there are, on average $\bar{N}$ electrons in the volume cell, then because of

random fluctuations, the total charge may vary in the root-mean sense by

$$\frac{\Delta\bar{Q}^2}{\bar{Q}^2} = \frac{1}{\bar{N}}. \tag{4.34}$$

If use fewer macroparticles, where one macroparticle represents N_m electrons, then the noise will increase by the factor $\sqrt{N_m}$. Comparing the noise between schemes is slightly more complicated. In three dimensions the reduction in noise by using CIC compared to NGP is approximately $(3/8)^n$ [50], but the implementation time goes up by a factor of 3^n. In three dimensions, therefore the improvement of CIC over NGP is 1/3 of the noise for the same number of particles, but runs 8 times slower. The next level of complexity is TSC which will assign charges to 27 three-dimensional grid points. However, the noise improvement for TSC does not justify the increase in complexity, so our choice for a balance between noise supression and complexity is to use CIC for charge assignment. Force interpolation can use the same scheme, but in reverse. For a given spatial coordinate, one computes the same factors for each of the eight bordering grid points as for charge assigment, but uses them to proportion the contribution to the total force from each grid point. For consistency, we use the same method (CIC) for both assignment and interpolation.

4.8 Space Charge in Converging/Diverging Beams

The near perfect cancellation between electric and magnetic space-charge forces in relativistic beams is well known. However, there is another space-charge effect from slowly converging/diverging beams which is less well-known. For clarity, the physical situation is the convergence/divergence of an axisymmetric charged-particle

beam caused perhaps by a thin lens such as a solenoid or quadrupole triplet inside a vacuum pipe with constant cross-section. We also assume that the pipe walls are perfectly conducting and grounded (we set the potential to zero at the walls). Within the beam, there will be a variation in energy caused by the potential depression associated with the space-charge fields. As the beam changes shape as a result of convergence/divergence there will be a new potential within the beam. Assuming no radiation, the change in potential must come from a change in kinetic energy. In turn, there must be forces acting on the charged particles which cause the change in kinetic energy. These forces are the space-charge fields we are interested in. We will derive general expressions for the forces and apply the situation to some common beam distributions.

4.9 Derviation of the Space-Charge Forces

Since we are concerned with potential, we will derive the fields from the scalar and vector potentials ϕ and $\boldsymbol{A}$ where

$$\boldsymbol{E} = -\nabla\phi - \frac{1}{c}\frac{\partial \boldsymbol{A}}{\partial t}, \tag{4.35}$$

$$\boldsymbol{B} = \nabla \times \boldsymbol{A}. \tag{4.36}$$

From these fields we form the Lorentz force using

$$\boldsymbol{F} = e(\boldsymbol{E} + \boldsymbol{\beta} \times \boldsymbol{B}). \tag{4.37}$$

We choose a cartesian coordinate system (x, y, s) where s is along the axis of

the beam in its direction of motion. The relevant fields are

$$E_x = -\frac{\partial\phi}{\partial x} - \frac{1}{c}\frac{\partial A_x}{\partial t}, \tag{4.38}$$

$$B_y = \frac{\partial A_x}{\partial s} - \frac{\partial A_s}{\partial x}, \tag{4.39}$$

$$E_s = -\frac{\partial\phi}{\partial s} - \frac{1}{c}\frac{\partial A_s}{\partial t}. \tag{4.40}$$

Now, we change coordinates, introducing $z = s - \beta_0 ct$ changing the independent variable ct to τ. Now

$$E_x = -\frac{\partial\phi}{\partial x} - \frac{\partial A_x}{\partial \tau} + \beta_0\frac{\partial A_x}{\partial z}, \tag{4.41}$$

$$B_y = \frac{\partial A_x}{\partial z} - \frac{\partial A_z}{\partial x}, \tag{4.42}$$

$$E_s = -\frac{\partial\phi}{\partial z} - \frac{\partial A_z}{\partial \tau} + \beta_0\frac{\partial A_z}{\partial z}. \tag{4.43}$$

Collecting terms for the forces

$$F_x = e\left[-\frac{\partial\phi}{\partial x} - \frac{\partial A_x}{\partial \tau} + (\beta_0 - \beta_s)\frac{\partial A_x}{\partial z} + \beta_s\frac{\partial A_z}{\partial x}\right] \tag{4.44}$$

$$F_z = e\left[-\frac{\partial\phi}{\partial z} - \frac{\partial A_z}{\partial \tau} + \beta_0\frac{\partial A_z}{\partial z}\right] \tag{4.45}$$

We can further simplify these expressions noting that the potentials satisfy the following wave equations in the Lorentz gauge, where $\nabla\cdot\boldsymbol{A} = -\partial\phi/c\partial t$,

$$\left(\nabla^2 - \frac{1}{c^2}\frac{\partial^2}{\partial t^2}\right)\phi = -4\pi\rho, \tag{4.46}$$

$$\left(\nabla^2 - \frac{1}{c^2}\frac{\partial^2}{\partial t^2}\right)\boldsymbol{A} = -4\pi\boldsymbol{\beta}\rho, \tag{4.47}$$

where ρ is the charge density. In cartesian coordinates, $\nabla^2\boldsymbol{A} = (\nabla^2 A_x)\boldsymbol{e}_x + (\nabla^2 A_y)\boldsymbol{e}_y + (\nabla^2 A_z)\boldsymbol{e}_z$, the components of the vector potential satisfy the same wave equation as the scalar potential except at the source is multiplied by the components of $\boldsymbol{\beta}$. Next we discuss the boundary conditions on ϕ and $\boldsymbol{A}$.

We already have one of the boundary conditions on ϕ by assumption, namely that $\phi = 0$ everywhere on the walls. The rest we must deduce from the boundary conditions for the fields at the walls of a perfect conductor. They are

$$E_{y,z}|_{x=\pm a/2} = 0, \tag{4.48}$$

$$B_x|_{x=\pm a/2} = 0, \tag{4.49}$$

$$\frac{\partial E_x}{\partial x}\Big|_{x=\pm a/2} = 0, \tag{4.50}$$

$$\frac{\partial B_{z,y}}{\partial x}\Big|_{x=\pm a/2} = 0, \tag{4.51}$$

$$E_{x,z}|_{y=\pm b/2} = 0, \tag{4.52}$$

$$B_y|_{y=\pm b/2} = 0, \tag{4.53}$$

$$\frac{\partial E_y}{\partial y}\Big|_{y=\pm b/2} = 0, \tag{4.54}$$

$$\frac{\partial B_{x,z}}{\partial y}\Big|_{y=\pm b/2} = 0. \tag{4.55}$$

In terms of potentials, let us first restrict the discussion to where there is only an A_z component because $\boldsymbol{\beta}_\perp = 0$. From the gauge condition, this now implies that

$$\frac{\partial A_z}{\partial z}\Big|_{wall} = 0. \tag{4.56}$$

From $E_z = 0$ we can also infer

$$\frac{\partial A_z}{\partial t}\Big|_{wall} = 0. \tag{4.57}$$

and from $B_x = 0$ at $x = \pm a/2$ and $B_y = 0$ at $y = \pm b/2$,

$$\frac{\partial A_z}{\partial y}\Big|_{x=\pm a/2} = 0, \tag{4.58}$$

$$\frac{\partial A_z}{\partial x}\Big|_{y=\pm b/2} = 0. \tag{4.59}$$

Lastly, from the conditions on E_x and B_y at $x = \pm a/2$,

$$\left.\frac{\partial^2 \phi}{\partial x^2}\right|_{x=\pm a/2} = 0, \tag{4.60}$$

$$\left.\frac{\partial^2 A_z}{\partial x^2}\right|_{x=\pm a/2} = 0. \tag{4.61}$$

Similarly,

$$\left.\frac{\partial^2 \phi}{\partial y^2}\right|_{y=\pm b/2} = 0, \tag{4.62}$$

$$\left.\frac{\partial^2 A_z}{\partial y^2}\right|_{y=\pm b/2} = 0. \tag{4.63}$$

Leaving the only possible difference between ϕ and A_z as a constant, which we are free to choose to be zero, making them identical.

We can now conclude for the case of axial motion only that $A_z = \beta_z \phi$. Rewriting the forces

$$F_x = -e\frac{1}{\gamma^2}\frac{\partial \phi}{\partial x}, \tag{4.64}$$

$$F_z = e\left[-\frac{1}{\gamma^2}\frac{\partial \phi}{\partial z} - \beta_0 \frac{\partial \phi}{\partial \tau}\right], \tag{4.65}$$

where $\gamma = \sqrt{1-\beta_0^{-2}}$. The familiar γ^{-2} scaling is manifestly demonstrated in both terms. However, there remains a time dependent term in the longitudinal force. This term is the force that will change the kinetic energy in an amount approximately equal to the change in potential of the beam. We see this easily by integration

$$\phi(t) - \phi(0) = \frac{1}{e}\int_0^{ct} F_z^{int}\frac{d\tau}{\beta_0}. \tag{4.66}$$

Compare this with the change in total energy

$$\left[\gamma(t) - \gamma(0)\right] mc^2 = \int_0^{ct} F_z \beta d\tau. \tag{4.67}$$

We see that

$$[\gamma(t) - \gamma(0)]\, mc^2 \approx e\beta_0^2\, [\phi(t) - \phi(0)]\,, \tag{4.68}$$

where the approximation comes from the assumption that β remains unchanged over the integration path. From conservation of energy, neglecting the additional factor of $\beta^2 \approx 1$, this is what one would expect: the change in potential resulting from convergence/divergence of the beam in a waveguide must come from the same change in the kinetic energy of the beam which is caused by a longitudinal force directly proportional to the rate of change in potential necessary to balance the energy conservation law. This seems to be the case based on the discussion above, but there still remains the factor of β^2 instead of unity. The difference is easily seen by writing $\beta^2 = 1 - \gamma^{-2}$. Now, as long as $\gamma \gg 1$, there essentially is no difference, or at least the difference is small. On the other hand, if $\beta \to 0$, there will be no kinetic energy change, and no longitudinal force, regardless of how the potential is changed.

So we see that this is not a conservative system in the usual sense. Of course, to change the potential without motion of the beam would require an external energy source of some sort. Likewise, holding the potential of the walls at zero while the beam changes its potential, as seen above requires an additional energy loss

4.10 The Talman Force and Cancellation Effect

We have already introduced the transverse CSR and demonstrated how it is calculated by simulation, as well as compared it to theory for the rigid beam case.

The net force is transverse and centrifugal, in the direction away from the center of the bend. One should also note that the transverse force increases as the beam radius decreases. In the limit of a line charge, the transverse force is logarithmically divergent. So what allows thin beams to be successfully transported around bends without being forced to the outside wall? We have described it: potential depression. We will now show that the effect of potential depression and divergent portion of the transverse force on the transverse dynamics cancel each other perfectly, at least initially, and therefore it is essential to properly initialize the beam.

The Talman force [15] is a divergent type of space-charge force arising from the curvilear trajectory. We already derived the forces in terms of potentials ϕ and $\boldsymbol{A}$. The Talman force is

$$F_x^T = e\frac{\beta A_z}{R}. \tag{4.69}$$

We have already discussed that in the straight section, $A_z = \beta\phi$, so we take this as the initial condition. Similarly, the initial energy deviation $\delta(0) = -e\beta^2\phi(0)/\gamma mc^2$. Substituting into Eq. (4.20), we see that the last two terms on the right hand side cancel exactly and we are left with only the natural betatron motion in a dipole magnet, $x'' = -x/R^2$. Therefore, proper intialization of the beam potential depression is essential, especially in the case of a very thin beam where the Talman force will be quite large.

Chapter 5

Self-Consistent Simulations

In chapter 3, we tested the field solver against theory for the case when the charge distribution was rigid. Even in a simple bend, however, for a three-dimensional beam, this is certainly not the correct behavior. We have already shown that for high energies, the beam velocities are nearly the same to a high degree of accuracy. This means that the individual electron trajectories follow elliptic paths in $x - z$ space. Also the beam may be converging or diverging because of either edge/fringe field focusing or the natural betatron motion in a dipole magetic field. So we would like to test our simulation against what we know from theory in a piece-wise fashion. To begin with, let us ignore the effects of curvature and waveguide boundaries and consider the motion of a relativisitic beam in a vacuum drift space.

5.1 Drift Space

In a drift space, ignoring boundary walls and longitudinal effects, we have two factors that dominate the transverse dynamics. First, there is the statistical variation in transverse velocities, characterized by the transverse emittance. There are several conventions for the emittance, so now we will define ours. The macroparticle bunch consists of N particles each of which will have a six-dimensional phase space

Table 5.1: Drift Space Test Case Parameters.

Parameter	Symbol	Value
Design energy	E	20 MeV
Charge	Q	1 nC
Perveance	$K/4$	$5 \times 10^{-}9$
Rms emittance	$\tilde{\epsilon}_x$	1 mm-mrad
Initial rms width	x_0	0.3 mm
Initial angle	x'_0	10^{-4}
Betatron function	β_0	= 3.91 m
Alpha function	α_0	3.85 m^{-}1

coordinates, x, y, z, x', y' and $\delta p/p$. We can define the first and second moments for any coordinate as follows

$$\bar{x} = \frac{1}{N} \sum_i x_i, \tag{5.1}$$

$$\bar{x^2} = \frac{1}{N} \sum_i x_i^2. \tag{5.2}$$

The *rms emittance* is defined by

$$\tilde{\epsilon}_x = \left[\bar{x^2}\bar{x'^2} - (\bar{xx'})^2\right]^{1/2}. \tag{5.3}$$

The *normalized rms emittance* $\tilde{\epsilon}_{nx} = \beta\gamma\tilde{\epsilon}_x$ is often a better measure of the beam quality when comparing one machine to another at a different energy. The units of

emittance are $m - rad$, but are often expressed in $mm - mrad$ or simply μm.

The requirements on beam emittance depend on the application. For a free electron laser (FEL) in an oscillator configuration, the maximum emittance depends on the optical wavelength such that

$$\tilde{\epsilon}_{nx,y} \leq \beta\gamma\frac{\lambda}{4\pi}. \tag{5.4}$$

For example if the operating wavelength is 1 μm, and $\gamma = 200$, then $\tilde{\epsilon}_{nx,y} \leq 16$ μm. Note that this limit is based simply on matching the beam envelope to the optical mode for maximum overlap.

We also have the collective repulsion of the electrons, or space-charge which we have already described in some detail. We can describe the evolution of the envelope using following equation for the beam radius $x_m(s)$ from Reiser [51]

$$x_m'' = \frac{\epsilon_x^2}{x_m^3} + \frac{K}{x_m}, \tag{5.5}$$

where K is the generalized perveance defined by

$$K = \frac{2I}{I_0\beta^3\gamma^3} \tag{5.6}$$

characterizes the space-charge repulsion, and the emittance characterizes the statistical variation. For a non-continuous beam, the current is $\beta c\lambda(z)$. If we have a Gaussian distribution in the longitudinal coordinate, then

$$\lambda(z) = \frac{Ne}{\sqrt{2\pi}\sigma_z}e^{-z^2/2\sigma_z^2}. \tag{5.7}$$

This strictly applies to laminar flow and linear space-charge forces like those from a K-V distribution [52] where x_m is the beam width. This can be extended to a

general distribution by the use of the *rms equivalent beam* where the beam envelope x_m is replaced by rms $\tilde{x}$. In this form the rms equation is

$$\tilde{x}'' = \frac{\tilde{\epsilon}_x^2}{\tilde{x}^3} + \frac{K}{4\tilde{x}}, \tag{5.8}$$

where the emittance $\tilde{\epsilon}_x$ is now also defined in terms of rms quantities. If one term dominates, the beam is either *space-charge* or *emittance* dominated. The ratio of terms

$$\chi = \frac{K\tilde{x}^2}{4\tilde{\epsilon}_x^2} \tag{5.9}$$

is a convenient measure, where $\chi > 1$ is space-charge dominated, and *vice-versa*.

To demonstrate that simulation follows the rms envelope equations in the emittance-dominated regime is interesting, but the space-charge dominated case is much more relevant. This would show not only response of the particles to self-fields, but proper computation of the self-fields in a dynamical situation. Of course, we need to be careful of two things: that the boundaries are far enough away to not influence the self-fields, and that the beam is long enough that longitudinal effects can be ignored. To make sure we satisfy the first condition, we can look at the analytical form of the space-charge force (in vacuum) from a charge distribution

$$\rho(r,z) = \frac{Ne\lambda(z)}{2\pi\sigma_r^2} e^{-r^2/2\sigma_r}. \tag{5.10}$$

Gauss' law becomes

$$2\pi r E_r(r,z) = 4\pi \int_0^r 2\pi r' \rho(r',z) dr', \tag{5.11}$$

which we solve resulting in

$$E_r(r,z) = \frac{2\lambda(z)}{r}(1 - e^{-r^2/2\sigma_r^2}). \tag{5.12}$$

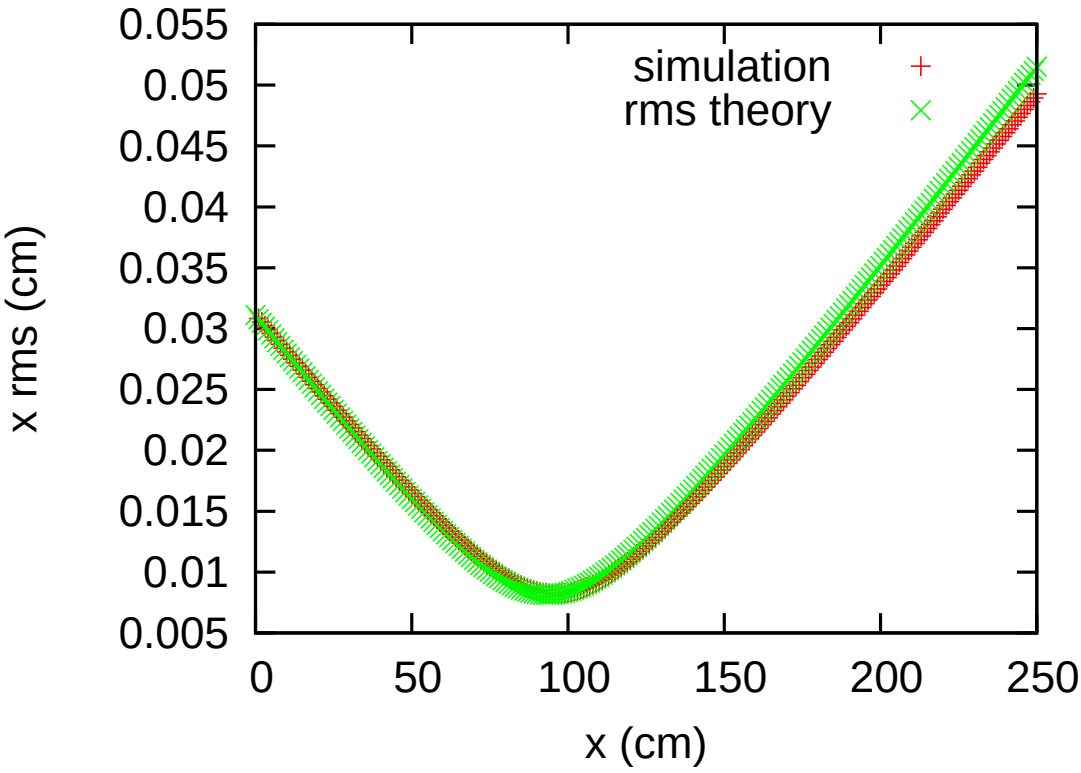

Figure 5.1: Beam envelope simulation compared to theory. The simulation was modified to use the steady-state space-charge forces at all times, and a very long beam approximation so that there are no longitudinal effects.

We can at the transverse field components (taken at $z = 0$ along the x-axis where $r = x$) and compare the vacuum theory to the waveguide simulation and see if there is a difference inside the beam. If not, then we have chosen the boundary far enough away so that it does not influence the result.

To satisfy the second condition we could make the beam long relative to the width and height. However, this would be very slow to simulate, and because we cannot separate the radiative effects in the full simulation, it has been modified for this test case. We take the steady-state solutions, and disregard the longitudinal effects. This can easily be accomplished by the same method we use to intialize the fields. Recall the wave equation, Eq. (3.5). By setting the time derivative to zero we obtain the steady-state solution

$$\hat{\boldsymbol{E}}_{\perp}^{ss}(\boldsymbol{k}) = \frac{4\pi\nabla\hat{\rho}(\boldsymbol{k})}{k_{\perp}^2 + k_z^2/\gamma^2}. \tag{5.13}$$

If the beam is long and/or the energy is high, the contribution from k_z^2/γ^2 will be small, thus meeting the requirements of our second condition. To compute the forces, in a straight section we simply use

$$\hat{\boldsymbol{F}}_{\perp}^{ss}(\boldsymbol{k}) = \frac{4\pi\nabla\hat{\rho}(\boldsymbol{k})}{\gamma^2(k_{\perp}^2 + k_z^2/\gamma^2)}. \tag{5.14}$$

We compare the results of our modified simulation, with a simple numerical integration of Eq. (5.8). The parameters for the simulation and numerical integration are shown in Table 5.1. The ratio of space-charge to emittance effects $\chi = 0.8$ initially. The results between the two methods are shown in Fig. 5.1. There is a small disagreement, but it turns out this case is very sensitive to the intial conditions.

Furthermore, in the simulation, because we are using a randomly populated distribution to initialize the macroparticles, there will always be slight variations from run to run. Nonetheless, within the range of accuracy for both methods we see the correct behavior of the simulation for a case which includes both self-consistently determined space-charge forces as well as statistical variations. From this we conclude that at least the transverse dynamics appears to be correct.

5.2 Converging Beam in Straight Waveguide

We have already seen that the simulation can replicate the space-charge forces (in all three directions) in a steady-state condition. The reason for this is simple: the relativistic form of the Poission equation is already contained in the paraxial wave equation for the transverse fields. In steady-state, the Lorentz forces are $\boldsymbol{F}_\perp = \boldsymbol{E}_\perp/\gamma^2$ and the fields can be derived from a single potential $\boldsymbol{E}_\perp = -\nabla\phi$. However, when the beam in converging or diverging, even in a straight waveguide, there is another kind of longitudinal space-charge force which we have already discussed in chapter 4. Now that we have encorporated the particle motion into the simulation, it should be interesting to test if the simulation will generate the correct longitudinal force , which when integrated should provide exactly the right energy modulation to match the potential depression (assuming that the waveguide cross section remains constant).

To test this, we start with an axisymmetric laminar beam that is focused by a thin lens with focal length f_0. At a distance $s = f_0/2$, we place a second thin

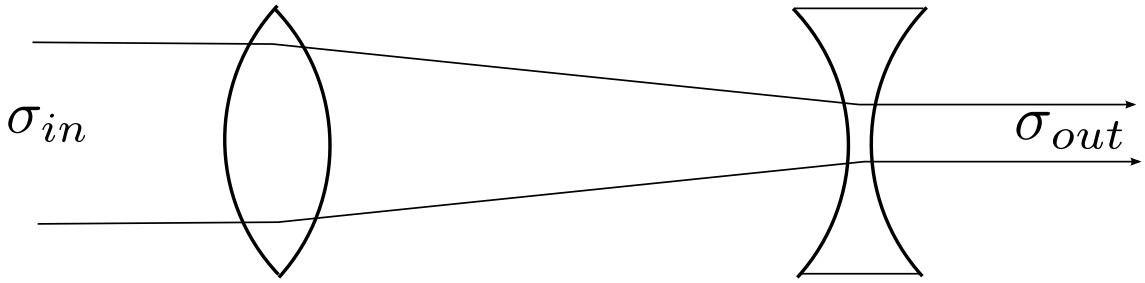

Figure 5.2: Geometry for converging beam test case. An axisymmetric laminar beam with initial rms radius σ_{in} is first focused by a thin lens with focal length f_0. The second lens is defocusing with focal length $= f_0/2$, resulting in a laminar beam with rms radius $\sigma_{out} = \sigma_{in}/2$.

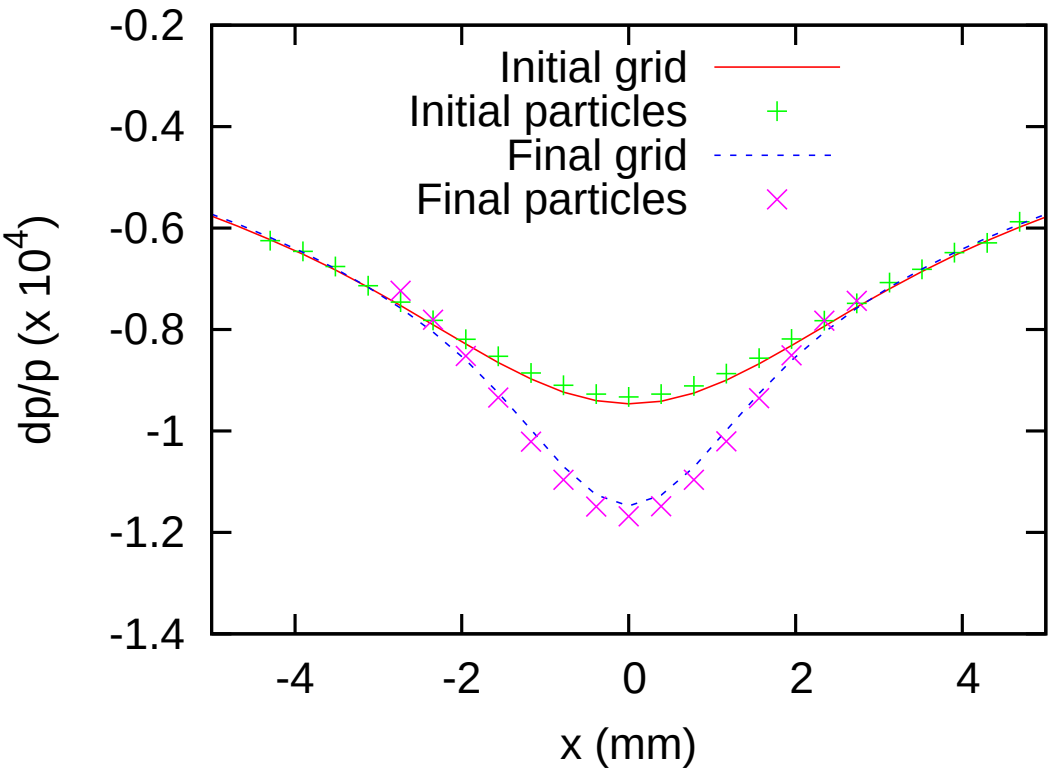

Figure 5.3: Comparison of the initial and final potential depression as measured both by the field and particle solvers of the simulation. The beam starts in laminar flow and is focused axisymmetrically to half its original beam width. The simulation used two thin lenses, separated by 50 cm, acting as a telescope.

lens with focal length $-f_0/2$ that restores the beam to laminar flow, but at half the original beam radius. The waveguide cross section is constant. Comparing the intial and final beams, because of the increased space-charge, the final beam should have a greater potential depression. We expect this to come from a longitudinal force in a direction as to decrease the beam energy, and of appropriate magnitude so that the final change in beam energy matches the change in potential depression. We can solve for the potential depression in the same way that we intialize the fields, using the Fourier transform

$$\hat{\phi}(\boldsymbol{k}_\perp, k_z) = \frac{4\pi\hat{\rho}(\boldsymbol{k}_\perp, k_z)}{k_\perp^2 + k_z^2/\gamma^2}. \tag{5.15}$$

To initialize the beam, we apply this potential after creating the charge distribution. After compression, we can calculate the potential depression in the same way, as if we were initializing a new beam at that radius. For the simulation, we track the macroparticles through compression then take a slice at $z = 0$ and compare to the potential depression as a function of x. The results are shown in Fig, 5.3 showing a reasonable agreement. From this we conclude that the method we have chosen to calculate the longitudinal fields is consistent with the theory of space-charge in converging beams, and which is vitaly important to correctly model in order to nearly cancel the logarithmically divergent Talman force.

5.3 Bunch Compressor Chicanes

We now turn to the application of the simulation to real systems. There are two main types of bending systems: 180^o turns or bunch compressor chicanes.

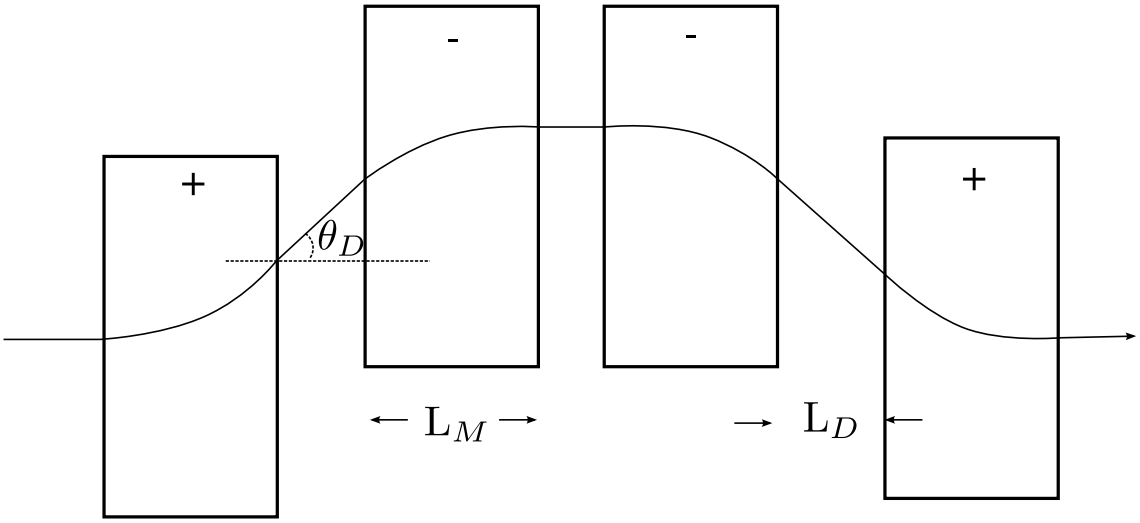

Figure 5.4: Bunch compressor chicane consisting of four dipole magnets. The first and last magnets have the same polarity which is opposite of the middle two. All magnets have identical field strengths. The distance between the second and third magnet does not affect the compression strength. The bending angle is θ_D, the projected length of the magnet is L_M and the separation between magnets is L_D. The path through the chicane corresponds the reference energy. Particles with higher energy will take shorter path and particles with lower energy will take a longer path, therefore a bunch with a linear energy chirp will either compress or expand accordingly.

We will concentrate on the latter, specifically because at the short pulse lengths they are designed to create, they may be a potent source for CSR. The design of a typical bunch compressor chicane (BCC) is illustrated in Fig. 5.4. It consists of four dipole magnets connected by drift sections. The outer pair and inner pair have opposite polarity. Here, the magnet entrance is shown perpendicular to the beam, although it is sometime angled at half the bending angle in order to keep the electron beam trajectory closer to the center of the magnet and therefore minimize the effects of field errors. For our simulations, we will assume the effects of edge focusing/defocusing and fringe fields can be described by an equivalent thin lens. Note that every face not perpendicular to the trajectory will generally be defocusing in x and focusing in y.

If the electron beam is monoenergetic, the BCC will simply deflect the beam to the side and back. This often done in FEL oscillator designs to make room for the optical cavity mirrors. On the other hand, if the beam is accelerated off-phase, there will be an energy correlation with z. We will approximate off-phase acceleration as a perfectly linear energy chirp $\delta = -\alpha z$. The path length change from an energy deviation in the linear approximation is denoted as M_{56}, consistent with the matrix method, and for the symmetric four dipole BCC is given by

$$M_{56} = 2\left[2R(\theta_D - \tan\theta_D) - L_D\frac{\sin^2\theta_D}{\cos^3\theta_D}\right]. \tag{5.16}$$

In general, the linear term is insufficient to accurately predict the actual compression and if using the matrix method one needs an additional term M_{566} which describes the path length dependence on δ^2. We will not need this however, because we are

not using the matrix method and our dynamics actually model the path length variation to all orders in δ.

5.3.1 Estimation of Emittance Dilution

To understand the effect that CSR fields have on transverse emittance and as a way to make rough estimates, we follow the method used by Carlsten [53]. The main assumption is that main effect appears as a change in the value of $\bar{x'^2} \rightarrow \bar{x'^2} + \Delta\bar{x'^2}$. We assume that the change in $\bar{x^2}$ is small. This is reasonable for the types of beams we are considering because the unperturbed value of $\bar{x'^2}$ is quite small indeed. The presence of a perturbing field with rms spread W_{rms}, which we also assume to be constant alters the spread in energy over a distance Δs by

$$\Delta\delta_{rms} = \frac{W_{rms}}{\gamma mc^2}\Delta s. \tag{5.17}$$

This, in turn, creates a rms spread in x' of

$$\Delta x'_{rms} = \frac{W_{rms}}{\gamma mc^2}\frac{\Delta s^2}{2R}. \tag{5.18}$$

The resulting change in normalized emittance is

$$\Delta\tilde{\epsilon}_{nx} \approx \tilde{x}\frac{W_{rms}}{mc^2}\frac{\Delta s^2}{2R}. \tag{5.19}$$

Using the steady-state longitudinal CSR field for a Gaussian beam, we can use Eq. (5.19) to estimate the peak current that may can be transported through a single bend before the transverse emittance is increased significantly. Our estimate will depend on six factors: the initial emittance, the energy, the bending angle, the bend radius, the pulse length, and the betatron function. The betatron function

is used to estimate the rms beam width (in the x direction). This is based on the assumption that the beam is at a waist and the beam width can be determined from

$$\tilde{x} = \sqrt{\frac{\beta\epsilon_{n,x}}{\gamma}}. \tag{5.20}$$

For the CSR field we use the basic scaling for a Gaussian

$$W_{rms} = \sqrt{\frac{2}{\pi}}\frac{Ne^2}{(3\sigma^2 R)^{2/3}} \tag{5.21}$$

Finally, we assume that the criteria for significant emittance dilution is when $\Delta\epsilon/\epsilon \gtrsim 1$. This establishes a maximum bunch charge $Q = Ne$ for a given set of parameters, which in turn can be expressed in terms of peak current, or peak brightness. The relation between Q and peak current is assumed to be

$$I_{peak} = \frac{Qc}{\sqrt{2\pi}\sigma_z}. \tag{5.22}$$

The limit is

$$N_{max} < \sqrt{\frac{2\pi\gamma}{\beta\epsilon_{n,x}}}\frac{1}{r_0\theta^2}\left(\frac{9\sigma_z^4}{R}\right)^{1/3}, \tag{5.23}$$

where $r_0 = e^2/mc^2$ is the classical electron radius.

We can also estimate the average energy loss of the beam. Once again assuming a constant field at the steady-state value, and rearranging some terms

$$\Delta E = N\sqrt{\frac{2}{\pi}}\frac{r_0\theta_D R}{(3\sigma_z^2 R)^{2/3}} \times 0.511 \text{ MeV}. \tag{5.24}$$

5.3.2 CSR Workshop Benchmark Chicane

To begin with, we model the benchmark BCC from the 2002 CSR Workshop [54], which is representative of the x-ray FEL driver designs, for example such as

Table 5.2: CSR Workshop Chicane Bunch Compressor Parameters.

Parameter	Symbol	Value
Design energy	E	5 GeV
Bend magnet length (proj.)	L_M	0.5 m
Drift length (proj.)	L_D	5.0 m
Inner magnet spacing	L_I	1.0 m
Bend radius at design energy	R	10.35 m
Vertical gap	b	0.5 cm
Horizontal gap	a	30 cm

LCLS [55] or TESLA-XFEL [56]. This type of BCC is characterized by shallow angles with very large drift sections between the dipole magnets. The parameters for the chicane and electron beam are shown in Tables 5.2 and 5.3. First let us estimate the bunch charge at which we may begin to see transverse emittance dilution. We assume that all of the growth occurs in the final bend with angle $\theta_D = 2.77^o$, and at full compression $\sigma_z = 20$ μm. Using Eq. (5.23), a rough estimate of the onset emittance dilution is 0.5 nC, so at 1.0 nC we show see at least a noticeable effect.

The results of our simulation, designated SCARS (for Space-Charge and Radiation Simulation), is shown in Fig. 5.5. The purpose of this benchmark was to compare the results from various codes, however this is not entirely possible for our code because we need to specify waveguide boundaries. The benchmark results for

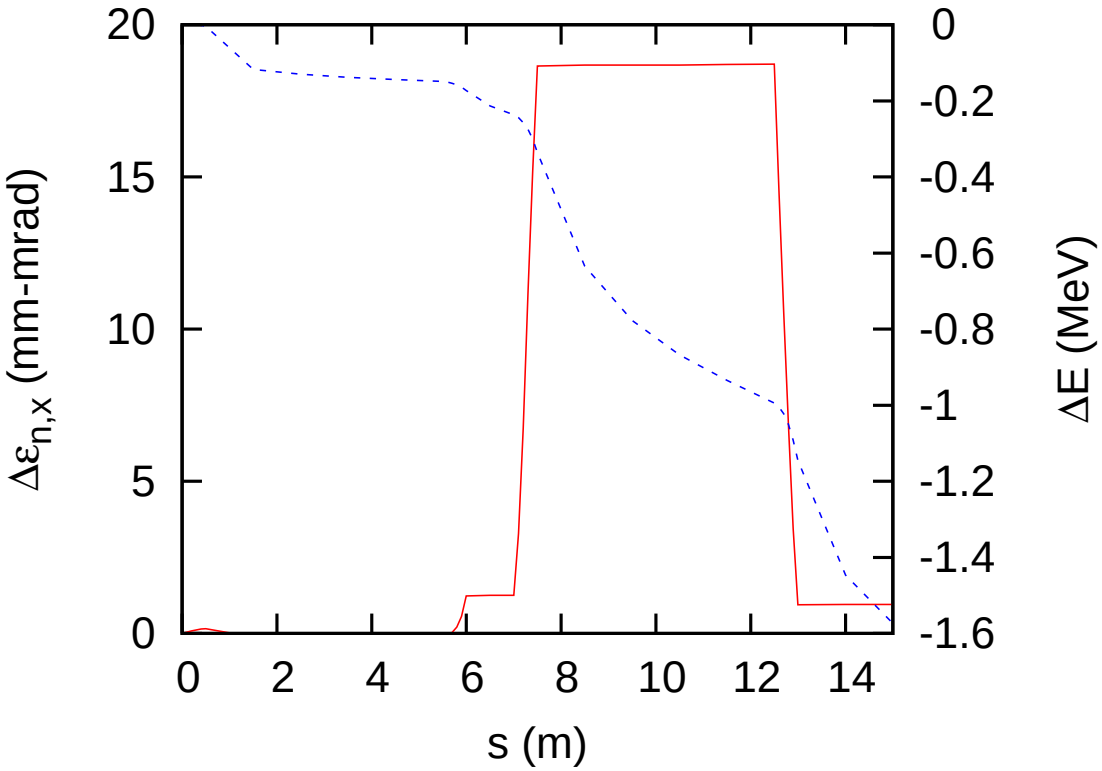

Figure 5.5: Emittance growth (red, solid) and energy loss (blue, dashed) as a function of distance in CSR workshop bunch compressor chicane. The beam is at 5 GeV, 1 nC. The emittance growth is computed as the absolute value of the difference between the 1 nC and the 0 nC simulations. Energy loss is the difference of the average particle energy from 5 GeV.

Table 5.3: CSR Workshop beam parameters.

Parameter	Symbol	Value
Chirp	α	0.36 cm^{-1}
Bunch charge	Q	1 nC
Pulse length (FWHM)	τ	2.3 ps
Initial betatron functions	β_x/β_y	40.0/13.0 m
Initial alpha functions	α_x/α_y	2.6/1.0
RMS norm. emittances	$\epsilon_{n,x}/\epsilon_{n,y}$	1.0/1.0 μm

other codes are only given for the vacuum case. We could approximate vacuum by using very large values for the waveguide dimensions, and therefore set height = 20 cm and the width = 30 cm as an approximation and in order to minimize the effect of the waveguide. The value of emittance inside the chicane is normally quite large because of dispersion. In order to track the emittance growth in this case, we ran the simulation with no bunch charge, and used that as a baseline. The value of emittance as a function of distance is the difference between the simulation at 1.0 nC and zero bunch charge. Plotted on the same graph is the average energy loss of the beam. The rough estimate values for emittance growth and energy loss in the fourth dipole 1.0 nC are 1.0 μm and -0.67 MeV respectively.

The emittance growth is approximately half of the rough estimate, and the cumulative energy loss is of course, much greater. However, the energy loss in

Table 5.4: CSR Workshop Summary.

Code	$\Delta E/E_0$ (%)	$\sigma_{\delta,rms}$ (%)	$\epsilon_{n,x}$ (μm)
SCARS [57]	-0.03	-0.0062	2.0
TraFiC^4 [58]	-0.058	-0.002	1.4
Tredi [59]	-0.041	+0.017	2.3
R. Li [60]	-0.056	-0.006	1.32
Elegant [61]	-0.045	-0.0043	1.55
Emma [62]	-0.043	-0.004	1.52
Dohlus-1 [63]	-0.045	-0.011	1.62
Dohlus-2	-0.043	-0.01	1.57

the fourth dipole alone is fairly close to the estimate at 0.6 MeV. Since this is a benchmark, we compare the results of SCARS to the other codes as reported. Table 5.4 summarizes the results. Among the other codes, only SCARS, TraFiC^4 and Tredi are three-dimensional. The rest are one-dimensional with the exception of the code by R. Li which is two-dimensional.

The benchmark also has a test case for 500 MeV beam energy with all other parameters the same. From our rough estimate, the expected scaling for a tenfold decrease in energy is for the emittance growth to be approximately $\sqrt{10} \approx 3$ times greater. The result from SCARS is an emittance growth of 4.5 μm or 4.5 times the 5 GeV case. Note that the model for energy loss does not scale with energy, so the

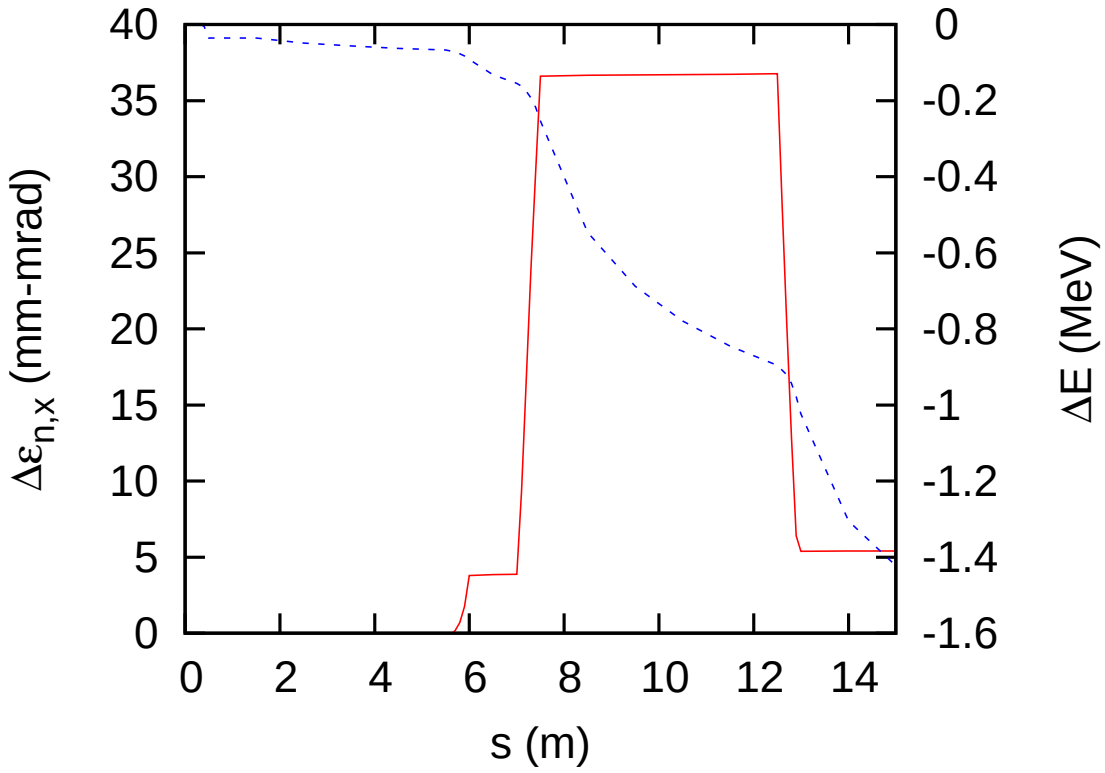

Figure 5.6: Emittance growth (red, solid) and energy loss (blue, dashed) as a function of distance in CSR workshop bunch compressor chicane. The beam is at 0.5 GeV, 1 nC. The emittance growth is computed as the absolute value of the difference between the 1 nC and the 0 nC simulations. Energy loss is the difference of the average particle energy from 0.5 GeV.

expected energy loss estimate is identical to the 5 GeV case. Fewer details were available for other codes, but a simple comparison for other codes on the 500 MeV benchmark case is shown in Table 5.5.

5.3.3 SDL-type Bunch Compressor Chicane

We now consider a different type of bunch compressor chicane, typical of designs for use in the Source Development Lab at BNL or the Jefferson Lab IR-FEL.

Table 5.5: CSR Workshop Summary at 500MeV.

Code	$\epsilon_{n,x}$ (μm)
SCARS	5.5
Tredi	21
R. Li	5.0
Elegant	4.1
Emma	4.05

The chicanes have much larger bending angle and shorter drift sections, and are appropriate for designs with shorter overall footprints. The energy is also much less, at or about 100 MeV. The chicane and beam parameters are shown in Tables 5.6 and 5.7. Again, we use our rough estimates for the maximum bunch charge assuming the final compressed beam has $\sigma_z = 180$ μm, and find the limit to be approximately 0.36 nC. In this case, we will explore scaling in two different parameters: compression, and beam width.

The two different levels of compression are achieved by the amount of energy chirp. Up to a point, the more chirp, the more the bunch will compress. However, it is also possible to over compress the bunch in which case the head and tail switch places. The sign of the chirp is important, too. One will compress the bunch and the other will decompress the bunch (which may be useful for transport). In this case, we mean that the head of the bunch has a lower energy, and therefore travels a longer path in the chicane. In real systems, the chirp can be applied by adjusting

Table 5.6: SDL-type Chicane Bunch Compressor Parameters.

Parameter	Symbol	Value
Design energy	E	85 MeV
Bend magnet length (proj.)	L_M	0.31 m
Drift length (proj.)	L_D	.37 m
Inner magnet spacing	L_I	0.25 m
Bend radius at design energy	R	1.25 m
Vertical gap	b	3.0 cm
Horizontal gap	a	5.0 cm

the phase of the RF accelerating sections, in which case the beam travels through an accelerating cavity not a the peak of the fields but in a place where the fields are changing approximately linearly with entrance time. In our simulations, we did not attempt to model this effect, although it is relatively important when if one wants to acheive the highest compression possible because the nonlinear chirp can somewhat offset the nonlinear variation in path length with energy. Additionally, we will not add any incoherent energy spread, which again would limit the final compression. The reason is that incoherent energy spread tends to mask the energy modulation from CSR, which we are attempting to study.

We will also vary the initial betatron function, which changes the beam width. Because of dispersion, the x rms beam width will expand, reaching a maximum in

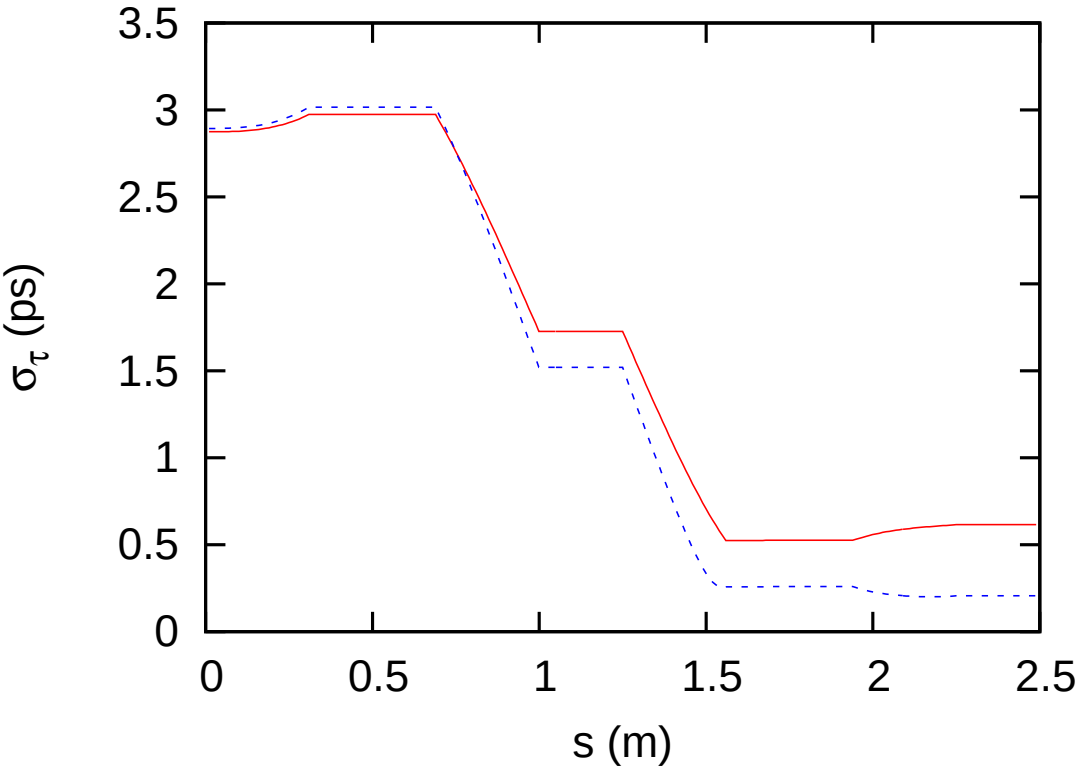

Figure 5.7: Bunch length (rms) as a function of path length in the SDL bunch compressor. The total charge is 0.3 nC. The red lines (solid) corresponds to a linear chirp of 0.105 cm^{-}1 which results in a final rms pulse length of 0.6 ps , and the blue line (dashed) corresponds to a linear chirp of 0.125 cm^{1} and corresponds to a final rms pulse length of 0.2 ps.

Table 5.7: SDL BCC beam parameters.

Parameter	Symbol	Value
Chirp	α	0.105/0.125 cm^{-1}
Bunch charge	Q	0.3 nC
Initial pulse length (FWHM)	τ	10 ps
Initial betatron functions	$\beta_x/\beta y$	15 m
Initial alpha functions	α_x/α_y	0
RMS norm. emittances	$\epsilon_{n,x}/\epsilon_{n,y}$	1 μm

the center of the chicane. If the beam is at a waist, the betratron function is related to the beam width by

$$\tilde{x} = \sqrt{\frac{\beta\tilde{\epsilon}_n}{\gamma}}. \tag{5.25}$$

To double the beam width, one must increase the betatron function by a factor of four. The rms beam width as a function of distance in the chicane is shown in Fig. 5.8. Note that the relationship between beam widths only applies near the ends, where dispersion is the least.

For efficiency, in order to calculate the effect of CSR on emittance as a function of distance along the trajectory in the bunch compressor, we will compensate the effect that dispersion will have on the trajectory using an analytic model, rather than take the difference to a zero charge as was done in the benchmark case. If

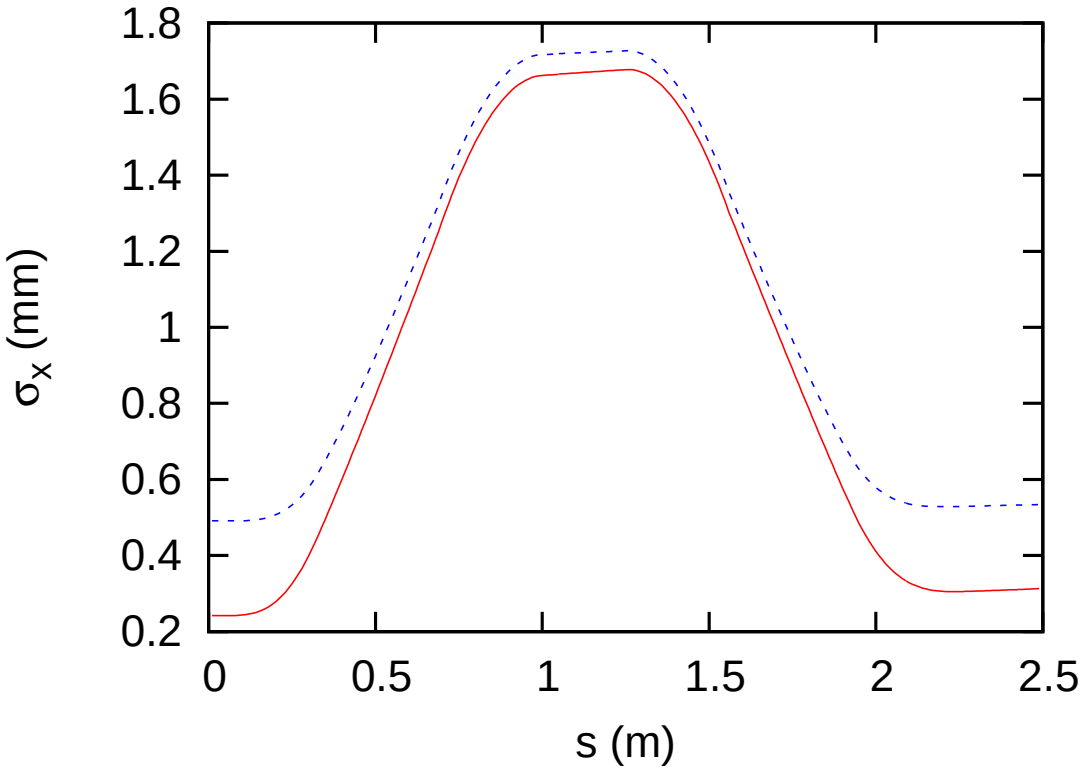

Figure 5.8: Horizontal beam width (rms) as a function of path length in the SDL bunch compressor. The total charge is 0.3 nC. The red lines (solid) corresponds to an intial betatron function of 5 m^{-}1, and the blue line (dashed) corresponds to an intial betatron function of 20 $^{-}$1. The chirp in both cases in 0.105 cm^{-}1.

we just compute the emittance of an unperturbed beam along the path inside the chicane, we will naturally find a great increase beginning shortly from the entrance. The reason is that the large energy chirp is forcing portions at the head and tail respectively to take widely different paths through the chicane. This is after all, how compression is acheived. Based on energy alone, to some extent (i.e. linear model), we can compensate for this apparent emittance growth inside the chicane. One should note that the symmetric chicane, in the absence of self-fields, is doubly achromatic, so that after exiting the chicane, regardless of the energy the trajectory will be exactly the same as it was at the entrance. However, inside the chicane, the tractories will be noticibly altered.

We use our results from the previous chapter, where we derived the linear model for the trajectories in dipole magnetic fields. This has to be applied in stages, also taking into account the edge focusing factors. If the energy deviation is δ, and we assume that it is all coming from the energy chirp applied before the beam entered the chicane, the when we compute the moments in the emittance equation, the dispersion must be subtracted off. We can define the dispersion functions $D(s)$ and $D'(s)$ to be the cumulative result such that the compensated moments are

$$\bar{x}_c = \frac{1}{N}\sum_i [x_i - \delta_i D(s)], \tag{5.26}$$

$$\bar{x'}_c = \frac{1}{N}\sum_i [x_i - \delta_i D'(s)]. \tag{5.27}$$

For the parameters of the SDL bunch compressor, the dispersion functions are shown in Fig. 5.9.

We now show the emittance growth, corrected for dispersion as described

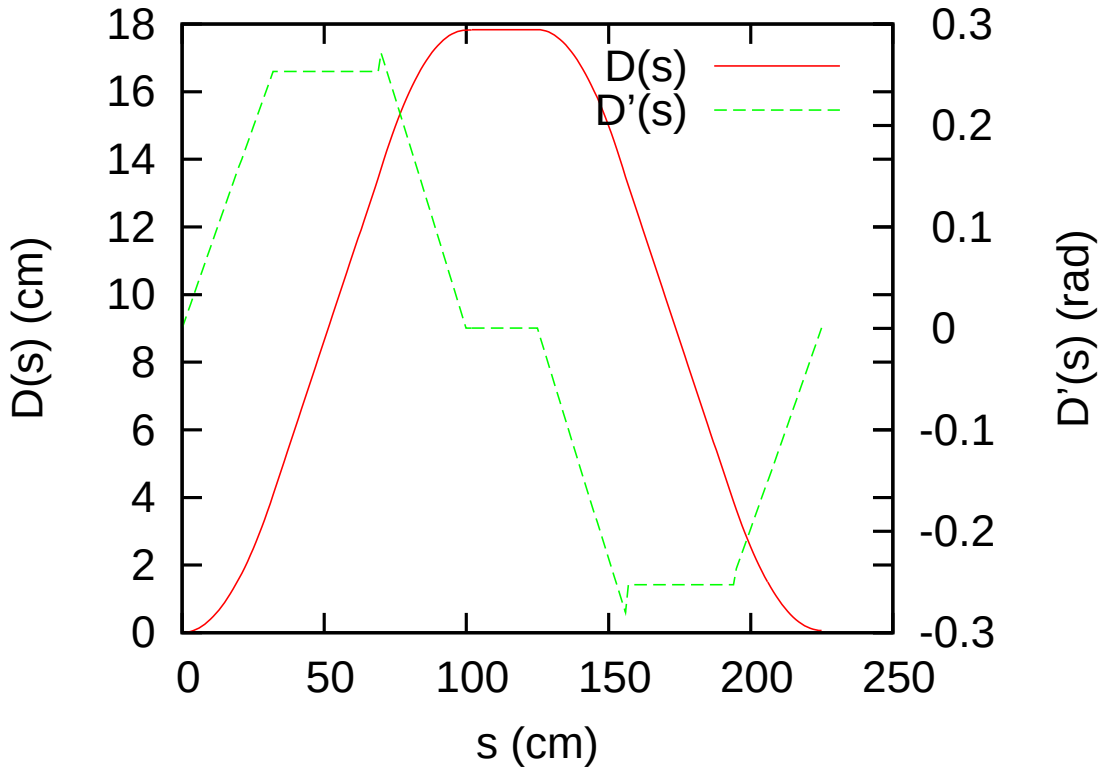

Figure 5.9: Dispersion functions for the SDL bunch compressor parameters.

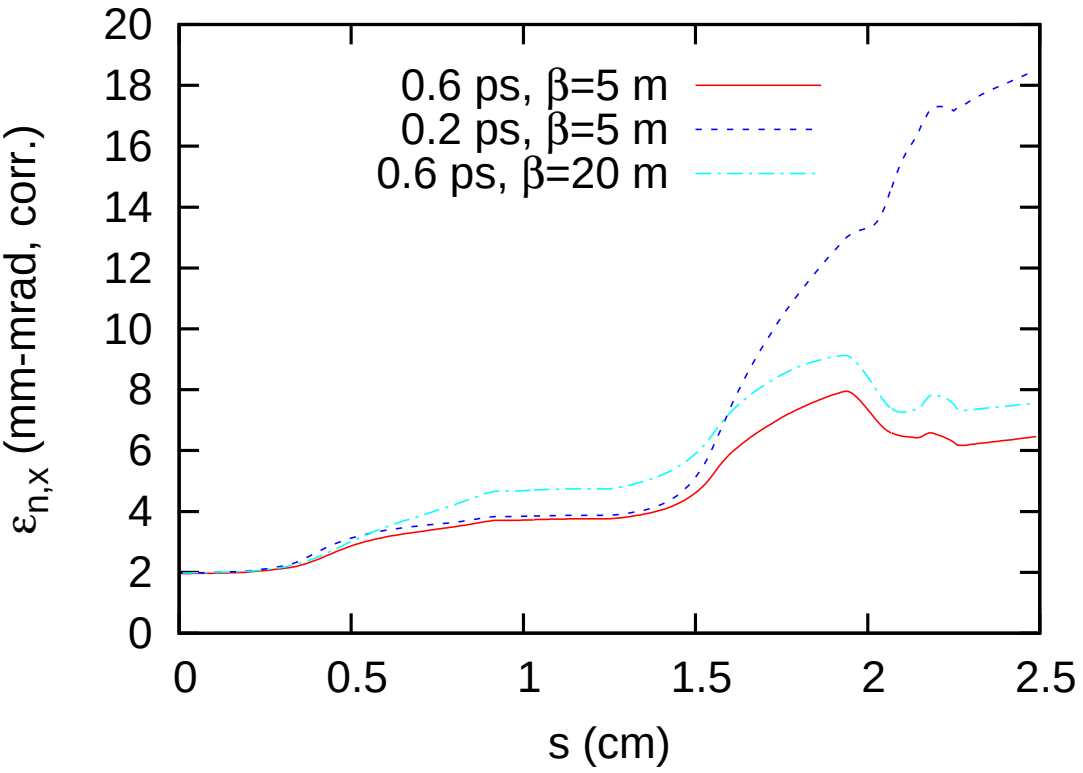

Figure 5.10: Dispersion-corrected transverse emittance as a function of path traveled in the SDL bunch compressor. The bunch charge is 0.3nC. The three differenent case show the effect of varying basic beam parameters on the emittance growth. The largest effect is pulse length which scale roughly as $\sigma_z^{-4/3}$. The effect of beamwidth is approximately $\tilde{x}^{1/2}$.

above for three combinations of parameters. When the amount of chirp is varied, causing the final compression to reduce by one-third, the emittance growth goes from 3.5 to 15.5 μm, a ratio of 4.4 compared to the predicted rough estimate scaling of $3^{4/3} = 4.3$. When the beam width is increased by emittance growth goes from 3.5 to 5.5 μm, a ratio of 1.6, compared to the rough estimate scaling of $\sqrt{2} = 1.4$. So for this set of parameters and variations, we see that the rough scaling is a good estimate and consistent with our simulations.

Up to this point, we have been talking about projected emittance. However, depending on the application the emittance may only be relevant over a time scale, smaller than the pulse length. For example, in a free electron laser, the relevant distance is the slippage length $l_{slip} = N_w\lambda$ where N_w is the number of wiggler periods and λ is the wavelength of the output light. For an IR FEL, $l_{slip} \sim 50$ μm, whereas for an X-ray FEL, it may be like $l_{slip} \sim 0.1$ μm. Since our simulation stores the complete phase space of the macroparticles, we can process it however we like. For instance, we may project it onto $x - x'$ phase in slices where the longitudinal coordinate lies within some range. If we do this for all the slices along the bunch we obtain the slice emittance. The result for 0.02 ps slices is shown in Fig. 5.11, for two levels of compression. In neither case, does the wieghted-average slice emittance differ significantly from the projected.

Another way to visualize, or understand what has happened to the electron beam is to look at a density plot in phase-space, rather than single measures like emittance. First let us examine the $x - x'$ phase space for the 0.2 ps compression case as shown in Fig. 5.12. The reason the emittance is increasing in this case is a deformation in transverse phase-space. A growth in projected emittance from purely longitudinal energy modulation would appear as a smearing out in the vertical (x') direction of the usual elliptical distribution.

We can also examine the longitudinal phase space, shown in Fig. 5.13. Even without CSR, the longitudinal phase space will show an arc shape. This is due to the non-linear dependence of path length, and therefore compression, on energy. The beam starts with a perfect linear energy dependence, and with no incoherent energy

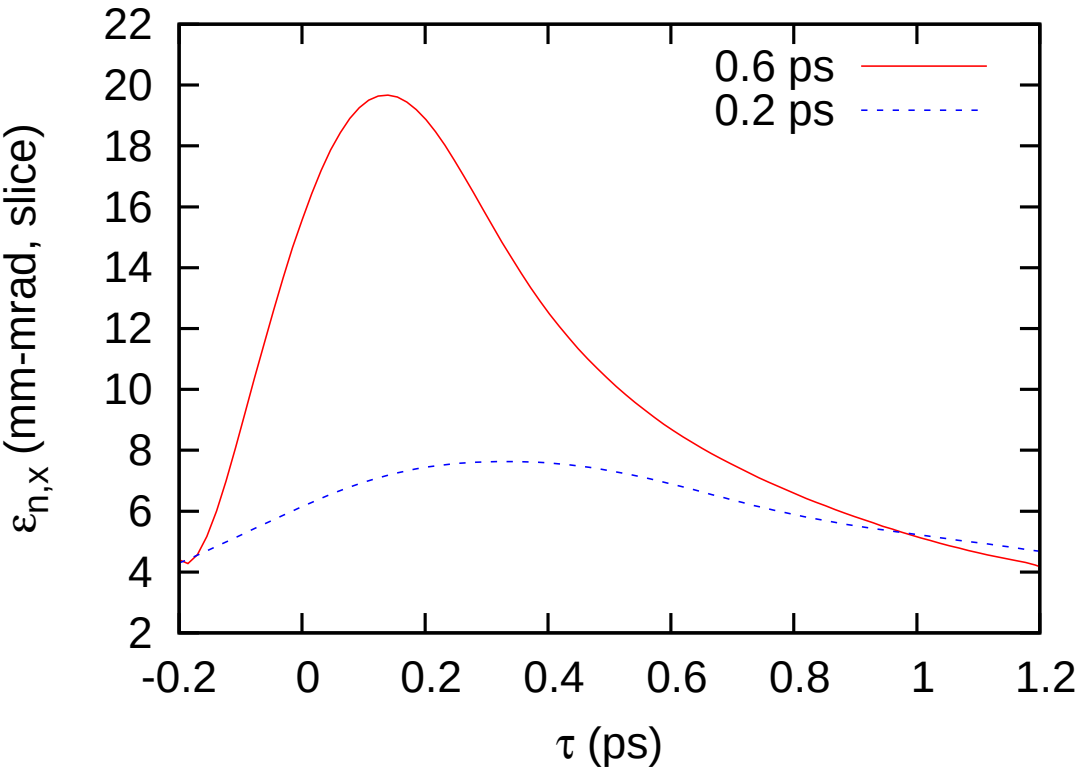

Figure 5.11: Emittance (x, rms, normalized) taken in 0.02 ps slices at exit of compressor for 0.2 ps rms final pulse length(red, solid) and 0.6 ps (blue, dashed). Each slice is corrected for the centroid of x and x' independently. For the 0.2 ps case, the projected emittance was 18.5 μm, and for the 0.6 ps case, the projected emittance was 5.5 μm. In both cases, there is not a significant difference between the peak slice emittance and the projected emittance, indicating that the emittance growth is random, not systematic.

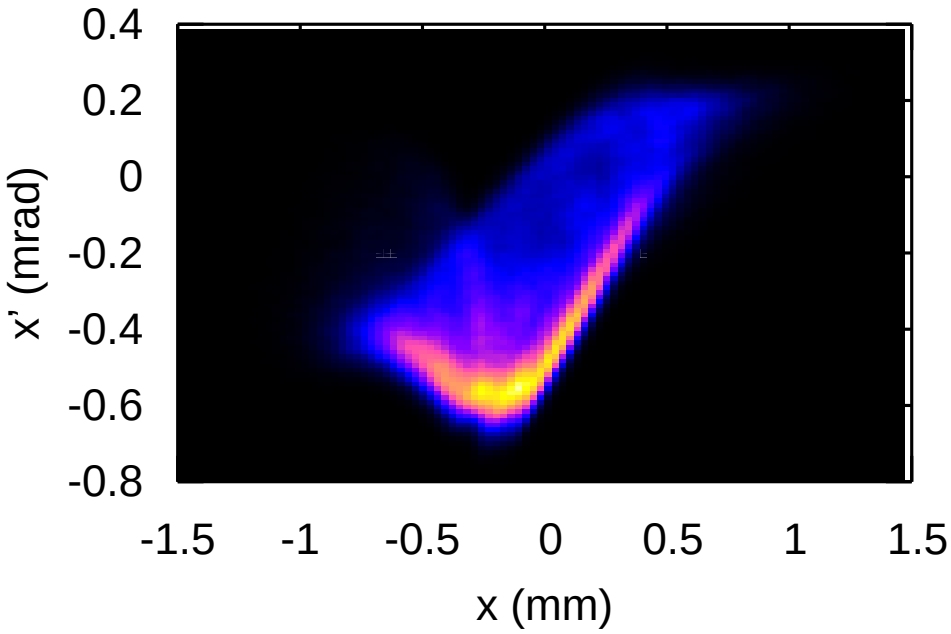

Figure 5.12: Transverse (x) phase-space at exit of SDL bunch compressor. The bunch charge is 0.3 nC, and the final rms pulse length is 0.2 ps. The offset in both coordinates is due to the net energy loss of the beam. The normalized rms emittance, which is corrected for the offsets in centroids, is 18.5 mm-mrad (initial was 2 mm-mrad).

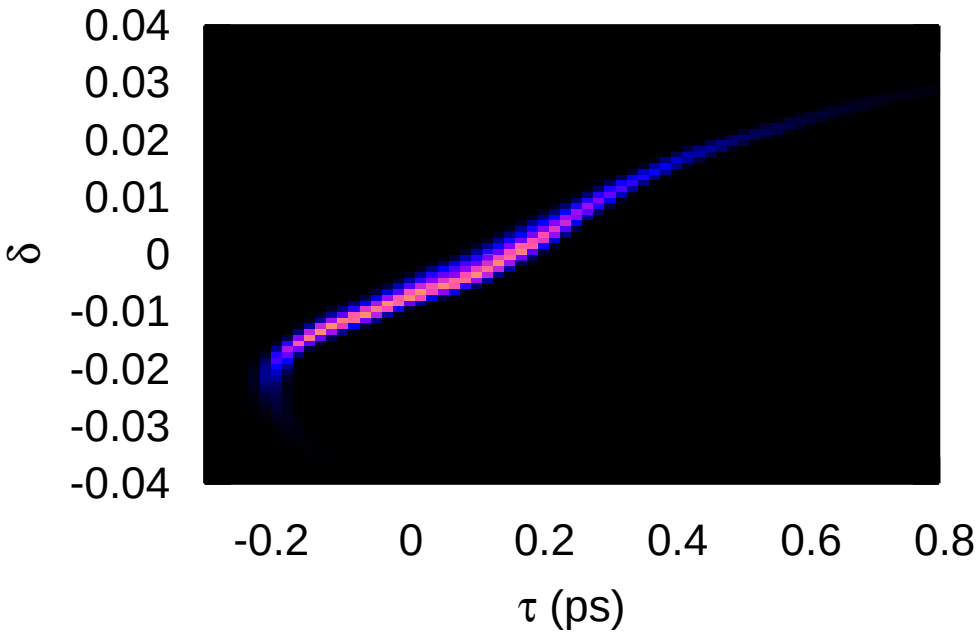

Figure 5.13: Longitudinal phase-space at exit of SDL bunch compressor. The bunch charge is 0.3 nC, and the final rms pulse length is 0.2 ps. The general curved shape reflects the non-linear dependence of path length on energy. The wavy deflection in the center is from CSR.

spread. In reality the initial longitudinal emittance (area in phase space, analogous to transverse emittance) would limit the compression, even with non-linearty. The wavy defelction in the center is a result of the CSR forces.

So, we have demonstrated a small sample of our simulation's capabilities to perform end-to-end modeling of bunch compressor chicanes in a self-consistent manner, complete with longitudinal and transverse space-charge effects, as well as perfectly conducting boundary walls. These sample simulations are not intended to be an exhaustive parameter study of this design, rather just to show what types of

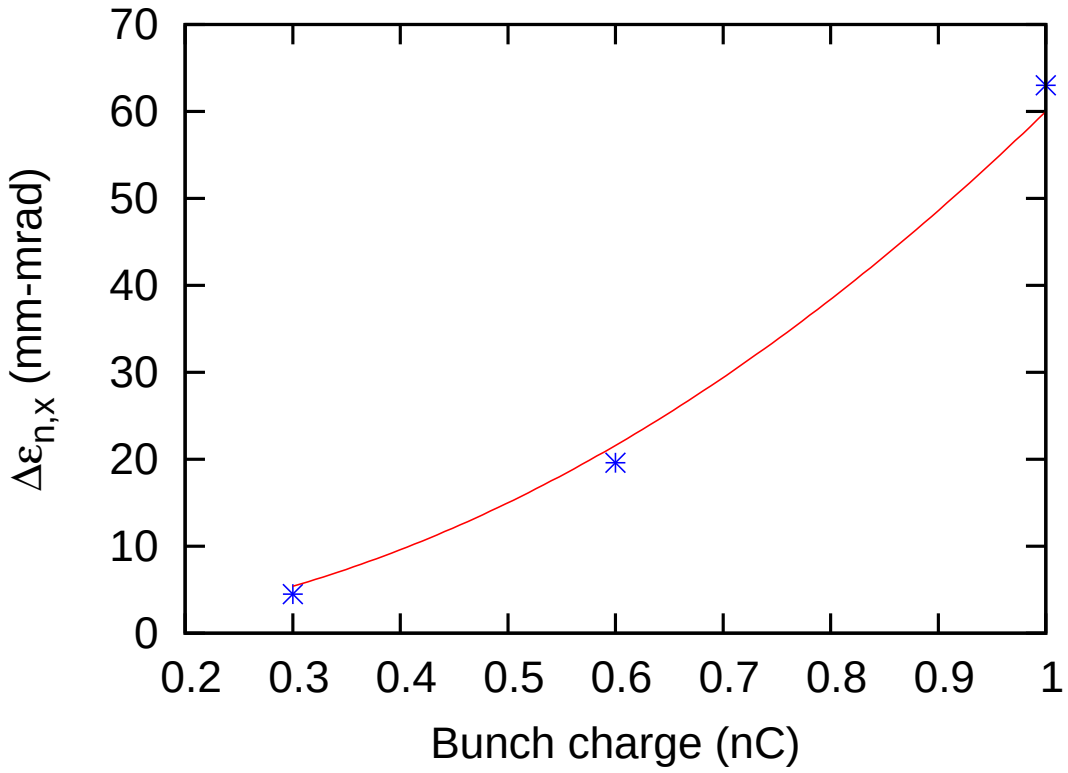

Figure 5.14: Transverse emittance growth for three different values of bunch charge. Also plotted is a perfect quadratic dependence for reference.

capabilities it has. So far the scaling has been consistent with our rough estimate. However, varying the remaining parameter, bunch charge, does not result in the expected behavior. In Fig. 5.14, we see the final emittance growth for three different values of bunch charge, 0.3, 0.6 and 1.0 nC. We see there is nearly a perfect quadratic dependence, whereas our rough scaling indicates the dependence should be linear.

By comparing the rms beam width as a function of distance in the chicane for two different bunch charges as shown in Fig. 5.15, we see that for the 1.0 nC

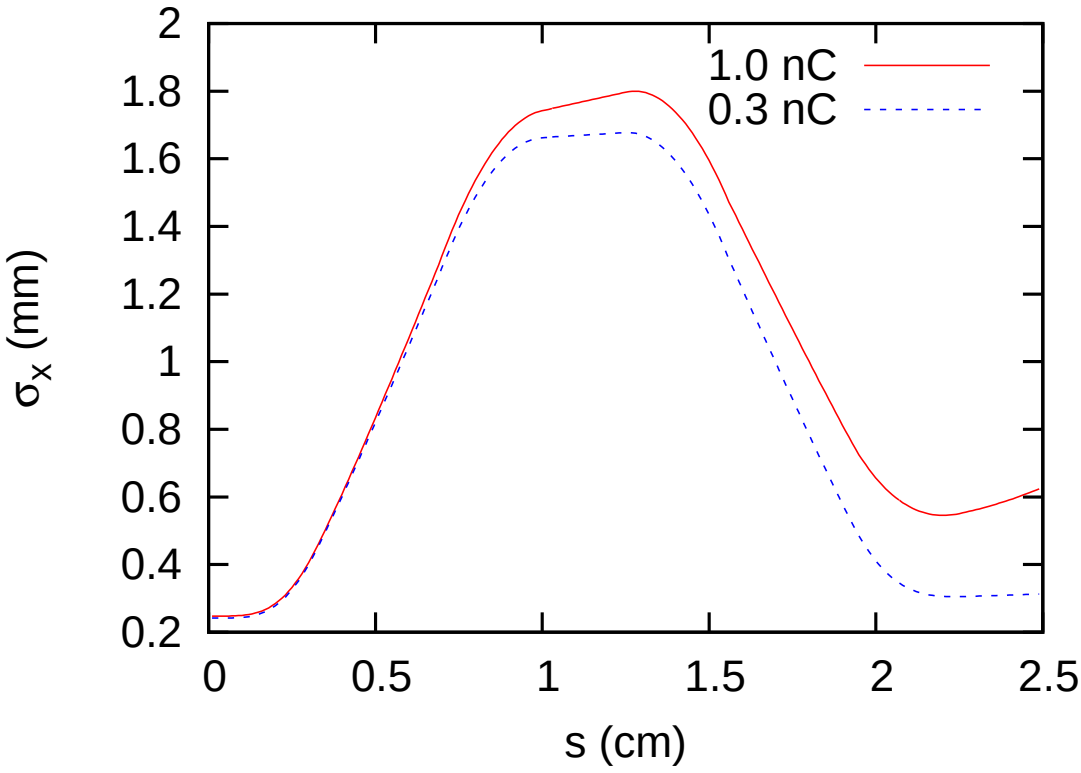

Figure 5.15: Transverse emittance growth for three different values of bunch charge. Also plotted is a perfect quadratic dependence for reference.

case, space charge has altered the beam envelope. Our rough estimate had assumed that the beam width at the exit was nearly the same as the input. However, this is clearly not the case and we see that it has increased by at least a factor of two. Since our rough estimate depends linearly with beam width, this at least explains some of the scaling with bunch charge. While not entirely explaining the behavior, we speculate that because of the strength of the space charge fields as well as the CSR fields that our simple scaling is not taking enough of the dynamical behavior into account. Furthermore, this type of non-linear scaling of effects illustrates the need for simulations in general to account for as much of the physics as possible.

5.4 Microbunching

The concept of microbunch with regards to CSR is that perturbations in either current or energy may grow and hence lead to instability [7]. Even if the bunch length is such that self-interaction is shielded, such as in the case of parallel plates or a waveguide, the modulation with a much shorter wavelength could act coherently and feel the full effects of CSR. Once again, the theoretical development for the microbunching instability has assumed a line charge distribution. Of course, this may be quite reasonable for a storage ring with transverse focusing, but would not generally be the case for a bunched beam in either a chicane or 180^o bending system typical in energy recovery linacs. The beam will travel in a vacuum pipe of some in these bends, so this is the perfect sort of thing that SCARS could simulate.

As already discussed, at sufficiently long bunch lengths in a toriodal waveguide,

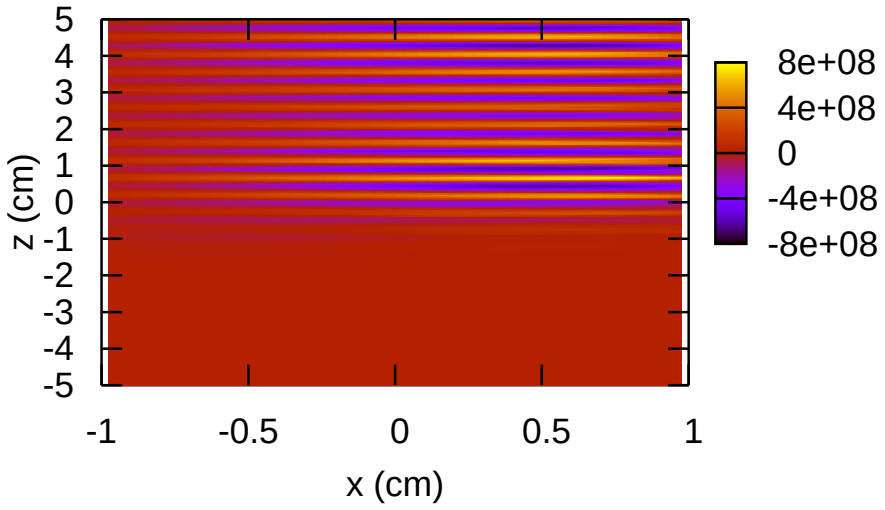

Figure 5.16: Longitudinal force after 375 cm (one-half revolution) at midplane ($y = 0$) as a function x, positive towards the outside wall and z, negative towards the bunch head. The bunch is surrounded by a square waveguide with dimension 2.5 cm. The other parameters are $R = 120$ cm, $E = 100$ MeV, Gaussian bunch $\sigma_z = 5.75$ mm with 20% modulation at wavelength 4.0 mm, initial $\sigma_x = 1.0$ mm.The color indicates the magnitude of the longitudinal force, in units of F_z/e^2 (cm^{-2}). There is no force forward of the bunch because the group velocity for this (and all) resonant mode is less than than the bunch velocity. At this bunch length, the beam would otherwise be completely shielded from CSR self-interaction, however the modulation has stimulated the lowest order synchronous mode.

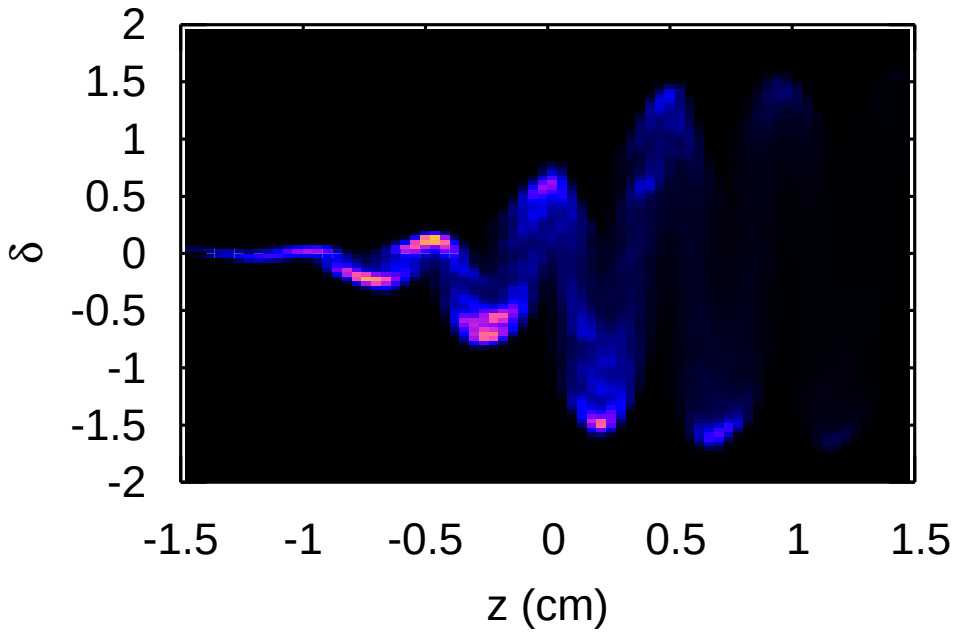

Figure 5.17: Longitudinal phase space density after 375 cm (one-half revolution). The bunch is surrounded by a square waveguide with dimension 2.5 cm. The other parameters are $R = 120$ cm, $E = 100$ MeV, Gaussian bunch $\sigma_z = 5.75$ mm with 20% modulation at wavelength 4.0 mm, initial $\sigma_x = 1.0$ mm. Although the bunch clearly shows modulation a the wavelength of the lowest synchronous mode, there is a substantial incoherent energy spread resulting from the beam width.

even the lowest frequency resonant mode will not be stimulated and there will be no interaction. However, if there is some modulation in current at a wavelength below the resonant maximum, some modes can be stimulated. In particular it may be possible to interact with a single resonant mode [64]. This is exactly the case shown in Fig. 5.16. Here, we see F_z/e^2 displayed as a function of x and z, after traveling halfway around in a square rectangular toroidal waveguide with dimension 2.5 cm. The bending radius 120 cm as Chapter 3, so the wavelength of the resonant mode is the same at 4.75 mm. The Gaussian bunch length is 5.75 mm, so no resonant interaction would be stimulated under normal circumstances. We verified this by stimulating the bunch with no additional modulation, and indeed there was no additional fields beyond the usual space-charge. In Fig. 5.16, however, the Gaussian beam was initially modulated by 20% with a sinusoidal perturbation with wavelength of 4.0 mm, close to the lowest resonant mode wavelength. As a result, one can clearly see the stimulation of the lowest resonant mode behind and within the bunch.

The longitudinal force of the resonant mode stimulated by the intial current density will in turn modulate the bunch energy. Once can estimate, in simple terms, the effect on density. In the absence of any transverse focusing, the change in path length Δl from an energy deviation δ will be

$$\Delta l = \delta s, \tag{5.28}$$

where s is the total distance traveled. If the energy deviation is coming from a

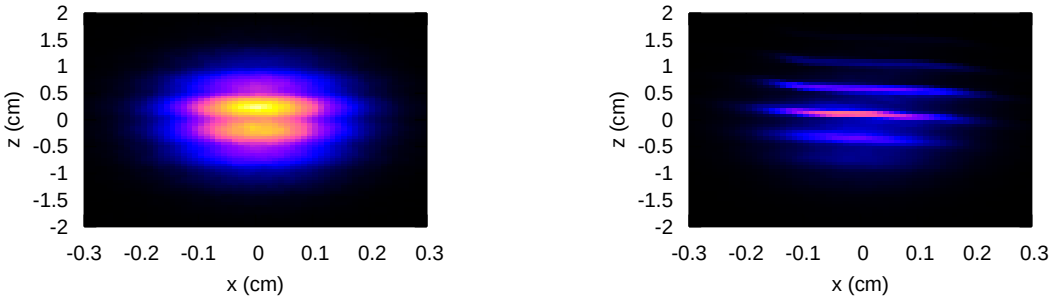

Figure 5.18: Charge density as a function of x (horizontal, outer wall to right) and z (vertical, head is towards bottom) comparing input (on left) and output after 180^o bend. The intial modulation was 20% with a 4.0 mm wavelength on a Gaussian bunch with $\sigma_z = 0.575$ mm, which would otherwise be completely shielded from CSR interaction. The waveguide is square with transverse dimension 2.5 cm and bending radius R= 120 cm. Although the amount of bunching is small, there is a noticeable effect particularly towards the tail of the bunch. Microbunching is also limited somewhat by the finite beamwidth which in this case is 1 mm, approximately 25% of the resonant wavelength.

constant longitudinal force then

$$\delta = \frac{F_z/e^2}{\gamma r_0} s. \tag{5.29}$$

Combining these we can estimate the path length change, or potential microbunching over a given total path, assuming the longitudinal field remains constant

$$\Delta l = \frac{F_z/e^2}{\gamma r_0} \frac{s^2}{2}. \tag{5.30}$$

In the example for the simulation, the steady-state field for the lowest resonant mode is $F_z/e^2 \approx 8 \times 10^8$ cm-2. For one full revolution of $s = 750$ cm, the potential path length difference is 0.16 cm or approximately one-quarter of the mode wavelength. Because of the natural momentum compaction, all electrons gaining energy will fall back, while those losing energy will move forward. The electrons should accumulate and enhance the density modulation at the zero field points. Looking at the projection of the beam onto $x-z$ space, comparing the input to output after one complete revolution as shown in Fig. 5.18, we clearly see growth in the modulation. This can be illustrated, perhaps even more clearly by comparing the current between input and out as shown in Fig.5.19.

One might expect all resonant modes with shorter wavelegths also to be unstable in a similar fashion. There are a few effects that might mitigate this, however. For clarity, we did not apply any incoherent energy spread, but that would obviously smear out the longitudinal phase space modulation. Additionally, the natural betratron motion where electrons not directly on the longitudinal axis will rotate in $x - z$ space, may also interfere with the energy modulation. If the initial x coordinate is large compared to the wavelenth, then over one revolution, the electron

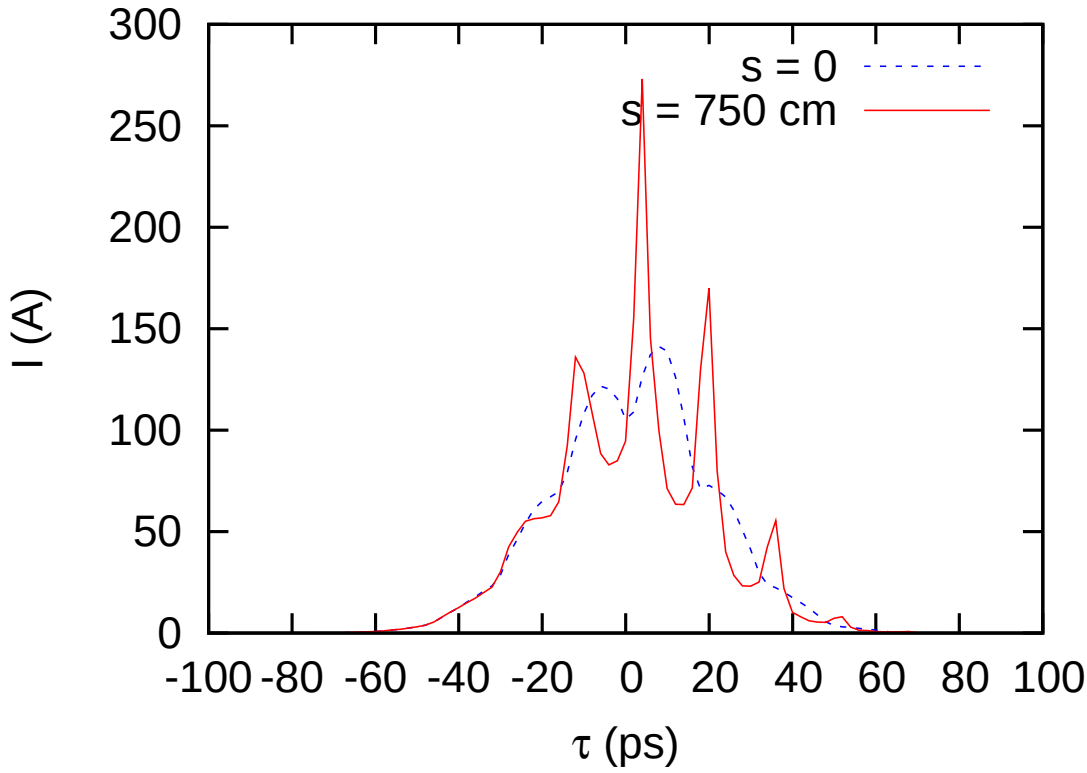

Figure 5.19: Current comparing input (blue, dahsed) and output (red, solid) after one complete revolution in bend. The intial modulation was 20% with a 4.0 mm wavelength on a Gaussian bunch with $\sigma_z = 0.575$ mm, which would otherwise be completely shielded from CSR interaction. The waveguide is square with transverse dimension 2.5 cm and bending radius R= 120 cm.

will see both accelerating and decelerating fields equally. Here, we can already see some evidence of the betatron motion relfected in the projection onto longitudinal phase space, as the sinusoidal modulation is broadened incoherently. So at very short wavelengths, one might expect no microbunching gain at all, the coherence being completely diestroyed by the beam width.

Chapter 6

Summary and Outlook

The goal was to develop a new simulation in order to calculate CSR effects, taking into account as much of the real physics as possible. However, in endeavoring to do so, one must continually test the results against reality and theory, and even other simulations as much as possible. Therefore, much effort has been expended, not only to create the model, but to write and test the code wherever possible. This aspect has been mostly successful, particulary in the cases where the theory is well-established for a rigid beam. Based on the results in Chapter 3, we feel that the paraxial wave equation contains all of the relevant physics, including space and computes them comrreclty as seen by direct comparisons to theory.

When we introduced the dynamic source in a self-consistent manner, we also moved beyond most of the theories in which we can compare the results to. Therefore, we can only compare some simple dynamics and test the parts that are well understood. In this manner, we feel mostly successful, in that the results seem to obey scaling laws consistent with our understanding. However in our test case, there remains an quadratic scaling with bunch charge, which we speculate is the combined action of emittance dilution due to energy spread and space charge repulsion. We feel this case in particular illustrates the need for a simulation that contains as much of the three-dimensional dynamics as it is possible to emulate. We have only run

a very limited set of examples, so a complete understandiong of the dependence of this emittance growth on initial parameters must remain a matter for future work.

Finally, we have introduced a new area of capability for this type of simulation that we feel can be accomplished nowhere else, namely the study of microbunching in toroidal waveguides. Through a relatively simple example, it appears that the interaction of the bunch with single resonant modes of the waveguide may lead to enhanced bunching or instability. Though our study of this phenomenon has just begun, it appears that the elements are in place and we hope to continue.

Bibliography

[1] H. P. Freund and T. M. Antonsen, Jr, *Physics of Free Electron Lasers* (Chapman and Hall, London, 1992).

[2] P. G. O'Shea and H. P. Freund, Science **292** (2001).

[3] M. Tigner, Nuovo Cimento **37** (1965).

[4] *Jefferson lab fel website*, `http://www.jlab,org/fel`.

[5] *Cornell energy recovery linac website*, `http://erl.chess.cornell.edu`.

[6] R. Hajima et. al., Nucl. Inst. Methods, A **445** (2000).

[7] G. Stupakov and S. Heifets, Phys. Rev. ST Accel. Beams **5**, 054402 (2002).

[8] G. A. Schott, *Electromagnetic Radiation* (Cambr. Univ. Press, Cambridge, UK, 1912).

[9] J. P. Blewett, Phys. Rev **69** (1946).

[10] J. Schwinger, Phys. Rev. **75**, 1912 (1949).

[11] L. J. Schiff, Rev. Sci. Inst. **17**, 6 (1946).

[12] J. S. Nodvick and D. S. Saxon, Phys. Rev. **96**, 180 (1954).

[13] P. Goldreich and D. A. Keeley, Atstrophysical Journal **170** (1971).

[14] A. Faltens and L. J. Laslett, Part. Accel. **4** (1975).

[15] R. Talman, Phys. Rev. Letters **56**, 1429 (1986).

[16] R. L. Warnock and P. Morton, Part. Accel. **25**, 113 (1990).

[17] K.-Y. Ng, Part. Accel. **25**, 153 (1990).

[18] Y. S. Derbenev, J. Rossbach, E. L. Saldin, and V. D. Shiltsev, TESLA-FEL **95-05** (1995).

[19] S. Heifets, G. V. Stupakov, and S. Krinsky, Phys. Rev. ST Accel. Beams **5**, 064401 (2002).

[20] E. L. Saldin, E. A. Schneidmiller, and M. V. Yurkov, Nucl. Instr. and Meth. in Phys. Res. **A 398**, 373 (1997).

[21] G. Bassi, T. Agoh, L. Giannessi, R. Hajima, A. Kabel, T. Limburg, and M. Quattromini, Nucl. Inst. Meth. A. **557**, 189 (2006).

[22] G. V. Stupakov and I. A. Kotelnikov, Phys. Rev. ST Accel. Beams **6**, 034401 (2003).

[23] T. Agoh and K. Yokoya, Phys. Rev. ST Accel. Beams **7**, 054403 (2004).

[24] S. Krinsky and J. M. Wang, Part. Accel. **17** (1985).

[25] M. Venturini et. al., Phys. Rev. ST Accel. Beams **8** (2005).

[26] F. R. Elder, A. M. Gurewitsch, R. V. Langmuir, and H. C. Pollock, Phys. Rev. **7**, 829 (1947).

[27] A. A. Liénard, L'Eclairage Electr. **16**, 5 (1898).

[28] E. Wiechert, Ann. d. Phys. **4**, 667 (1901).

[29] J. D. Jackson, *Classical Electrodynamics* (John Wiley & Sons, New York, 1975), 2nd ed.

[30] J. B. Murphy, S. Krinsky, and R. L. Gluckstern, Part. Accel. **57**, 9 (1997).

[31] S. Ramo, J. R. Whinnery, and T. V. Duzer, *Fields and Waves in Communication Electronics* (John Wiley & Sons, New York, 1994), 3rd ed.

[32] R. L. Warnock, Tech. Rep. SLAC-PUB-5375, SLAC (1990).

[33] S. Benson et al., in *Proceedings of the 2004 FEL Conference* (2004).

[34] M. Cornacchia (1999), invited talk at Free Electron Laser Challenges II Technical Conference 3615 of SPIE photonic West 99 Conference 23-27 Jan 1999, San Jose, CA.

[35] I. Bazarov et al., in *Proceedings of the EPAC 2002 Conference* (2002).

[36] A. Piwinski, Tech. Rep. LEP-TH/85-43, CERN (1985).

[37] Y. S. Derbenev and V. D. Shiltsev, Tech. Rep. SLAC-PUB-7181, SLAC (1996).

[38] T. Agoh, in *Proceedings of the APAC 2004 Conference* (2004).

[39] T. Agoh, Ph.D. thesis, University of Tokyo (2004).

[40] M. Leontovich and V. Fock, J. Phys. USSR **10**, 13 (1946).

[41] W. K. H. Panofsky and W. A. Wentzel, Rev. Sci. Instr. **27**, 967 (1956).

[42] R. Li, in *Proceedings of the EPAC 2002 Conference* (2002).

[43] E. P. Lee, Part. Accel. **25**, 241 (1990).

[44] G. Geloni, E. Saldin, and E. Schneidmiller, Tech. Rep. DESY 03-165, DESY (2003).

[45] L. D. Landau and E. M. Lifshitz, *The Classical Theory of Fields* (Butterworth Heineman, Oxford, 1975), 4th ed.

[46] E. O. Brigham, *The Fast Fourier Transform and its Applications* (Prentice Hall, Englewood Cliffs, NJ, 1988).

[47] J. H. Press, S. A. Teukolsky, W. T. Vetterling, and B. P. Flannery, *Numerical Recipes in C++* (Cambridge University Press, Cambridge, UK, 2002), 2nd ed.

[48] E. L. Saldin, E. A. Schneidmiller, and M. V. Yurkov, Nucl. Instr. and Meth. in Phys. Res. **A 398**, 373 (1997).

[49] C. Birdsall and D. Fuss, J. Comput. Phys. **135** (1997).

[50] B. Terzić, I. Pogorelov, and C. Bohn, Phys. Rev ST Accel.Beams. **10** (2007).

[51] M. Reiser, *Theory and Design of Charged Particle Beams* (Wiley Interscience, New York, 1994).

[52] I. M. Kapchinksy and V. V. Vladimirsky, in *Proceedings of the International Conference on High Energy Accelerators, CERN, Geneva* (1959), p. 274.

[53] B. E. Carlsten and T. O. Raubenheimer, Phys. Rev. E **51**, 1453 (1995).

[54] *CSR workshop 2002*, `http://www.desy.de/csr`.

[55] *LCLS website*, `http://www_ssrl.stanford.edu/lcls`.

[56] *TESLA-XFEL website*, `http://www.xfel.desy.de`.

[57] D. Gillingham and T. Antonsen, Jr., Phys. Rev. ST Accel. Beams **10**, 054402 (2007).

[58] *TraFiC4*, `http://www.slac.stanford.edu/ kabel/TraFiC4`.

[59] *Tredi*, `http://www.tredi.enea.it`.

[60] R. Li, in *Proceedings of the EPAC 1998 Conference, Stockholm, Sweden.* (1998).

[61] M. Borland, Tech. Rep. LS-287, Advanced Photon Source (2000).

[62] G. Stupakov and P. Emma, Tech. Rep. LCLS-TN-01-12, SLAC (2001).

[63] M. Dohlus, Tech. Rep. TESLA-FEL-2003-05, DESY (2003).

[64] S. Heifets and G. Stupakov, Phys. Rev. ST Accel. Beams **5**, 064401 (2002).